The Structure and Evolution of Disk Galaxies

by

Zheng Zheng

A dissertation submitted to The Johns Hopkins University in conformity with the requirements for the degree of Doctor of Philosophy.

Baltimore, Maryland

July, 2014

Abstract

The general theoretical framework for the formation and evolution of galaxies has been successful in explaining the basic properties of disk galaxies. However, many questions remain as to the detailed mechanisms by which the specific observed properties of galaxy disks are produced over cosmic time. In this thesis we focus on two specific aspects of disk galaxies in the local universe. First, we develop a model based on the idea that disks self-regulate to achieve a state of marginal dynamical stability. Our model allows us to successfully predict the gas surface mass density and star formation intensity of a galaxy given its rotation curve and stellar surface mass density. Second, we use very deep imaging from the Pan-STARRS1 survey to study the outer disks of galaxies. Our results imply that the simple inside-out model for the evolution of disk galaxies needs to be modified to include the radial migration of stars and the suppression of star formation in the outer disk.

Acknowledgments

At the endpoint of my seven years Ph.D. student life, I can not help to write down my appreciations to those who made my life wonderful and my thesis possible.

First of all, I want to express my deepest gratitude to my three advisors, Gerhardt Meurer, David Thilker and Timothy Heckman. Prof. Meurer, who led me to the world of galaxies, the subject of my thesis, is humorous and inspiring and he gave me great help not only in my academic career but also in my personal life. Dr. Thilker, who inspired my scope of the second part of my thesis, is encouraging, helpful, and never hesitate to provide me countless support in my research. Prof. Heckman, who oversaw my whole Ph.D. project, is one of the most insightful professors I have ever met, and he always guide me to the cores of the key questions in an intuitive way. I feel extremely fortunate to have the three extraordinary advisors and my gratitude to them is far beyond being describable by any languages.

I want to extend my appreciation to Ronald Allen, my summer research advisor at STScI for being supportive to my research and career. Martin Zwaan trained me in reducing radio data during my visit to ESO. My thesis committee members

ACKNOWLEDGMENTS

Rosemary Wyse and Jennifer Lotz helped improve the quality of my thesis. I also benefit a lot from discussions with my collaborators Oiwei Ivy Wong and Mark Huber. I am grateful to all my coauthors and the Pan-STARRS1 team even they are not yet mentioned explicitly here.

I am indebted to Guilin Liu, my college and one of my best friends, for willing to help and give his best suggestions at all times. Special thanks to my fellow students and friends in the P&A department including but not limited to Jian Su, Jianjun Jia, Kuang-han Huang, Wei Liu, Rongguang Xu, Guofan Hu, Jian Kang, Bingxiao Xu, Jiajia Wen, Mingen Li, Shan Wu, Danru Qu, Ting Su, Yongjie Xin, Zhilei Xu, Lin Yang, Ting-wen Lan, Guangtun Zhu and Xin Wang. They made my life in Baltimore colorful and enjoyable.

I would specially thank my parents for being always supportive. I am also grateful to my wife for giving birth to my lovely son and being understanding in the past 7 years.

Dedication

To my parents,

Zheng De Min and **Zhang Lei**,

my wife, **Qiao Wen**,

and my son, **Xerxes.**

Contents

CONTENTS

List of Tables

List of Figures

Chapter 1

Introduction

1.1 Motivation

It is widely accepted that galaxies were formed out of the collapsing of primordial gas inside dark matter halos (Fall & Efstathiou , 1980). Some of the primordial material acquired enough angular momentum through tidal torques to ultimately produce a rotating disk galaxy. The inner part of the protogalaxy has very low angular momentum and high density and therefore it collapses in a shorter timescale and forms the central bulge (and possibly the surrounding stellar halo). The outer part of the gas cloud, probably shock heated, has lower density and thus cools more slowly and contracts to its corresponding angular momentum radius. Accreted material continues to fall onto the disk during the whole life of the disk galaxy. The gas accreted in later stages usually has higher specific angular momentum so that it falls

onto outer region of the disk. The newly accreted gas fuels star formation in the outer disk and the stellar disk would be growing from inside to out (Mo et al. , 1998; Kepner , 1999). The dark matter halos and galaxies will also experience mergers and build up more massive halos and galaxies. This so called hierarchical clustering and inside-out formation scenario is very simple and intuitive and is supported by various studies (e.g. Nelson et al. , 2012; Pěrez et al. , 2013). However, the details of the disk formation and evolution, especially the internal secular evolution theory are still not very clear and some questions with significant cosmological relevance are still not well addressed.

1.2 Star formation and disk stability

One of the big questions is: what is regulating the star formation in the disk. This is important because star formation converts gas into the stars and it is the stars that light up the galaxy. The stars are also a major source of feedback in terms of radiation, mechanical energy input, and chemical enrichment. Unfortunately, the question is too difficult to be solved in a simple way because the physical processes related to star formation are complicated and involve not only a wide range of physical scales from the atomic to galactic but also different components/phases of the ISM. Generally speaking, studies of galactic star formation can be divided into two categories: one is the 'star formation law' (SFL), which explores the relationship between star formation

rate and gas properties. The most successful SFLs are perhaps the empirical relations between the surface density of star formation and gas such as the 'Schmidt-Kennicutt Law' (Kennicutt , 1989, and more details and SFLs in Section 2.3.3). The other is a star formation threshold (cf. Section 2.3.1), which focuses on the threshold in gas densities needed to support wide spread star formation.

The most straightforward way to study the star formation threshold is to investigate the gravity-related physics, because star formation is basically the process of gas collapsing under the influence of gravity. Gravity also plays an important role in shaping the galaxy: it controls the orbits of gas particles and stars and more importantly, it controls the collapsing of gas, which makes the stars. The redistribution of gas and stars in turn reshape the gravitational potential and makes the process more complicated. Theoretical studies on the star formation threshold focus on the balance between the gravitational force of attraction and the expansion force induced by the motions of the gas particles. The gravitational stability parameter Q for a single-component thin disk was first derived by Toomre (1964). Later on, different versions of the two-fluid stability parameter Q_{2f} (e.g. Rafikov , 2001; Wang & Silk , 1994; Romeo & Wiegert , 2011, more details in Section 2.3.1) were developed to characterize the stability of the disk composed of both stars and gas. The Toomre's Q parameter and subsequent versions of Q_{2f} have been used as star formation indicators. The basic idea is that a disk with a Q_{2f} value less than unity (or some empirical constant value) at some location is unstable and small fluctuations will result in large

instabilities and thus lead to wide spread star formation. In contrast, a disk area with a Q_{2f} value greater than unity (or some empirical constant value) has enough supportive force from gas motions to resist the gravity and is too stable to collapse and form stars. Therefore, we expect spontaneous star formation in low Q_{2f} regions and little or no star formation in high Q_{2f} regions. However, observations show that the two-fluid stability parameter is almost a constant within the whole galactic disk (Kennicutt , 1989; Meurer et al. , 2013; Boissier et al. , 2003; Martin & Kennicutt , 2001; Wang & Silk , 1994; Leroy et al. , 2008). Figure 1.1 shows the Toomre's Q profiles of a sample of nearby galaxies. These galaxies almost all have a constant Q up to a couple of optical radii.

One plausible explanation for this constant Q phenomena is that the galactic disk is self-regulated by star formation: the heating and outflows induced by star formation counteract with gravity and the galaxy is usually in an equilibrium state, i.e. normal galaxies are generally marginally gravitational stable. This kind of equilibrium gives us a chance to estimate the relatively difficult to measure quantities, e.g. gas and star formation, using some easy to observe quantities, such as stellar mass. This fact has been realized by Quirk (1972) and he successfully 'predicted' the gas distribution of several disk galaxies. It has been four decades since the work of Quirk (1972) and there are a lot of progress on the disk stability theory. Inspired by the work of Quirk (1972), we studied the most recent disk stability theory and several empirical relations and developed a simple 'constant-Q' (CQ) model to estimate the radial distribution

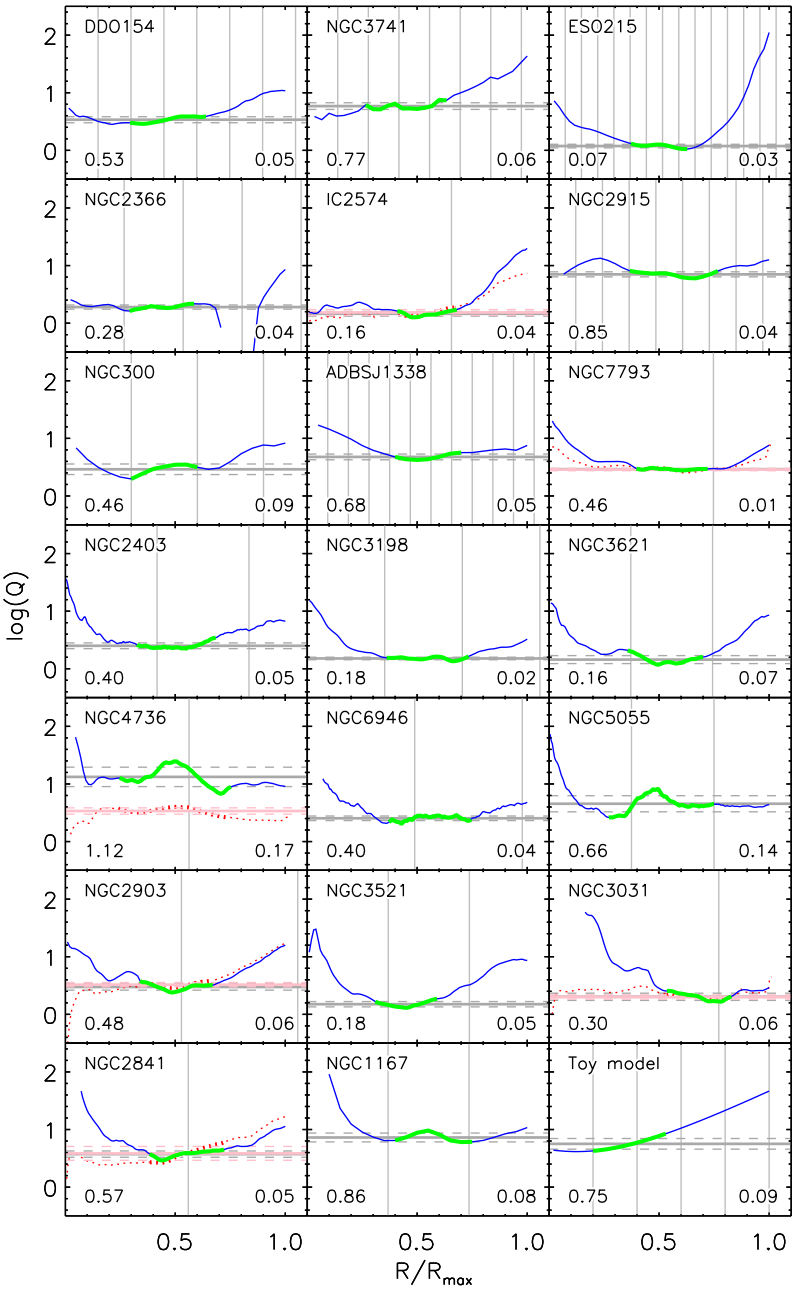

Figure 1.1: Stability parameter radial profiles of 20 nearby galaxies and a toy model galaxy. Blue solid lines show the Toomre's Q parameter and red dotted lines show the two-fluid stability parameter Q_{2f} by Romeo & Wiegert (2011). The intermediate disk containing 50% of the HI mass is highlighted in thick green lines. The horizontal gray and red lines show the constant fit to the highlighted region. The vertical gray lines show intervals of r_{25} (the radius where the B-band surface brightness is 25 mag/arcsec^2). The figure is from (Meurer et al., 2013).

of gas and star formation rate (SFR) using the stellar mass and rotation curve as an input or vice versa. This work is presented in Chapter 2. The model is successful in explaining the distribution of gas and SFR in a sample of THINGS galaxies and also successful in explaining the $1/r$ distribution of HI in most galaxies (Meurer et al., 2013). It gives an alternative explanation to the gas distribution in the galaxy, i.e. the gas and stars redistribute in secular evolution so that the disk always maintain a constant Q.

1.3 The outer disk and stellar halo

The reason to study the outer disk is that it is the place where the galaxy is currently growing more actively (in the sense of highest specific star formation rate) according to the inside-out galaxy formation scenario. Studying in the outer disk may give us some insight into disk formation processes (internal motions, in-situ star formation, star formation thresholds) and their relative importance.

To the first order, the surface-brightness (SB) profile of stellar disks of galaxies can be well described by an exponential function (Freeman , 1970). van der Kruit (1979); van der Kruit & Searle (1981) studied several edge-on disk galaxies and found that the exponential disk does not continue forever, but is truncated in the outer disk. Later studies (e.g. Pohlen et al., 2002; Erwin et al., 2005, 2008; Pohlen & Trujillo , 2006, hearafter PT06) using deeper imaging data reveal that most of the stellar disks

are not single exponential or truncated exponential but broken exponentials. PT06 classified different types of disk SB profiles into three categories: Type I (the classical single exponential), Type II (down-bending) and Type III (up-bending). The type I galaxies are only about 10% of the population and most ($\sim$ 60%) galaxies are Type II.

A single exponential profile can be easily explained by the collapsing model of a uniformly rotating protogalactic cloud (Fall & Efstathiou , 1980; Ferguson & Clarke , 2001). Type II profiles could be due to star formation being suppressed in the outer regions because of very low gas density (Kennicutt , 1989; Schaye , 2004; Elmegreen & Hunter , 2006). However, the collapsing model plus the star formation threshold can not produce a single SB exponential profile out to large radii (Schaye , 2004). This leads to other explanations such as radial stellar migration (Debattista et al. , 2006; Roškar et al. , 2008). The interplay between a star formation threshold and radial stellar migration produces stellar radial profiles in good agreement with observed Type II (Roškar et al. , 2008). Radial stellar migration also plays an important role in forming the Type III profiles if combined with environmental interactions (Younger et al. , 2007; Minchev et al. , 2012). Later studies of radial color profiles (e.g. Bakos et al. , 2008) indirectly confirmed the signature of the stellar radial migration (Roškar et al. , 2008; Sánchez-Blázquez et al. , 2009) by showing a 'U' shape color profile for the Type II galaxy (Fig. 1.2).

Despite the progress, our understanding of the formation and evolution of the outer

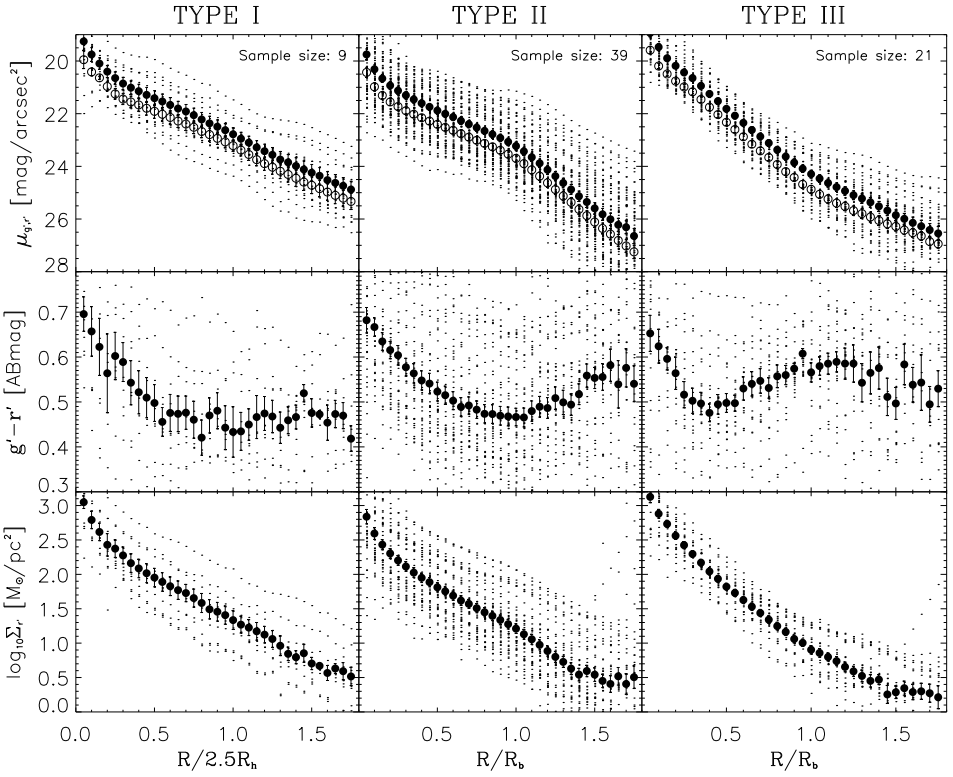

Figure 1.2: Stacked SB (top row), $g-r$ color (middle row) and stellar surface mass density (bottom row) profiles of PT06 galaxies. The small dots show profiles of individual galaxies and the big dots with error bars show the mean values with scaled scatter. The Figure is from Bakos et al. (2008).

disk is still incomplete. With recent improvements in availability of deep multi-band imaging we can make significant progress on this topic. Our investigation improves on the past studies in several ways:

Firstly, previous studies are mostly focused on single band surface brightness (e.g. Freeman , 1970; Pohlen & Trujillo , 2006), however, theoretical models (e.g. Roškar et al. , 2008) are mostly emphasize on physical parameters such as the stellar mass distribution. Single band photometry is not a good tracer to the underlying physical parameters because different stellar populations have very different ages and mass-to-light ratios. Bakos et al. (2008) studied the $g - r$ color profiles of PT06 galaxies and applied the mass-to-light ratio prescription of Bell et al. (2003) to get the stellar surface mass density profiles. The two-band color is helpful in removing the degeneracy between stellar mass and age but is still not very accurate. A more elaborate and robust way to to study the distribution of stellar mass is to use stellar population synthesis models describing predicted photometric quantities for a diverse collection of realistic star formation histories and a robust multi-band spectral energy distribution (SED) fitting method.

Secondly, the SB of the outermost regions might be affected by the surrounding stellar halos. The most systematic previous study ,e.g. PT06, has a sky background uncertainty of about 27 mag/arcsec^2. This limiting SB might already be affected by the stellar halo region (Zibetti et al. , 2004) but it is still too shallow to be dominated by the stellar halo. Bakos & Trujillo (2012) (cf. Fig. 1.2) studied 7 of the PT06

galaxies using SDSS stripe82 deep imaging data and they claim that there are no true Type I profiles and that the up-bending part of the Type III profile is really produced by the stellar halo. Therefore, a more systematic deep survey is needed to disentangle the light from the outer disk v.s. the stellar halo.

Last but not least, previous studies have focuses on very nearby galaxies and most sample sizes are relatively small. The largest sample up to now is the sample of 90 face-on to intermediate inclined nearby late-type (Sb - Sm) spiral galaxies selected by PT06. The PT06 sample is also distance (within $\sim$46 Mpc) and magnitude limited (B-band $M_{abs} < -18.4$). A larger sample with less constraint on distance and brightness, which is representative to the star-forming galaxy main sequence (Schiminovich et al. , 2007) is needed for us to determine the structure of a generic galaxy and measure the dependence of this structure on other galaxy properties.

To solve the problems stated above, we need a multi-band wide-field photometric deep survey. Fortunately, the Pan-STARRS1 (PS1) Medium Deep Survey (MDS) meets these requirements exactly. PS1 has five filters, g, r, i, z, y and the MDS fields have about 70 deg^2 in total and the depth of the MDS stack images are comparable if not deeper than the SDSS stripe82 images. We selected 700 galaxies in 8 of the 10 PS1 MDS fields (overlapping with SDSS, for spectroscopic redshift measurement) and derived 5-band SB profiles of these galaxies down to $28 - 30$ ABmag/arcsec^2. We then derive radial profiles of physical parameters, such as stellar surface mass density, specific star formation and mean stellar age using the SED fitting software

package, Multi-wavelength Analysis of Galaxy Physical Properties (MAGPHYS da Cunha et al. , 2008; Bruzual & Charlot , 2003; Charlot & Fall , 2000). The general properties of the stellar mass radial profile and mass-to-light ratio profile are presented in Chapter 3.

The most important result is that the generic M/L profile represented by the stacked M/L profiles has a 'U' shape with the minimum located around r_{90} (the radius containing 90% of the r-band Petrosian flux). The average stellar age of the outer disk is also larger than that of the inner disk. Possible explanations to this 'U' shape M/L profile could be stellar radial migration or the stellar halo contamination.

1.4 Thesis outline

The whole thesis is motivated by understanding the structure of disk galaxies and how they evolve to the current stage. In Chapter 2, we constructed a simple (CQ-Disk) model to highlight the marginal equilibrium state of the inner disk. The model is not supposed to solve the fundamental question about why and how stars are formed but instead to provide a constraint on the star and gas distribution and kinematics. The CQ-disk model would also give us a simple way to estimate quantities that are difficult to observe. In chapter 3 we investigate the outer disk, where the galaxy is supposed to be currently growing. We focus on the distribution of physical parameters such as stellar mass, SFR and mean stellar age. The physical parameters

derived from the SB profiles are model dependent but are more straightforward to compare with theoretical models and numerical simulations. We finally summarize the conclusions and implications from the thesis and propose possible future studies in Chapter 4. Images and radial profiles of the 700 galaxies studied in Chapter 3 are in the appendix.

Chapter 2

Equilibrium Star Formation In A Constant Q Disk: Model Optimisation and Initial Tests

2.1 Abstract

We develop a model for the distribution of the interstellar medium (ISM) and star formation in galaxies based on recent studies that indicate that galactic disks stabilise to a constant stability parameter, which we combine with prescriptions of how the phases of the ISM are determined and for the Star Formation Law (SFL). The model predicts the gas surface mass density and star formation intensity of a galaxy given its rotation curve, stellar surface mass density and the gas velocity dispersion. This

model is tested on radial profiles of neutral and molecular ISM surface mass density and star formation intensity of 12 galaxies selected from the THINGS sample. Our tests focus on intermediate radii (0.3 to 1 times the optical radius) because there are insufficient data to test the outer disks and the fits are less accurate in detail in the centre. Nevertheless, the model produces reasonable agreement with ISM mass and star formation rate integrated over the central region in all but one case. To optimise the model, we evaluate four recipes for the stability parameter, three recipes for apportioning the ISM into molecular and neutral components, and eight versions of the SFL. We find no clear-cut best prescription for the two-fluid (gas and stars) stability parameter $Q_{2\mathrm{f}}$ and therefore for simplicity, we use the Wang & Silk (1994) approximation (Q_{WS}). We found that an empirical scaling between the molecular to neutral ISM ratio (R_{mol}) and the stellar surface mass density proposed by Leroy et al. (2008) works marginally better than the other two prescriptions for this ratio in predicting the ISM profiles, and noticeably better in predicting star formation intensity from the ISM profiles produced by our model with the SFLs we tested. Thus in the context of our modeled ISM profiles, the linear molecular SFL and the two-component SFL (Krumholz et al., 2009b) work better than the other prescriptions we tested. We incorporate these relations into our 'Constant Q disk' (CQ-disk) model.

2.2 Introduction

The processes in the interstellar medium (ISM, or gas) that determine its distribution, structure, and the formation of stars are multiple, very complex, and operate on atomic to galactic size scales (see e.g. McKee & Ostriker , 2007). This makes it difficult to develop a comprehensive model for the distribution of gas and star formation in galaxies from first principles. Fortunately, normal galaxies are usually in a marginally stable equilibrium state. Here we use this fact as the basis of a model for the distribution of gas in galaxies, and with some additional assumptions we extend this into a model of the star formation distribution. Our aim is to construct an easy to implement model for the distribution of gas and star formation in galaxies that can be used to compare to observations and to easily create realistic simulated galaxies. Our approach also allows difficult to observe properties of galaxies (e.g. the molecular ISM distribution) to be inferred from those that are relatively easy to determine or infer (the stellar mass profile and rotation curve).

Star formation has long been believed to be related to disk (in)stability. Major studies (e.g. Toomre , 1964; Wang & Silk , 1994; Rafikov , 2001; Romeo & Wiegert , 2011; Elmegreen , 2011) have been carried out on gravitational disk stability since the 1960s and the theory of this subject is well developed. However, as early as 1972, Quirk claimed that the whole galactic disk should be marginally stable due to negative feedback mechanism. He used this assumption to predict the gas surface density profile; his model roughly matches the observations in the outer regions of

his sample galaxies but overestimates the densities in the inner half of the galaxies. Since then, observational evidence for Quirk's statement that disk galaxies are usually in a marginally stable state has mounted and been noticed in various studies (e.g. Kennicutt , 1989; van der Hulst et al. , 1993; Leroy et al. , 2008).

The gravitational stability parameter Q (see section 2.3.1 for details) for a single component thin disk was first derived by Toomre (1964). Kennicutt (1989) used a sample of tens of galaxies to show that there is very little star formation where Q is above some critical threshold. Martin & Kennicutt (2001) confirmed the result using more recent data. However a single fluid Q does not accurately indicate the stability of a real disk which contains both stars and gas. Jog & Solomon (1984) derived the two-fluid (stars and gas) stability parameter $Q_{2\mathrm{f}}$ for a thin disk. Rafikov (2001) improved the derivation by considering the stellar component as collisionless, yielding a rigorous but elaborate form of the stability parameter, Q_{R}. Wang & Silk (1994) proposed an approximation for the two-fluid stability parameter, Q_{WS}, which is widely used because of its simple form. More recently, Romeo & Wiegert (2011) reexamined the Wang & Silk (1994) approximation and gave a simple but more accurate effective two-fluid stability parameters for both an infinitesimally thin ($Q_{\mathrm{RW,thin}}$) and finite thickness ($Q_{\mathrm{RW,thick}}$) galactic disks.

Inspired by the Quirk (1972) and recent studies on disk stability theory and star formation laws, we develop and test the 'Constant Q disk' (CQ-disk) model, which we define as: A two-fluid (gas+stars) axisymmetric thin disk will evolve into a marginally

stable state with a constant stability parameter Q_{2f} through out the galactic disk. The basic idea for this model is to use the constancy of the two-fluid stability parameter to predict the distribution of gas and then use empirical molecular-to-neutral gas ratio ($R_{\rm mol}$) relations and the best star formation law (SFL) to predict the distribution of neutral and molecular gas as well as star formation rate. Here we compare the observed distribution of the ISM, and star formation in a small sample of galaxies to our model in order to test our assumptions and to optimise the model by trialling different recipes for its key ingredients (Q_{2f}, $R_{\rm mol}$, and the SFL).

The outline of our paper is as follows: section 2.3 briefly introduces background information, e.g. the gravitational stability parameter, molecular-to-neutral gas ratio model, and star formation laws; section 2.4 presents the detailed model we construct; section 2.5 gives a brief description of our sample galaxies; section 2.6 shows the results; in section 2.7 we discuss the assumption and implications of our model; and in section 2.8 we discuss further tests and possible uses of our model.

Through out this paper, we are only concerned with the large scale star formation in the galactic disk, hence we suppose the disk is axisymmetric and focus on the radial profiles of various physical quantities. As our research progressed it became useful to divide the galactic disk in to three regions: central (within $0.3r_{25}$), intermediate ($0.3 \sim 1r_{25}$) and outer ($> r_{25}$), where r_{25} is the optical radius, defined by where the B band surface brightness reaches 25 mag arcsec^{-2}. In general, our model works best in the intermediate radii, and much of the testing of the model is limited to

these radii. The profiles we create often do not match the observations in detail in the central region, although, as we will show, the match to quantities integrated over the central region is reasonable. We can not test our star formation models in the outer disk because the star formation intensity was not measured beyond r_{25} in our data sources. In Meurer et al. (2013) we discuss the expected ISM structure in the outer disk. There we showed that a gas dominated constant Q outer disk should have a surface mass density fall-off with the same profile as the dark matter for systems with a flat rotation curve, thus explaining the close relationship between dark matter and HI (Bosma , 1981; Hoekstra et al., 2001; Hessman & Ziebart , 2011). The other reason that we make these divisions is that the RCs are generally more reliable in the intermediate disk: there are less or even no data points in the central regions, while often warps and asymmetries are present in the outer regions.

2.3 Background information

2.3.1 Brief introduction to the gravitational stability parameter

Toomre (1964) showed that galactic disks can be unstable to axis-symmetric perturbations, and that the stability of a thin disk to such a perturbation can be represented quantitatively in a single parameter Q. Following Toomre (1964), Wang &

Silk (1994), and Rafikov (2001), we express the stability parameter for a gaseous disk:

$$Q_g = \frac{\sigma_g \kappa}{\pi G \Sigma_g}, \tag{2.1}$$

where σ_g is the gas velocity dispersion. Typically σ_g is assumed to be constant (e.g. Leroy et al., 2008, hereafter L08), although observations show that it typically slowly varies with radius (e.g. Tamburro et al., 2009; O'Brien et al., 2010). G is the gravitational constant, Σ_g is the gas surface mass density and κ is the epicyclic frequency which can be calculated from the rotation curve using

$$\kappa = \frac{v}{r}\sqrt{2\left(1 + \frac{r}{v}\frac{dv}{dr}\right)}, \tag{2.2}$$

where v is the circular velocity of the gas at a distance r from the galactic centre. Toomre's Q parameter can be an indicator for widespread star formation: a large stability parameter ($Q_g > 1$) means that pressure and centrifugal forces are sufficient to support the disk and thus it is stable, while a small $Q_g (< 1)$ means the gravity exceeds the internal support and the disk will collapse, resulting in widespread star formation (Kennicutt , 1989; van der Hulst et al., 1993; Martin & Kennicutt , 2001).

For a single component stellar disk, we can use a similar parameter, Q_s, to indicate gravitational stability of the stars [1] :

$$Q_s = \frac{\sigma_{s,r} \kappa}{\pi G \Sigma_s}, \tag{2.3}$$

[1]This is originally defined as $Q_s = \sigma_{s,r}\kappa / 3.36 G \Sigma_s$ (Toomre , 1964; Binney & Tremaine , 2008), but redefined as the equation shown above by later authors e.g. Wang & Silk (1994); Rafikov (2001) in order to use a more consistent expression with regards to Q_g.

where Σ_s is the star surface mass density and $\sigma_{s,r}$ is the radial component of the stellar velocity dispersion (Jog & Solomon , 1984; Wang & Silk , 1994; Rafikov , 2001). We follow the estimation of $\sigma_{s,r}$ given by L08: assuming a typical fixed shape to the velocity dispersion ellipsoid, we have

$$\sigma_{s,r} = 1.67\sigma_{s,z}, \tag{2.4}$$

where $\sigma_{s,z}$ is the z-direction component of the stellar velocity dispersion and using the standard relationship between this, disk scale height h_s, and mass density for an isothermal disk (e.g. van der Kruit , 1988), we have

$$\sigma_{s,z} = \sqrt{2\pi G\Sigma_s h_s}. \tag{2.5}$$

Here h_s is assumed to be a constant through out the galaxy disk (e.g. as done by L08). Since, h_s is difficult to measure unless the galaxy is viewed edge-on, we follow L08 and use the exponential stellar disk's scale length, l_s, to estimate it. Using the average flattening ratio $l_s/h_s = 7.3 \pm 2.2$, measured by Kregel et al. (2002), we then obtain

$$\sigma_{s,r} \approx 1.55\sqrt{G\Sigma_s l_s}. \tag{2.6}$$

Galactic disks are composed of both gas and stars. Thus, we need to consider both of them in a more sophisticated disk stability theory. There have been numerous studies on the two-fluid disk stability theory and therefore different forms of two-fluid stability parameters, Q_{2f}. Here we introduce four of them:

Jog & Solomon (1984) explored the gravitational stability of a two-fluid thin disk. Later-on, Rafikov (2001) extended this work by treating the stellar part of the disk as collisionless and gave an explicit expression for the total stability parameter $Q_{\rm R}$:

$$\frac{1}{Q_R} = \frac{1}{Q_s}\frac{2}{1/q+q} + \frac{1}{Q_g}\frac{2}{yq+1/yq}, \tag{2.7}$$

where

$$y = \sigma_g/\sigma_{s,r}, \tag{2.8}$$

and $q = k\sigma_{s,r}/\kappa$, with k the wave number of the instability being considered. We take k to be the wavenumber of the most unstable mode in our calculations (L08). In this paper, we make a coarse searching through the parameter space of k and find the value which gives the lowest gas surface mass density. We find that the galaxies studied here have $\lambda = 2\pi/k = 2-5kpc$, consistent with the result of L08.

Although the Rafikov (2001) derivation of the two-fluid stability parameter is quite rigorous, it is complicated and wavenumber dependent, making it hard to use. Wang & Silk (1994) give a much simpler form, $Q_{\rm WS}$:

$$\frac{1}{Q_{\rm WS}} = \frac{1}{Q_g} + \frac{1}{Q_s}. \tag{2.9}$$

It is widely used by astronomers (e.g. Martin & Kennicutt , 2001) although the analysis deriving it has been criticised (Jog , 1996). Romeo & Wiegert (2011) improved the Wang & Silk (1994) approximation and proposed an effective Q parameter for a

two-fluid infinitesimally thin disk, $Q_{\rm RW,thin}$:

$$\frac{1}{Q_{\rm RW,thin}} = \begin{cases} \dfrac{W}{Q_s} + \dfrac{1}{Q_g} & \text{if } Q_s \geq Q_g\,, \\ \\ \dfrac{1}{Q_s} + \dfrac{W}{Q_g} & \text{if } Q_g \geq Q_s\,; \end{cases} \tag{2.10}$$

where

$$W(y) = \frac{2}{y + 1/y}, \tag{2.11}$$

and y is defined above in Eq. 2.8.

In reality, disks are not infinitesimally thin, and the thickness of the disk has a stabilising effect. Therefore, Romeo & Wiegert (2011) also give an expression for a disk of finite thickness, $Q_{\rm RW,thick}$:

$$\frac{1}{Q_{\rm RW,thick}} = \begin{cases} \dfrac{W}{T_s Q_s} + \dfrac{1}{T_g Q_g} & \text{if } \; T_s Q_s \geq T_g Q_g\,, \\ \\ \dfrac{1}{T_s Q_s} + \dfrac{W}{T_g Q_g} & \text{if } \; T_g Q_g \geq T_s Q_s\,; \end{cases} \tag{2.12}$$

where T is a factor, by which the stability parameter of each component increases, reflecting the effect of the thickness of the disk. The factor T depends on the ratio of vertical to radial velocity dispersion: $T = 0.8 + 0.7(\sigma_z/\sigma_r)$. So that we have $T_g \approx 1.5$ for gas, and $T_s \approx 1.22$ for stars.

Kennicutt (1989) showed that Q_g values for 15 disk galaxies are almost a constant. Similarly Meurer et al. (2013) used more recent measurements to show that Q_g is constant over a large fraction of the outer disks of galaxies where HI dominates the

mass. Boissier et al. (2003); Martin & Kennicutt (2001) tested the Wang & Silk (1994) $Q_{\rm WS}$ on more disk galaxies and got a similar result. L08 used the Rafikov (2001) $Q_{\rm R}$ in testing the star formation threshold for 23 nearby galaxies and get a remarkably flat $Q_{\rm R}$ thorough the optically bright part of galactic disks with $Q_{\rm R} \sim 1.3 - 2.5$.

One plausible explanation for this phenomena is self-regulation by star formation (Burton et al., 1992; Elmegreen, 2011): an unstable disk (low Q) will collapse and commence widespread star formation. The star formation will consume most of the gas in a short time (Quirk, 1972), also the resulting winds from high mass stars and supernovae explosions will expel part of the gas out of the galactic disk (Dutton, 2009; Heckman et al., 1990) and heat up the remaining gas (Tamburro et al., 2009). This will increase Q by lowering Σ_g and increasing σ_g and thus make the disk more stable. On the other hand, a stable disk (high Q) will have suppressed star formation because the gas can not collapse. This means less heating of the ISM through winds and supernovae, and hence a relative cooling and lowering of σ_g, thus decreasing Q.

Thus a negative feedback system is set up and it will finally come to a stable equilibrium state. Here we suppose that galaxies equilibrate to the same Q at all radii through this local feedback cycle: regions of low Q heat up locally due to feedback, while regions of high Q cool due to relative lack of star formation. We test whether Q is constant within the optically bright portion of galaxies, and consider whether Q may be constant within a galaxy, but vary from galaxy to galaxy. This might

happen if the balance in the local support between epicyclic frequency κ and velocity dispersion σ varies due to changes in the relative importance of angular momentum and feedback, perhaps due to initial mass function variations (Meurer et al., 2009) or metallicity dependent cooling.

2.3.2 Brief introduction to $R_{\rm mol}$ relations

It is useful to have an accurate prescription for determining the molecular to neutral ratio ($R_{\rm mol} \equiv \Sigma_{\rm H_2}/\Sigma_{\rm HI}$) because these phases of the ISM are measured with separate observations and because it is generally believed that star formation is more related to the the molecular rather than the atomic gas. In practice the molecular data has been more expensive to obtain than HI data and requires use of tracers of H_2 like CO emission. The advent of new facilities like SMA, CARMA and ALMA may change these economics.

Various simple prescriptions for determining $R_{\rm mol}$ have been raised in previous studies (cf. L08 and references therein). L08 used high quality HI and CO data to assess four of the most popular $R_{\rm mol}$ prescriptions and found two that worked well. The first is purely empirical and involves just the stellar surface mass density (we call this the SR relation or $R_{\rm mol,s}$)

$$R_{\rm mol,s} = \frac{\Sigma_s}{81\, M_\odot\, pc^{-2}}. \tag{2.13}$$

The other uses hydrostatic pressure P_h as a parameter (the PR relation or $R_{\rm mol,p}$)

and is

$$R_{\rm mol,p} = \left(\frac{P_h}{1.7 \times 10^4 \, cm^{-3} \, K \, k_B} \right)^{0.8}, \tag{2.14}$$

where P_h is given by Elmegreen (1989) as

$$P_h = \frac{\pi}{2} G \Sigma_g (\Sigma_g + \frac{\sigma_g}{\sigma_{s,z}} \Sigma_s), \tag{2.15}$$

where $\sigma_{s,z}$ can be calculated using Eq. 2.5. Although L08 found that P_h is not as good of a predictor of $R_{\rm mol}$ as the stellar surface mass density, it has a more solid physical basis (Wong & Blitz , 2002; Blitz & Rosolowsky , 2004, 2006; Elmegreen , 1989; Elmegreen & Parravano , 1994).

Another physically intuitive model is described by Krumholz et al. (2008, 2009a,b, hereafter KR relation or $R_{\rm mol,K}$) and tested by Krumholz & Gnedin (2011) using numerical simulations. In this model the molecular gas can only exist in a region well shielded from the UV radiation field. The approximate solution is

$$R_{\rm mol,K} = \frac{4 - 2s}{3s}, \tag{2.16}$$

(Krumholz & Gnedin , 2011), where

$$s = \frac{ln(1 + 0.6\chi + 0.01\chi^2)}{0.6\tau_c}, \tag{2.17}$$

and where χ is a dimensionless number representing the scaled radiation field,

$$\tau_c = \Sigma_g a_d / \mu_H, \tag{2.18}$$

where a_d is the dust cross section per hydrogen atom and $\mu_H = 2.3 \times 10^{-24} g$ is the mean mass per nucleus. Following Krumholz & Gnedin (2011), we take the

approximation that

$$\frac{\sigma_d}{10^{-21} cm^{-2}} = Z', \tag{2.19}$$

and

$$\chi \approx 3.1 \left(\frac{1 + 3.1 Z'^{0.365}}{4.1} \right), \tag{2.20}$$

with Z' being the metallicity normalised to the solar value. From Eq. 2.16 - 2.20 we expect some troublesome asymptotic behaviour in low density and low metallicity regions because a small τ_c ($\ll 0.5$) leads to a negative $R_{\rm mol,K}$. We therefore set negative $R_{\rm mol,K}$ values to zero in our code, which means there is no molecular gas in low density and low metallicity regions.

We test all three relations to estimate $R_{\rm mol}$ in our calculation (using the total gas surface mass density derived using our model, cf model description in section 2.4) and see which prescription best models the $\Sigma_{\rm HI}$ and $\Sigma_{\rm H_2}$ profiles.

2.3.3 Brief introduction to star formation laws

The SFL is usually defined as the relationship between star formation rate and ISM properties, especially density. The SFL allows one to calculate the star formation rate given gas density and some other galactic parameters or vice versa. This is usually expressed as the surface density of star formation, $\Sigma_{\rm SFR}$, defined as the SFR per unit area, or in other words the star formation intensity. There have been numerous SFLs and here we summarise and test the most popular ones in the literature (L08; Bigiel

et al. , 2008; Tan , 2010, and references therein).

2.3.3.1 Schmidt-Kennicutt Law

Probably the most well known and widely used SFL is the Schmidt-Kennicutt Law (Schmidt , 1959; Kennicutt , 1998). It is a simple empirical correlation between star formation intensity and total gas:

$$\Sigma_{\rm SFR,SK} = A_{\rm SK} \left(\frac{\Sigma_g}{100 {\rm M}_\odot \, {\rm pc}^{-2}} \right)^N , \tag{2.21}$$

where $A_{\rm SK}$ is a coefficient with unit of $[{\rm M}_\odot \, {\rm kpc}^{-2} \, {\rm yr}^{-1}]$, Σ_g is the surface mass density of the gas (both neutral and molecular), and $N = 1.4 \pm 0.15$ (Kennicutt , 1998). Here we fix $N = 1.4$ in our tests of $\Sigma_{\rm SFR,SK}$.

2.3.3.2 Free-fall time scale with fixed scale height

The power law index N of Schimidt-Kennicutt Law is very close to 1.5, which can be explained by arguing that stars form in a free-fall time scale in a gas disk with fixed scale height: Since the free fall time scale $\tau_{\rm ff}$ is proportional to the inverse square root of the local gas density ρ_g, then for a fixed scale height h, the star formation intensity is (Leroy et al. , 2008):

$$\Sigma_{\rm SFR} \propto \frac{\Sigma_g}{\tau_{\rm ff}} \propto \frac{\rho}{\rho^{-0.5}} \propto \Sigma_g^{1.5}. \tag{2.22}$$

Therefore the star formation intensity in a free-fall timescale with fixed scale height can be written as

$$\Sigma_{\rm SFR,ff} = A_{\rm ff}\left(\frac{\Sigma_g}{100{\rm M}_\odot\,{\rm pc}^{-2}}\right)^{1.5}, \tag{2.23}$$

where $A_{\rm ff}$ has the same unit as $A_{\rm SK}$. So this version of the SFL is nearly the same as the Schmidt-Kennicutt SFL with a slightly higher $N = 1.5$.

2.3.3.3 Free-fall timescale with variable scale height

If the disk scale height is not fixed but set by hydrostatic equilibrium, then the star formation law (still assuming stars form in disk free-fall time scale) is (Leroy et al. , 2008)

$$\Sigma_{\rm SFR,ff'} = A'_{\rm ff}\left(\frac{\Sigma_g}{100{\rm M}_\odot\,{\rm pc}^{-2}}\right)^2\left(1+\frac{\Sigma_s}{\Sigma_g}\frac{\sigma_g}{\sigma_{s,z}}\right)^{0.5}\left(\frac{11km/s}{\sigma_g}\right), \tag{2.24}$$

where $A'_{\rm ff}$ has the same unit as $A_{\rm SK}$.

2.3.3.4 Orbital timescale

If we instead assume that a constant fraction of the ISM is consumed in a dynamical timescale, we would have

$$\Sigma_{\rm SFR,\Omega} = B_\Omega\Sigma_g\Omega, \tag{2.25}$$

where B_Ω is a dimensionless coefficient and Ω is the orbital angular frequency (Leroy et al. , 2008; Tan , 2010). Following the suggestion of this functional form by Silk

(1997) and Elmegreen (1997), Kennicutt (1998) showed that this form of the SFL was able to account for the star formation intensity in his sample of normal galaxies and circum-nuclear star burst, and worked equally well as $\Sigma_{\rm SFR,SK}$.

2.3.3.5 GMC collisions in a shearing disk

Tan (2000) presented a star formation model which assumes that star formation is triggered by GMC collisions in a shearing disk. This predicts that

$$\Sigma_{\rm SFR,CC} = B_{\rm CC} Q_g^{-1} \Omega (1 - 0.7\beta) \Sigma_g \quad (\beta \ll 1), \tag{2.26}$$

where $B_{\rm CC}$ is a dimensionless coefficient, $\beta \equiv d \ln v_{\rm circ} / d \ln r$ and $v_{\rm circ}$ is the circular velocity at a particular galactocentric radius r. Note $\beta = 0$ for a flat rotation curve. The GMC collision SFL is only meant to be valid in regions where a significant fraction of the gas is in gravitationally bound clouds, which typically means $\Sigma_{\rm H_2} \gtrsim \Sigma_{\rm HI}$. However, here we test it over a wider range of densities.

2.3.3.6 Linear molecular SFL

Leroy et al. (2008) and Bigiel et al. (2008) studied 12 nearby spiral galaxies at sub-kpc resolution and concluded that the SFR is proportional to the molecular content:

$$\Sigma_{\rm SFR,H2} = A_{\rm H_2} \left(\frac{\Sigma_{\rm H_2}}{100 {\rm M}_\odot \, {\rm pc}^{-2}} \right), \tag{2.27}$$

where the coefficient $A_{\rm H_2}$ has the same unit as $A_{\rm SK}$.

2.3.3.7 Turbulence-regulated SFL

Krumholz & McKee (2005) provided a turbulence-regulated star formation model to predict the SFR by assuming stars primarily form in molecular clouds that are virialised and supersonically turbulent and that the probability distribution of densities is lognormal. The intensity of star formation by their model is given by

$$\Sigma_{\rm SFR,KM} = A_{\rm KM} f_{\rm GMC} (\frac{\phi_{\bar{P}}}{6})^{0.34} (\frac{Q_g}{1.5})^{-1.32} (\frac{\Omega}{\rm Myr^{-1}})^{1.32} (\frac{\Sigma_g}{100 {\rm M_\odot\,pc^{-2}}})^{0.68}, \qquad (2.28)$$

where the coefficient $A_{\rm KM}$ has the same unit as $A_{\rm SK}$, $f_{\rm GMC}$ is the mass fraction of gas in giant molecular clouds (GMCs) and can be approximated as $f_{\rm GMC} = R_{\rm mol}/(1+R_{\rm mol})$, and $\phi_{\bar{P}} = 10 - 8 f_{\rm GMC}$ (Krumholz & McKee , 2005; Tan , 2010).

2.3.3.8 Two-component SFL

Krumholz et al. (2009b) presented a two-component star formation law,

$$\Sigma_{\rm SFR,KMT} = A_{\rm KMT} f_{\rm GMC} \left(\frac{\Sigma_g}{100 {\rm M_\odot\,pc^{-2}}} \right) \times \left\{ \begin{array}{ll} (\Sigma_g/\Sigma_0)^{-0.33}, & \Sigma_g < \Sigma_0 \\ (\Sigma_g/\Sigma_0)^{0.33}, & \Sigma_g > \Sigma_0 \end{array} \right\}, \quad (2.29)$$

where the coefficient $A_{\rm KMT}$ has the same unit as $A_{\rm SK}$, and $\Sigma_0 = 85\ {\rm M_\odot pc^{-2}}$ is a 'critical' gas surface mass density. In regions with $\Sigma_g < \Sigma_0$, GMCs have an internal pressure that far exceeds the ambient gas pressure and the star formation time scale is independent of the environment; whilst in regions with $\Sigma_g > \Sigma_0$, the star formation time scale depends on the metallicity and the clumping.

2.4 The Model

Our model requires at least three inputs: the rotation curve, gas velocity dispersion and the stellar mass distribution. The metallicity is also needed if using the KR relation (cf. 2.3.2). The basic assumption for our model is that the galactic disk is in a gravitationally marginal stable state and the $R_{\rm mol}$ relations and SFLs are valid for all the galaxies.

Our algorithm is as follows:

1). Determine the radial total gas distribution ($\Sigma_g(r)$) assuming a marginally stable disk.

We make the assumption that the two-fluid stability parameter , $Q_{\rm 2f}$, is constant through out the whole galactic disk. We test all four two-fluid stability parameters ($Q_{\rm R}$, $Q_{\rm WS}$, $Q_{\rm RW,thin}$, $Q_{\rm RW,thick}$, cf section 2.3.1) on our sample galaxies and pick out the one most suitable for our model and then adopt it for all further calculations. We define 'most suitable' in the first place as having the flattest Q profile with the smallest rms deviation over all or most of the sample galaxies, and as a secondary consideration the simplest form.

Based on eq. (2.1)-(2.12), we calculate the gas surface mass density Σ_g from the rotation curve $v(r)$, gas velocity dispersion and stellar surface mass density Σ_s by fixing the stability parameter $Q_{\rm 2f}$ to the average value at intermediate radii.

2). Determine the radial molecular ($\Sigma_{\rm H_2}(r)$) and neutral ($\Sigma_{\rm HI}(r)$) gas distribution

We test three different ways to determine $R_{\rm mol}$: the SR, PR and KR relations

(cf. section 2.3.2). Once we have $R_{\rm mol}$ we determine the molecular gas surface mass density based on our model predicted $\Sigma_{\rm g}$ from step 1

$$\Sigma_{\rm H_2} = \Sigma_g \frac{R_{\rm mol}}{1+R_{\rm mol}}, \tag{2.30}$$

and neutral gas surface mass density

$$\Sigma_{\rm HI} = \Sigma_g \frac{1}{1+R_{\rm mol}}. \tag{2.31}$$

We then compare the derived molecular and neutral gas surface mass density to the observations to determine which $R_{\rm mol}$ relation fits the data best.

3). Determine the star formation intensity ($\Sigma_{\rm SFR}(r)$)

After obtaining the $\Sigma_{\rm HI}$ and $\Sigma_{\rm H_2}$, we use the SFL(s) introduced in section 2.3.3 to calculate the star formation intensity $\Sigma_{\rm SFR}$. Following Tan (2010), we fit each galaxy using every SFL described in section 2.3.3. The results are evaluated to determine which SFL(s) fit the observed $\Sigma_{\rm SFR}$ best so as to implement in future application of our model.

2.5 The Data

In order to construct our model, we need the following quantities as inputs: the rotation curve $v(r)$, the stellar surface mass density Σ_s, the gas velocity dispersion σ_g, and metallicity. Also, for comparison with the observations, we need data for the neutral gas surface mass density $\Sigma_{\rm HI}$, the molecular gas surface mass density $\Sigma_{\rm H_2}$ and the star formation intensity $\Sigma_{\rm SFR}$.

The best sample, which has all the data listed above, is a subset of the THINGS sample (L08; de Blok et al. 2008). It is composed of five dwarf galaxies (DDO 154, IC 2574, NGC 7793, NGC 2403, and NGC 925) and seven spiral galaxies (NGC 3198, NGC 4736, NGC 6946, NGC 3521, NGC 5055, NGC 2841, and NGC 7331). The Σ_s, $\Sigma_{\rm HI}$ and $\Sigma_{\rm H_2}$ are tabulated in the paper of L08, although the dwarf galaxies do not have CO data and thus do not have $\Sigma_{\rm H_2}$. The $v(r)$ is provided by de Blok et al. (2008).

L08 used a fixed value of $\sigma_g (= 11 km/s)$. However, in general σ_g is observed to vary in galaxies (Tamburro et al., 2009; O'Brien et al., 2010). Therefore, we tried both the measured σ_g and a fixed $\sigma_g = 11\,{\rm km/s}$ when calculating the $Q_{\rm 2f}$. The measured σ_g are from A. C. Primo & F. Walter (private communication) and plotted in Fig. 2.3

The metallicity data is taken from Moustakas et al. (2010). We use a linear fit for each galaxy based on its metallicity zero point and radial gradient (Kobulnicky & Kewley , 2004) provided by Moustakas (private communication). The solar metallicity is taken as $12 + \log({\rm O/H})$=8.69 (Moustakas et al., 2010; Asplund et al., 2009).

For the rotation curve $v(r)$, we fit the data using the universal rotation curve (URC) (Battaner & Florido , 2000; Persic et al., 1996). The URC can be parameterised as

$$v^2(r) = v_0^2 \beta \frac{1.97 x^{1.22}}{(x^2 + 0.78^2)^{1.43}} + v_0^2 (1-\beta)(1+a^2)\frac{x^2}{x^2+a^2}, \qquad (2.32)$$

where $x = r/r_{opt}$ is the radial variable. Nominally, r_{opt} is the radius encircling 83%

of the light, v_0 is the velocity at $r = r_{opt}$, while β and a are constants that depend on the luminosity. Here we keep the v_0, r_{opt}, β, and a as free parameters.

The rotation curve data and their URC fits are shown in Fig. 2.1. The main advantage of using such a smooth rotation curve fit is to have a well defined and realistic derivative of $v(r)$. This is important when calculating κ (eq. 2.2) and thus essential for any version of Q_{2f}. We note that an overly tight fit to all the kinks and wiggles in the rotation curve amplifies these features in the derivative, producing unrealistic results, especially when the fitted $v(r)$ profile declines faster than Keplerian. It is likely that these small amplitude variations in $v(r)$ result from noise in the data and small scale non-circular motions due to bars, spiral arms, and asymmetries.

The URC parameters are fitted using the `MPFIT` software package (Markwardt , 2009) to $v(r)$. We also tried two other rotation curve parameterisations: the exponential form (L08) and the arctan form (Courteau , 1997). Generally, the URC model fits the data best, therefore we use the URC fit for all the rotation curves in this paper. The URC model fitting sometimes results in unphysical parameters (e.g. the fitted $R_{\rm opt}$ of DDO 154 is 12.1 kpc, far greater than the observation, 1.2 kpc; L08), but we use them anyway because we are only concerned with getting a smooth form which can best represent the data.

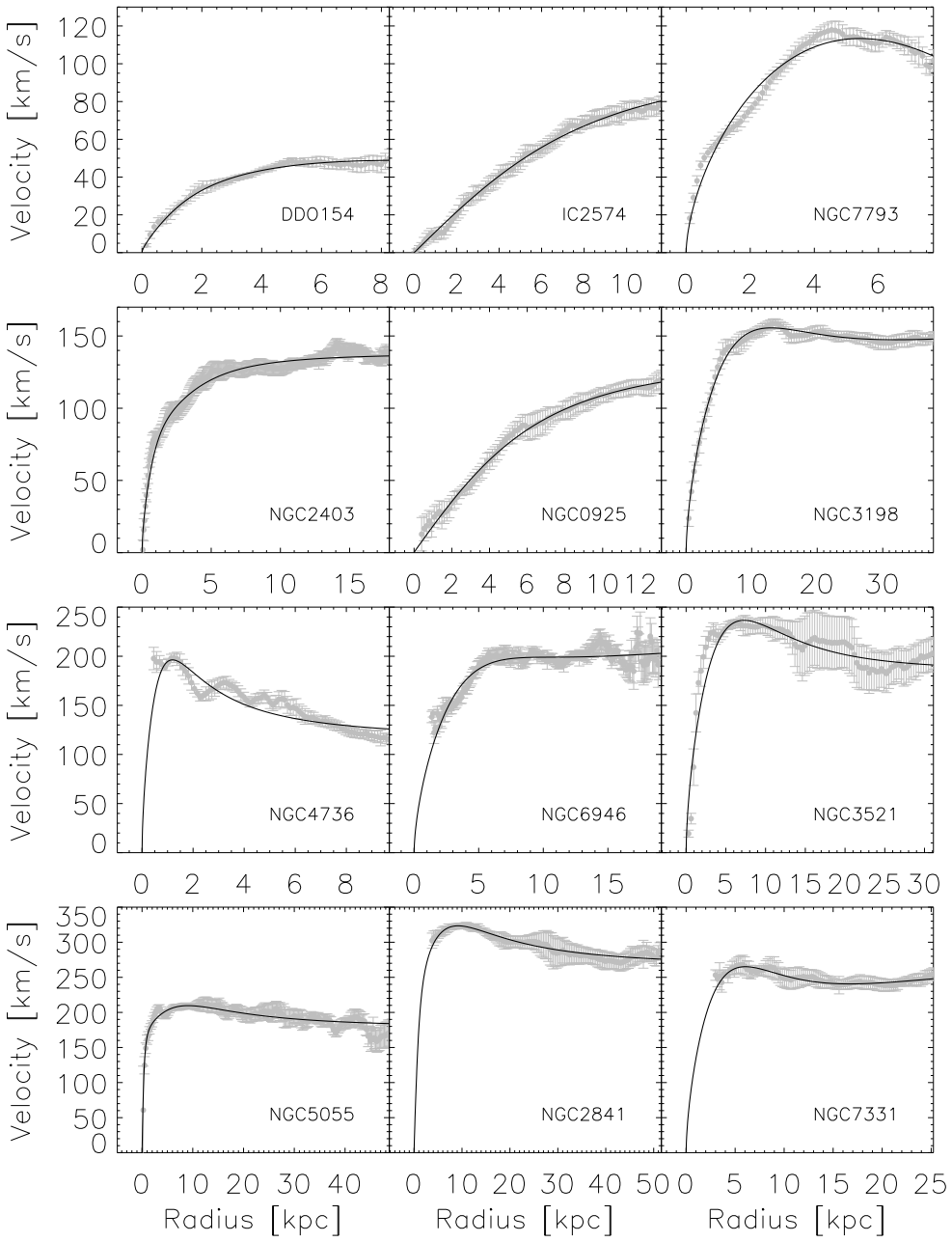

Figure 2.1: Rotation curve data and URC fitting. The grey dots with error bars are measured rotation curve data with uncertainty and the black solid lines are the URC fits.

2.6 Results

2.6.1 The two-fluid stability parameter Q_{2f}

The four two-fluid Q models are fitted to a constant (in forms of $\log Q$) using the `MPFIT` software package. In order to assess the quality of the fit we use the "deviation value" ϵ_Q which we define as

$$\epsilon_Q = \sqrt{\frac{1}{N_{\rm ann}-1}\sum_{i=1}^{N_{\rm ann}}\left(\log\frac{Q_{\rm model}}{Q_{\rm obs}}\right)^2}, \tag{2.33}$$

where $N_{\rm ann}$ is the number of valid annuli in the galaxy. ϵ_Q has units of dex; values of ϵ_Q closest to zero indicate the model that most closely represents the observations. The fitted values and their corresponding deviation values are shown in Table 2.1. Because the observed Q_{2f} are less constant in the central and outer regions, we only use the data within the intermediate disk during the fitting. In terms of flatness, the average ϵ_Q listed at the bottom of the Table 2.1 indicate that $Q_{\rm R}$ is marginally the best recipe, followed by $Q_{\rm RW,thick}$, $Q_{\rm WS}$, and $Q_{\rm RW,thin}$. It is satisfying that the form of Q_{2f} that is most rigorously defined yields the lowest average ϵ_Q, because it suggests that the feedback processes are truly working to maintain disks at a constant stability, at least over the intermediate radii. But since all these Q_{2f} recipes result in typically a factor of ~ 1.6 deviations about the mean, we choose to use $Q_{\rm WS}$ in our calculations as the easiest to implement, and sufficient for our purposes.

Figure 2.2 shows $Q_{\rm WS}$ for each galaxy using two cases for the gas velocity dis-

Table 2.1: Q_{2f} model fit results and galaxy properties

Galaxy	$N_{\rm ann}$	Q_R	$\epsilon_{Q_{\rm R}}$	$Q_{\rm WS}$	$\epsilon_{Q_{\rm WS}}$	$Q_{\rm RW,thin}$	$\epsilon_{Q_{\rm RW,thin}}$	$Q_{\rm RW,thick}$	$\epsilon_{Q_{\rm RW,thick}}$	V_m [km/s]	$\log(M_S)$ [$\log M_\odot$]	$\log(M_g)$ [$\log M_\odot$]	$\frac{\rm SFR_{cen}}{\rm SFR_{int}}$
DDO154	4	3.50	0.10	2.80	0.10	3.26	0.16	4.48	0.19	50.00	7.10	8.70	0.20
IC2574	27	1.46	0.21	1.26	0.20	1.30	0.21	1.84	0.21	134.00	8.70	9.30	0.13
NGC7793	22	1.77	0.19	1.70	0.21	1.79	0.18	2.34	0.19	115.00	9.50	9.10	0.55
NGC2403	33	1.96	0.18	1.89	0.20	1.98	0.17	2.61	0.17	134.00	9.70	9.50	0.49
NGC0925	22	1.82	0.22	1.36	0.23	1.44	0.27	1.98	0.25	136.00	9.90	9.82	0.43
NGC3198	14	1.82	0.16	1.42	0.15	1.58	0.23	2.09	0.21	150.00	10.10	10.12	0.37
NGC4736	16	1.85	0.27	1.73	0.29	1.78	0.28	2.20	0.29	156.00	10.30	8.95	3.45
NGC6946	24	1.55	0.26	1.21	0.31	1.53	0.23	2.05	0.20	186.00	10.50	10.01	0.31
NGC3521	18	1.57	0.17	1.19	0.21	1.50	0.20	1.99	0.19	227.00	10.70	10.15	0.66
NGC5055	25	1.67	0.18	1.31	0.28	1.69	0.20	2.29	0.16	192.00	10.80	10.25	0.83
NGC2841	15	3.99	0.17	2.52	0.19	2.94	0.21	3.66	0.20	302.00	10.80	10.11	0.14
NGC7331	20	1.86	0.13	1.33	0.16	1.67	0.22	2.20	0.20	244.00	10.90	10.25	1.04
Mean		2.07	0.187	1.64	0.211	1.87	0.213	2.48	0.205	168.83	10.45	9.93	0.72

Note – Four forms of stability parameters ($\log Q$) are calculated using a fixed $\sigma_g = 11km/s$ and then fitted using a constant. Only the intermediate disk data is used during this fitting. The fitted value and the corresponding deviation value, ϵ, for each galaxy are tabulated here. The maximum velocity V_m, total stellar mass M_S, total gas mass M_g and the ratio between the integrated central disk SFR and intermediate disk SFR SFR_{cen}/SFR_{int} are also tabulated here (data from L08). The galaxies are listed in ascending order of total stellar mass $\log(M_s)$.

persion: a fixed σ_g(=11km/s; L08) and the measured σ_g. Apparently, there is little difference in these two situations. Furthermore, we calculate the σ_g needed to maintain a constant $Q_{\rm WS}$ and plot it on top of the measured σ_g in Figure 2.3. In most cases or at nearly all radii, the needed σ_g is within 1σ uncertainty of the data and very close to a constant $\sigma_g = 11km/s$ as well. Therefore, in order to keep the simplicity of our model, we use the fixed $\sigma_g(= 11km/s)$ in the following calculations.

2.6.2 Neutral and molecular hydrogen content

We next calculate the neutral and molecular gas surface densities using the three $R_{\rm mol}$ relations: SR, PR and KR (cf. section 2.3.2). We use the fitted $Q_{\rm WS}$ values tabulated for each galaxy in Table 2.1 to derive the gas distribution. The calculated $\Sigma_{\rm HI}$ and $\Sigma_{\rm H_2}$ radial profiles are shown in Fig. 2.4 and Fig. 2.5 respectively. We calculate deviation values $\epsilon_{\rm HI}$ and $\epsilon_{\rm H2}$ for the three $R_{\rm mol}$ relations ($\epsilon_{\rm HI,SR}$, $\epsilon_{\rm HI,PR}$, etc.) using equations analogous to Eq. 2.33 to compare how well the $\Sigma_{\rm HI}$, and the $\Sigma_{\rm H_2}$ observations and model agree. A cursory comparison of Fig. 2.4 with Fig. 2.5 suggests that the HI profiles do not fit the data as well as the H_2 profiles. However, this is largely illusory - the $\Sigma_{\rm HI}$ profiles are much flatter than the $\Sigma_{\rm H_2}$ profiles for which a larger display range is required. Comparison of the $\epsilon_{\rm HI}$ and $\epsilon_{\rm H_2}$ values in Table 2 demonstrate that in general the HI profiles are fit by the model about as well or better than the H_2 profiles. All three $R_{\rm mol}$ model predictions agree with the data (cf. Table 2.2) reasonably well with the average $\epsilon_{\rm HI} \leq 0.19$ and the average

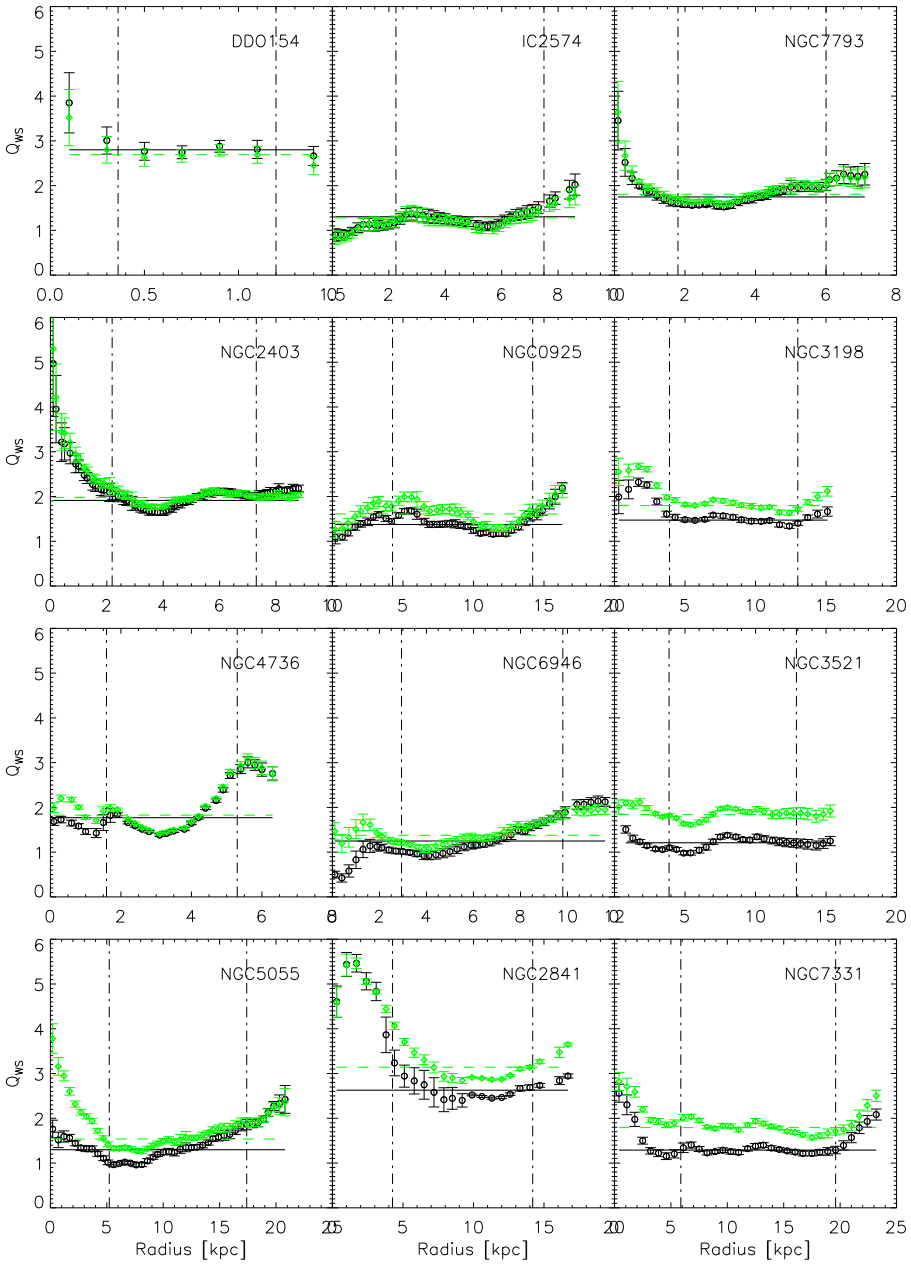

Figure 2.2: $Q_{\rm WS}$ radial profiles. Black open circles are $Q_{\rm WS}$ calculated using $\sigma_g = 11km/s$ and black solid lines are their best constant fit; green open diamonds are $Q_{\rm WS}$ calculated using measured σ_g, and green dash lines are their best constant fit. Error bars show 1σ uncertainty.

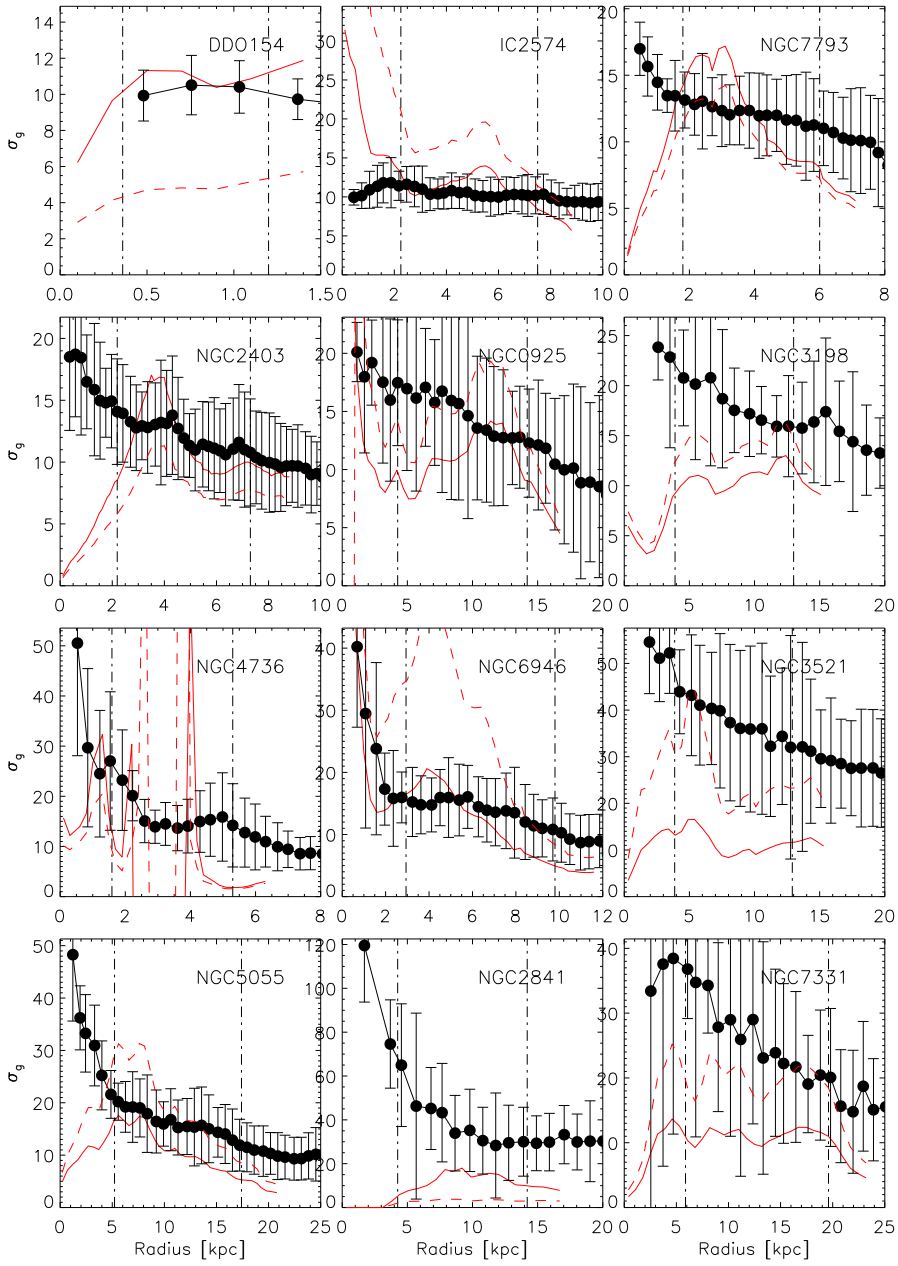

Figure 2.3: Gas velocity dispersion σ_g needed in order to keep a constant $Q_{\rm WS}$ with observed rotation curve and Σ_g and Σ_s. Red solid and dashed lines are the needed gas velocity dispersion calculated using the average $Q_{\rm 2f}$ value for the particular galaxy from Table 2.1 and a fixed $Q_{\rm WS} = 1.65$ respectively. Measured gas velocity dispersion with 1σ uncertainty are also over-plotted as black dots and error bars. The σ_g data are from Primo & Walter (private communication).

$\epsilon_{\rm H2} \leq 0.29$, equivalent to fractional errors better than 0.6 and 0.9 respectively. The KR relation is the best in terms of the $\epsilon_{\rm HI}$ values and the SR relation is the best in terms of $\epsilon_{\rm H_2}$ values. However, in some low metallicity regions and/or galaxies (e.g. DDO 154 and IC 2547) the KR relation results in no molecular gas. We do sometimes have a very bad fit (e.g. $\Sigma_{\rm HI}$ of NGC 2841) or even failure (e.g. $\Sigma_{\rm HI}$ of NGC 4736). The failure is caused by the big dip in the measured $Q_{\rm WS}$ curve (Fig. 2.2) which means the disk is already nearly unstable from just the stars.

The predicted HI surface mass density is usually flat over the radii considered here, but the model sometimes has a big divergence from the data in the outer regions where the observed HI has a steep decline, e.g. in NGC 925 and NGC 6946.

Note that the $R_{\rm mol}$ relations are tested using our CQ-disk model predicted $\Sigma_{\rm g}$, not the observed total gas surface mass density. The best $R_{\rm mol}$ relation we find here need not necessarily be the best one would find when applying to observed ISM profiles. However, our results are consistent with those of L08, who found the SR relation best in determining the molecular contents using observed values.

2.6.3 Star formation rate

Following Tan (2010), we test all SFLs introduced in section 2.3.3 using the derived $\Sigma_{\rm HI}$ and $\Sigma_{\rm H_2}$ (cf. section 2.6.2) as the input gas surface mass density values. For each galaxy, we derive the best-fit coefficients (e.g. $A_{\rm SK}$, B_Ω, etc.) for these SFLs and measure the resultant uncertainty, ϵ_{SFR}, which is defined in a similar way

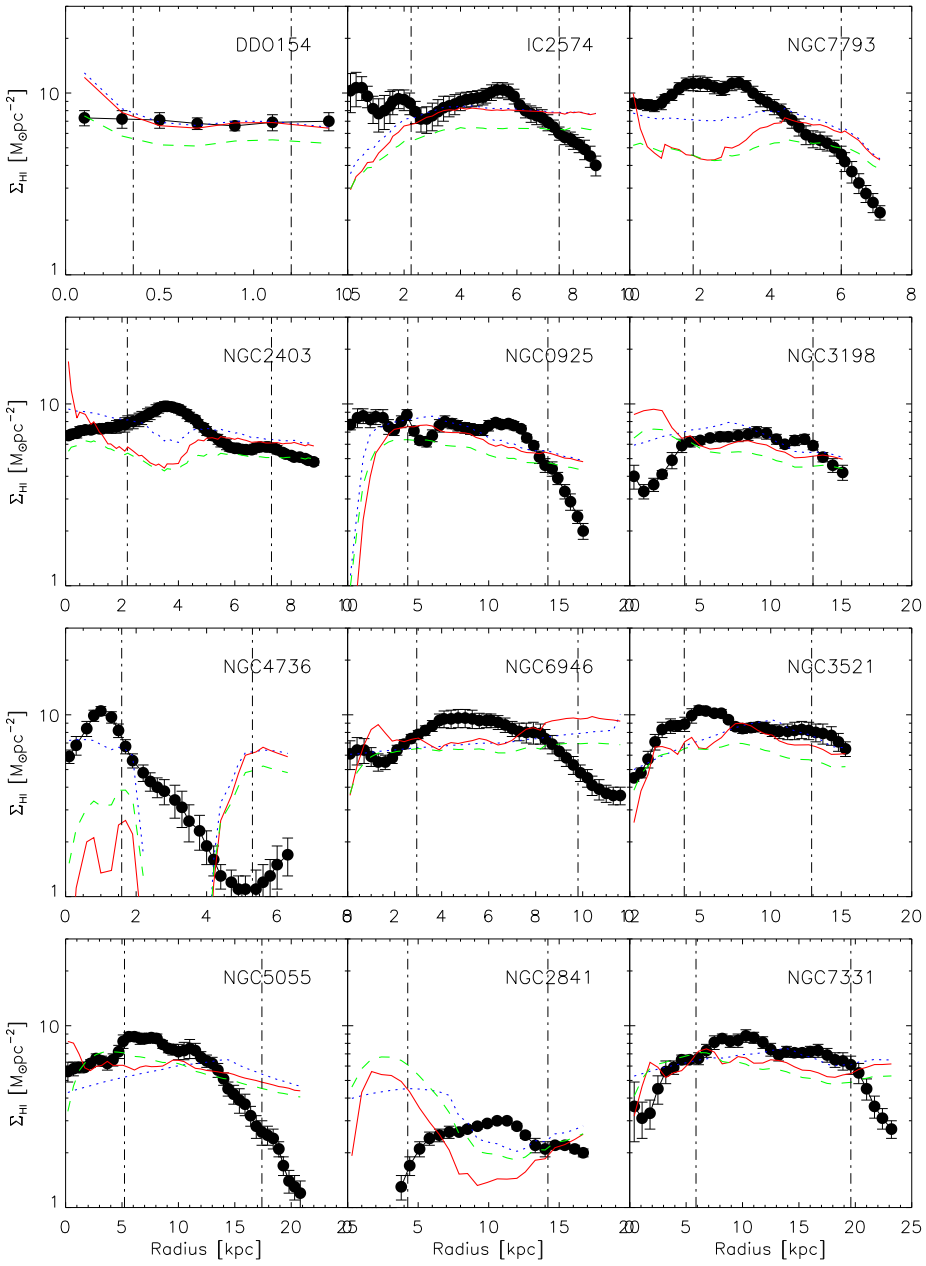

Figure 2.4: The $\Sigma_{\rm HI}$ radial profiles. Black dots and error bars are measured data with 1σ uncertainty; and red solid, green dash and blue dot lines are model derived $\Sigma_{\rm HI}$ using SR, PR and KR $R_{\rm mol}$ relations (cf. section 2.3.2) respectively.

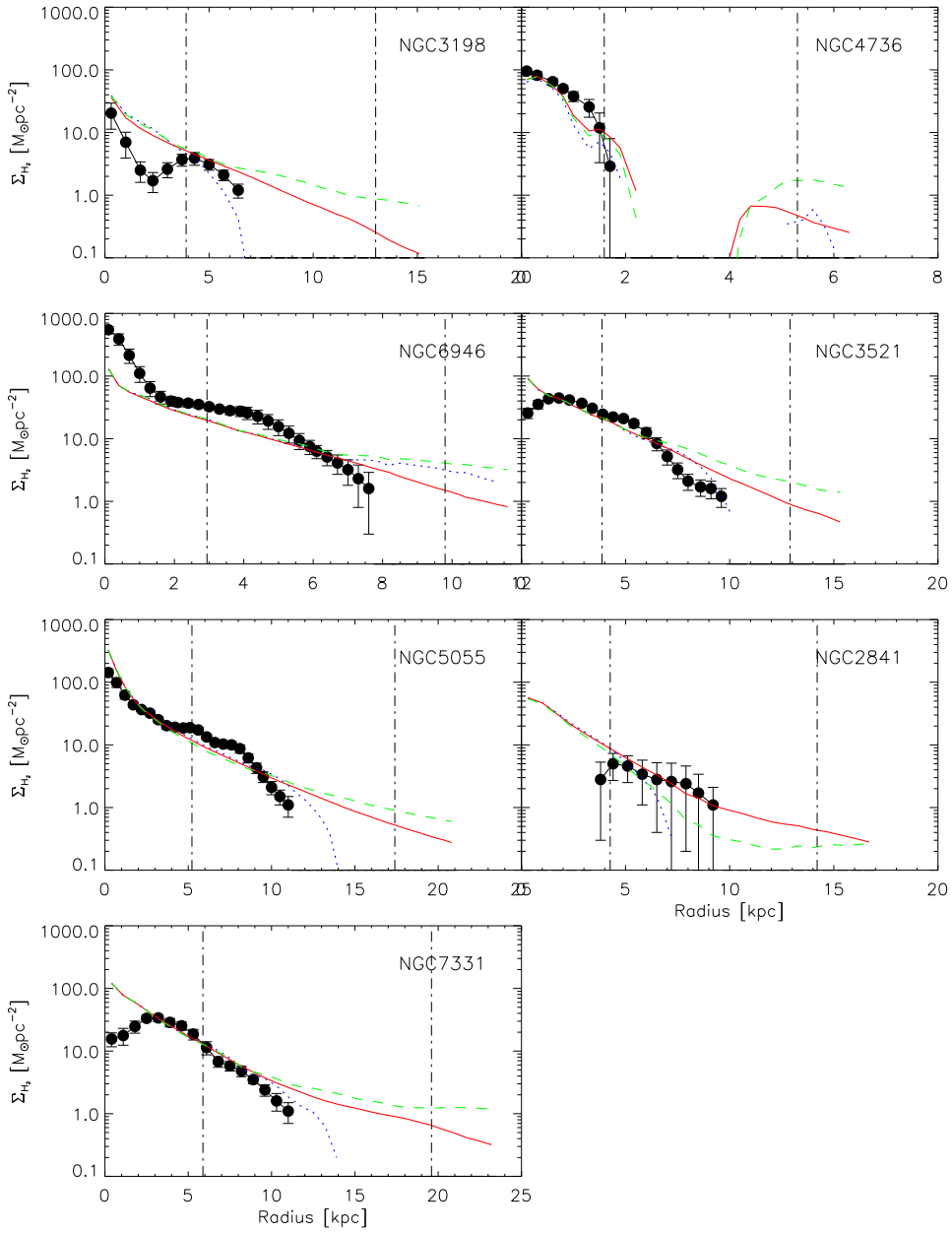

Figure 2.5: The Σ_{H2} radial profiles. Conventions follow Fig.2.4. There are only 7 galaxies shown here because we do not have CO data for the other 5 galaxies.

Table 2.2: Model-observation deviation for gas surface densities

Galaxy	$N_{\rm ann}$	$\epsilon_{\rm HI_{SR}}$	$\epsilon_{\rm HI_{PR}}$	$\epsilon_{\rm HI_{KR}}$
DDO154	4	0.02	0.13	0.02
IC2574	27	0.06	0.14	0.06
NGC7793	22	0.24	0.27	0.13
NGC2403	33	0.18	0.21	0.10
NGC0925	22	0.08	0.13	0.08
NGC3198	14	0.06	0.11	0.05
NGC4736	9	0.64	0.51	0.53
NGC6946	24	0.13	0.13	0.11
NGC3521	18	0.10	0.16	0.09
NGC5055	25	0.14	0.11	0.17
NGC2841	15	0.25	0.23	0.20
NGC7331	20	0.10	0.13	0.06
Median		0.13	0.14	0.10
Mean		0.17	0.19	0.14
		$\epsilon_{\rm H2_{SR}}$	$\epsilon_{\rm H2_{PR}}$	$\epsilon_{\rm H2_{KR}}$
NGC3198	4	0.20	0.24	0.31
NGC6946	17	0.23	0.26	0.24
NGC3521	12	0.24	0.35	0.21
NGC5055	12	0.20	0.25	0.20
NGC2841	8	0.13	0.38	0.47
NGC7331	8	0.21	0.25	0.17
Median		0.21	0.26	0.24
Mean		0.20	0.29	0.27

Note – ϵ is calculated for all three $R_{\rm mol}$ prescriptions. The upper half of this table is for $\Sigma_{\rm HI}$ and the lower half is for $\Sigma_{\rm H_2}$. There are less N_{ann} values in the lower half because there are fewer data points for Σ_{H_2}.

to Eq. 2.33. Since we have three different $R_{\rm mol}$ models, we also have three different sets of $\Sigma_{\rm HI}$ and $\Sigma_{\rm H_2}$ (cf. section 2.6.2) and therefore three different fitted SFL coefficients.The coefficients and the corresponding ϵ values are listed in Table 2.3 and 2.4. The resulting $\Sigma_{\rm SFR}$ profiles from the SFLs are plotted on top of the observed data in Figs. 2.6, 2.7, and 2.8.

Comparing the curves in Fig. 2.6, 2.7, and 2.8 the SFLs that depend on separating the molecular and neutral phases generally fit better than the SFLs that just depend on the total cool and cold ISM content. The predictions based on the SR relation performs better than PR and KR relations in terms of SFR predictions. The KR relation generally performs the worse in terms of SFR predictions. In addition, we see from Table 2.4 that the coefficient of the fit strongly correlates with stellar mass (as seen in the ordering of the table rows) when using the KR prescription for $R_{\rm mol}$. This means that SFL with this prescription is not universal. The $\epsilon_{\rm SFL}$ values in Tables 2.3 and 2.4 also support the view that the the molecular SFLs using the SR $R_{\rm mol}$ relation generally work the best. The exception to this rule is the dynamical time SFL ($\rm SFR_\Omega$) which outperforms the turbulence regulated molecular SFL ($\rm SFR_{KM}$) using the SR relation and all molecular SFLs using the PR and KR relation. However, the values in Tables 2.3 and 2.4 are the fit results using the intermediate radii data only. In terms of the simultaneous fit to all data points it is the third best SFL ($\epsilon_\Omega = 0.39$) following the linear molecular SFL (best, $\epsilon_{\rm H2} = 0.30$) and the two component SFL (second best, $\epsilon_{\rm cc} = 0.34$). This is slightly different from the results of Tan (2010)

who found the two component (KMT) SFL to be the best SFL in terms of rms dispersion. The best fit to all data for the linear molecular SFL yields a coefficient $A_{\rm H_2} = 9.51 \times 10^{-2}\,{\rm M_\odot\,yr^{-1}\,kpc^{-2}}$ using the SR relation. This is slightly higher than the L08 value, $(5.25 \pm 2.5) \times 10^{-2}\,{\rm M_\odot\,yr^{-1}\,kpc^{-2}}$, but well within its 2σ uncertainty. The higher coefficient implies 80% more efficient star formation and shorter molecular gas cycling times than those derived by L08.

Note that the GMC collision SFL is meant to be applied to molecular gas rich regions only (cf. section 2.3.3.5). It is therefore not surprising that our application of this SFL in regions that are not dominated by molecular gas, such as central region of NGC 2841, results in a poor match to the observed $\Sigma_{\rm SFR}$. Once more, one should bear in mind that the best SFL is selected based on our model predicted gas contents (Σ_g or $\Sigma_{\rm H_2}$). This is different from the standard approach of using the observed Σ_g or $\Sigma_{\rm H_2}$ to predict $\Sigma_{\rm SFR}$. Most of the best-fit SFL coefficients (A or B coefficients in Table 2.3 and 2.4), except the coefficient of the GMC collision SFL ($B_{\rm CC}$) and the coefficient of the KMT SFL ($A_{\rm KMT}$), are on the order of but a little bit larger than those of Tan (2010), who apply the SFLs onto observed gas surface mass densities. Since we have slightly different sample galaxies with Tan (2010), it is possible to have very different fitting values, however in fact, we do have similar $B_{\rm CC}$ and $A_{\rm KMT}$ values to those of Tan (2010) for galaxies in the overlapping part of our and Tan's sample. The model-observation deviation (ϵ values in Table 2.3 & 2.4) have similar situation: they are also generally larger than but on the order of those in Tan (2010, the χ

values). For example, for the galaxy NGC 7331, we find $\epsilon_{\rm SFR} = 0.056$ for the linear molecular SFL while Tan (2010) determines $\epsilon_{\rm SFR} = 0.0493$ for this SFL. However, the combination of the SR prescription for $R_{\rm mol}$ and the linear molecular SFL is claimed to provide the best results by L08, which is consistent with our results.

2.7 Discussion

2.7.1 Variations in $Q_{\rm 2f}$ and σ_g

The basic assumption of our model is that the two-fluid stability parameter $Q_{\rm 2f}$ is a constant. As we can see from Fig. 2.2, $Q_{\rm WS}$ is roughly constant, especially at intermediate radii. The variation can be large, up to a factor of 3 over the whole radial range sampled but the variations within the intermediate radii regions are smaller, less than a factor ~ 1.5 except for three cases NGC4736, NGC 6946, and NGC5055, where the variations are a factor of ~ 2 (see Table 2.1). There is also systematic variations with galactocentric radius: in 7/12 cases $Q_{\rm WS}$ rises towards the centre, sometimes quite sharply (NGC7793, NGC2403, NGC5055, NGC2841), while in 3/4 of the sample $Q_{\rm WS}$ increases at large radii, mostly beyond r_{25}. This systematic variation may cause over prediction of gas and SFR surface densities in the central and outer regions. A rapid central rise of $Q_{\rm WS}$ can have several explanations, which are discussed in section 2.7.2. The slow rise of $Q_{\rm WS}$ beyond r_{25} might be caused by undetected molecular gas in the outer disk, or may be due to the limited supply of

Table 2.3: Star Formation Law Parameters for Sample Galaxies (1)

Galaxy	$N_{\rm ann}$	$A_{\rm SK}$ (10^{-2})	$\epsilon_{\rm SFR_{SK}}$	$A_{\rm ff}$ (10^{-2})	$\epsilon_{\rm SFR_{ff}}$	$A_{\rm ff'}$ (10^{-2})	$\epsilon_{\rm SFR_{ff'}}$	B_{Ω} (10^{-3})	$\epsilon_{\rm SFR_{\Omega}}$	$B_{\rm CC}$ (10^{-3})	$\epsilon_{\rm SFR_{CC}}$
DDO154	4.	2.51	0.155	3.28	0.156	12.49	0.159	4.01	0.062	41.62	0.128
IC2574	27.	1.66	0.274	2.14	0.274	7.49	0.272	9.49	0.273	33.78	0.343
NGC7793	22.	6.84	0.491	8.86	0.489	32.29	0.484	11.61	0.458	42.52	0.577
NGC2403	33.	6.71	0.394	8.72	0.393	32.04	0.387	10.98	0.308	57.46	0.407
NGC0925	22.	3.30	0.200	4.27	0.194	15.42	0.167	20.39	0.204	64.03	0.273
NGC3198	14.	4.96	0.200	6.41	0.192	22.42	0.145	10.51	0.152	40.55	0.246
NGC4736	9.	12.38	0.838	12.65	0.856	14.13	1.394	0.63	1.077	14.77	1.293
NGC6946	24.	16.23	0.355	19.27	0.344	43.65	0.294	23.42	0.270	82.37	0.360
NGC3521	18.	5.43	0.401	6.43	0.379	14.31	0.257	6.91	0.296	20.21	0.399
NGC5055	24.	6.83	0.520	8.58	0.505	25.73	0.418	11.27	0.418	30.35	0.468
NGC2841	15.	5.79	0.341	7.18	0.390	20.22	0.676	3.50	0.375	26.96	0.605
NGC7331	20.	4.31	0.232	5.32	0.212	14.44	0.103	5.92	0.101	14.86	0.111
All	232	9.04	0.557	11.10	0.543	28.06	0.523	12.10	0.385	39.18	0.501
Median		5.79		7.18		20.22		10.51		40.55	
Mean		6.41		7.76		21.22		9.89		39.12	

Note – The fitted SFL coefficients and model-observation deviations: SK, Schimidt-Kennicutt Law; ff, free-fall time scale with fixed scale height; ff$'$, free-fall time scale with variable scale height; Ω, orbital time scale; CC, GMC collisions in a shearing disk. These five SFLs only depend on the total gas surface mass density and galactic dynamic parameters. The 'All' means the fitting using all valid data points from all the sample galaxies. All the 'A' coefficients have units of $M_{\odot}kpc^{-2}yr^{-1}$ and all the 'B' coefficients are dimensionless.

Table 2.4: Star Formation Law Parameters for Sample Galaxies (2)

R_{mol}	Galaxy	A_{H_2}	$\epsilon_{SFR_{H_2}}$	A_{KM}	$\epsilon_{SFR_{KM}}$	A_{KMT}	$\epsilon_{SFR_{KMT}}$
	(10^{-2})				(10^{-2})		
SR relation	DDO154	30.94	0.060	77.70	0.142	71.09	0.058
	IC2574	17.70	0.255	83.59	0.204	38.85	0.251
	NGC7793	13.22	0.169	40.33	0.291	29.35	0.168
	NGC2403	11.33	0.108	27.99	0.165	24.20	0.125
	NGC0925	9.83	0.195	61.09	0.165	20.74	0.232
	NGC3198	6.90	0.181	16.08	0.193	14.19	0.229
	NGC4736	11.49	0.459	1.19	1.654	11.71	0.651
	NGC6946	14.80	0.159	15.28	0.197	23.46	0.146
	NGC3521	5.02	0.167	4.08	0.090	7.83	0.095
	NGC5055	6.72	0.269	7.81	0.135	12.51	0.196
	NGC2841	3.75	0.296	4.96	0.827	7.25	0.485
	NGC7331	4.37	0.056	3.84	0.261	7.65	0.138
	All	9.51	0.300	8.37	0.642	15.61	0.334
	Median	11.33		16.08		20.74	
	Mean	11.34		28.66		22.40	
PR relation	DDO154	3.86	0.124	11.38	0.066	8.84	0.126
	IC2574	2.71	0.254	10.78	0.284	5.88	0.253
	NGC7793	8.03	0.432	19.49	0.494	17.80	0.428
	NGC2403	8.04	0.327	20.86	0.330	17.62	0.320
	NGC0925	4.83	0.140	30.42	0.163	10.45	0.133
	NGC3198	5.73	0.101	13.57	0.098	12.06	0.083
	NGC4736	11.67	0.832	1.18	1.926	11.90	1.040
	NGC6946	13.47	0.300	14.65	0.268	21.79	0.266
	NGC3521	4.56	0.309	3.90	0.194	7.28	0.228
	NGC5055	7.08	0.391	8.29	0.249	13.42	0.324
	NGC2841	4.82	0.565	5.64	1.116	9.01	0.770
	NGC7331	4.13	0.103	3.75	0.145	7.36	0.058
	All	8.66	0.440	8.13	0.503	15.08	0.407
	Median	5.73		11.38		12.06	
	Mean	6.58		11.99		11.95	
KR relation	NGC7793	76.85	0.396	223.23	0.426	167.85	0.406
	NGC2403	23.20	0.422	45.28	0.504	46.87	0.445
	NGC0925	15.66	0.254	98.27	0.230	32.49	0.259
	NGC3198	9.09	0.898	19.59	0.915	17.84	0.931
	NGC4736	12.46	0.454	1.18	1.499	12.71	0.647
	NGC6946	14.11	0.268	14.88	0.255	22.54	0.238
	NGC3521	5.07	0.193	4.08	0.206	7.83	0.204
	NGC5055	6.44	0.190	7.54	0.232	11.90	0.209
	NGC2841	3.60	0.637	4.62	0.869	6.80	0.732
	NGC7331	4.22	0.295	3.67	0.409	7.24	0.360
	All	9.38	0.441	8.18	0.639	15.10	0.475
	Median	12.46		14.88		17.84	
	Mean	17.07		42.23		33.49	

Note – The fitted SFL coefficients and model-observation deviations: H_2, linear molecular SFL; KM, turbulence-regulated SFL; KMT, two-component SFL. These SFLs depend on the molecular gas surface mass density and galactic dynamic parameters. Therefore we list fitted values for Σ_{H_2} calculated using both SR and PR relations. Results for the KR relation in DDO154 and IC2574 are omitted because eq. 2.16 yields non real results over much of these galaxies. All the 'A' coefficients have units of $M_\odot kpc^{-2} yr^{-1}$.

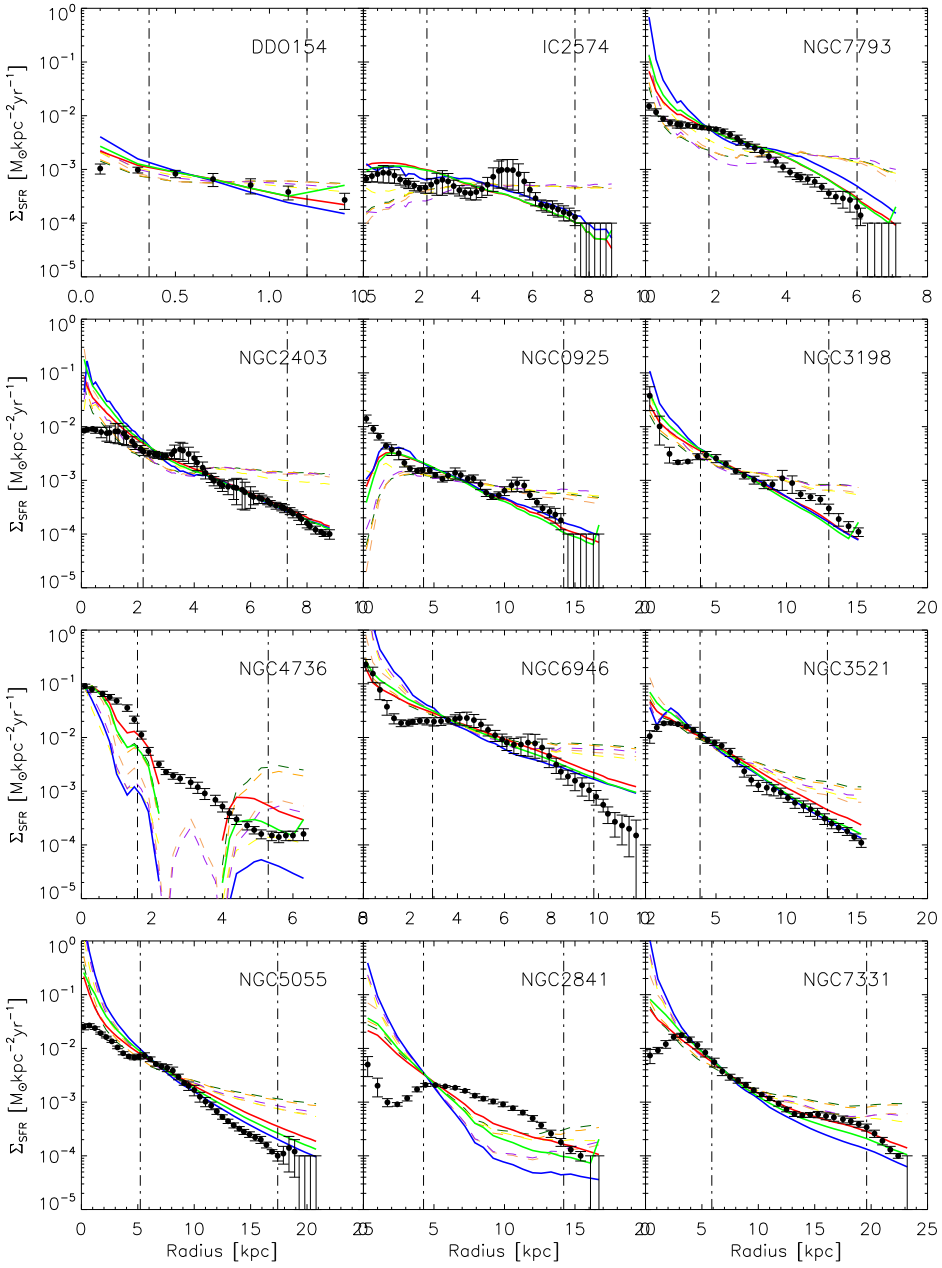

Figure 2.6: $\Sigma_{\rm SFR}$ radial profiles using the SR prescription for $R_{\rm mol}$. Black dots and error bars are measured $\Sigma_{\rm SFR}$ from L08. Thick solid lines are the three best fit SFLs: red, linear molecular SFL; blue, turbulence regulated SFL; green, two-component SFL. Dash lines are other SFL predictions: dark green, SK law; orange, free-fall with fixed scale height; sandy brown, free-fall with variable scale height; yellow, orbital time scale; purple, GMC collision.

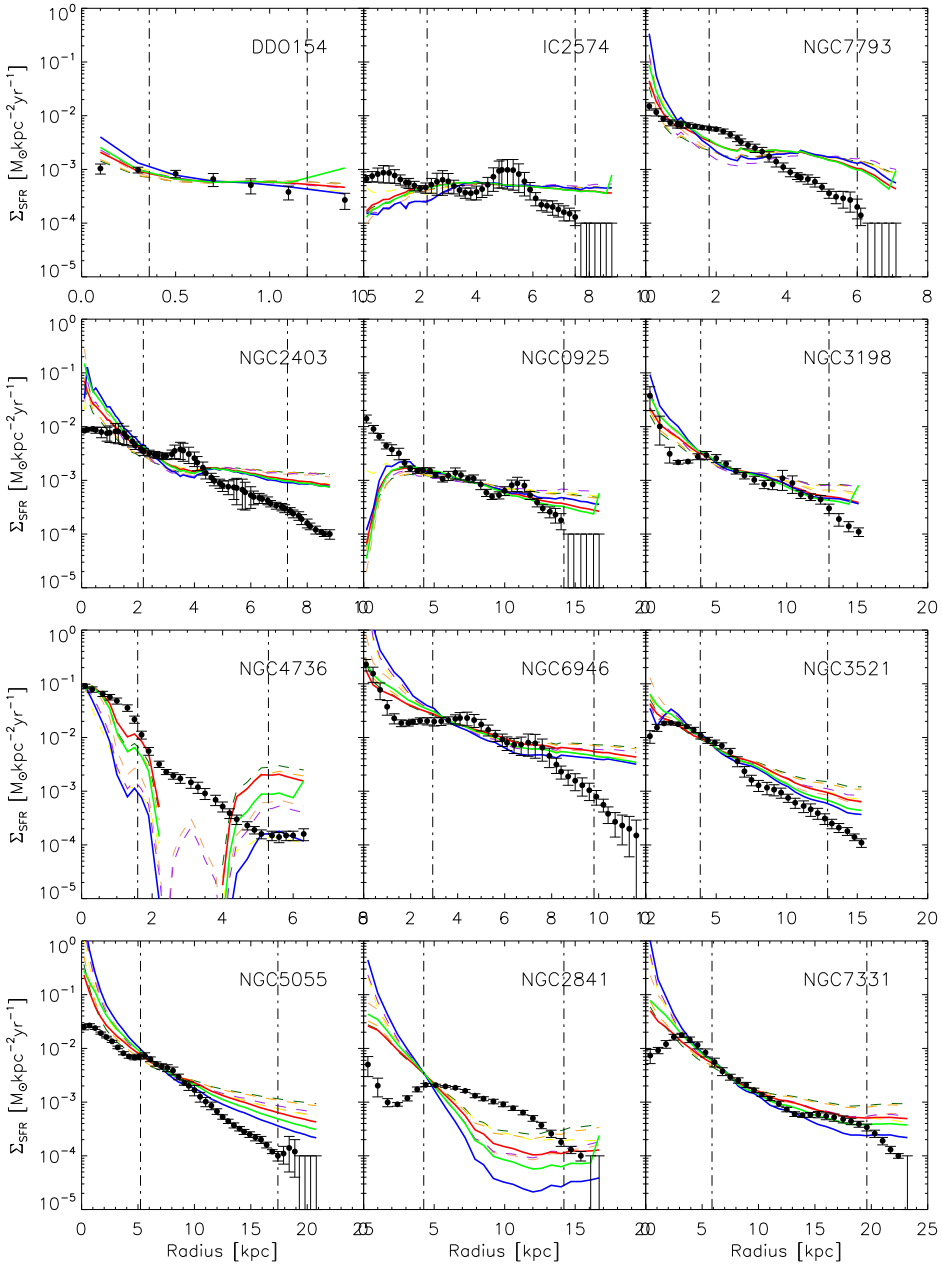

Figure 2.7: $\Sigma_{\rm SFR}$ radial profiles using the PR prescription for $R_{\rm mol}$. Conventions follow Fig.2.6.

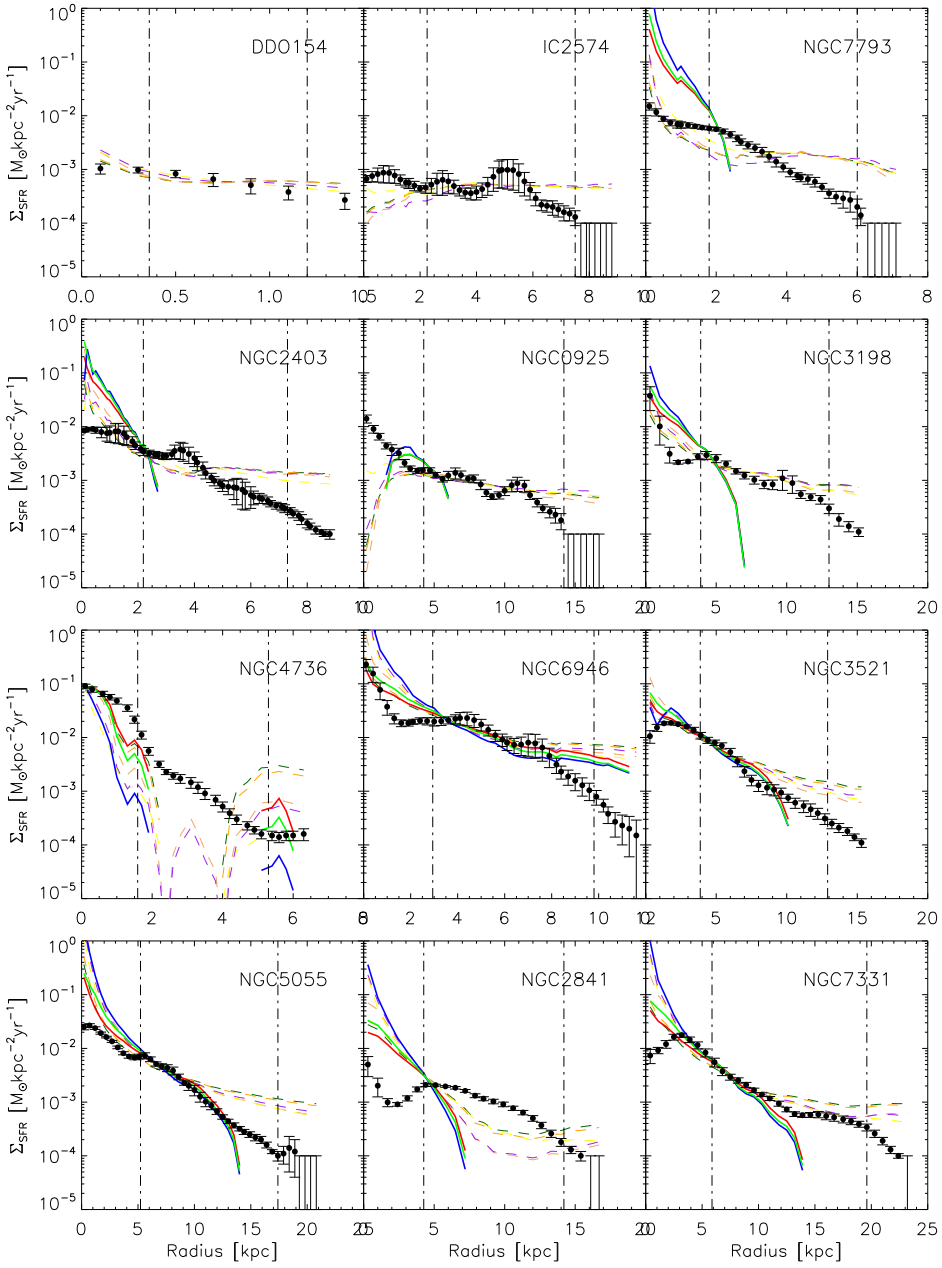

Figure 2.8: $\Sigma_{\rm SFR}$ radial profiles using the KR prescription for $R_{\rm mol}$. Conventions follow Fig.2.6.

ISM as pointed out by Meurer et al. (2013).

The gas velocity dispersion is hard to measure (Tamburro et al., 2009) and has large uncertainties (cf. Fig. 2.3). However, as shown in Fig. 2.2 the shape of the $Q_{\rm WS}$ profiles is not greatly affected by choosing a constant σ_g or adopting the observed σ_g profiles. In four cases (NGC3198, NGC3521, NGC2841, and NGC7331) the profiles are noticeably shifted vertically between the two options. This is because the measured σ_g is significantly higher than the assumed value of 11 km s^{-1}. We can also see from Fig. 2.3 that the σ_g needed to keep a constant $Q_{\rm WS}$ (using the observed Σ_s and Σ_g in Eq. 2.1, 2.3 and 2.9) is pretty constant and close to 11km s^{-1} and well within 2σ uncertainty of the measured gas velocity dispersion.

It might be surprising that $Q_{\rm WS}$ does not vary much no matter whether we use a constant $\sigma_g = 11{\rm kms}^{-1}$ or the measured σ_g. This is because the definition of $Q_{\rm WS}$ (eq. 2.9) is similar to the equivalent resistance of two resistors connected in parallel and Q_s is usually smaller than Q_g in the inner and intermediate disk regions. Thus, $Q_{\rm WS}$ is usually dominated by the Q_s value. This also illustrates that it is the total stability parameter, $Q_{\rm 2f}$, instead of Q_g that matters most and the interaction between gas and stars plays an important role in balancing the stability of galactic disk.

2.7.2 The central disk

Figures 2.7 - 2.8, suggest that our model overestimates Σ_g and/or $\Sigma_{\rm SFR}$ in the central disk for many of the sample galaxies. In e.g. NGC 2841, NGC 2403 and NGC

7331, the model overestimates Σ_g and $\Sigma_{\rm SFR}$ by more than an order of magnitude. This result is similar to that of Quirk (1972) although he used a different stability criterion (Goldreich & Lynden-Bell, 1965). Quirk (1972) argued that this is because the density-wave-induced shocks, which are very strong in the inner parts of the galaxy, make the gas in the post shock regions dense enough to be Jeans unstable. Thus their stability criteria, which does not consider shocks, may not be a good representation for the inner disk stability. However, our model does work well in the central part of other galaxies, e.g. NGC 7793, and furthermore, our model sometimes underestimates the central disk SFR of galaxies like NGC 6946 and NGC 925. Possible reasons for the model-observation discrepancy in the central disk could be the fitted functional form of the rotation curves are not good enough to represent the data (cf. section 2.7.3), or the central disk is not a suitable place to apply our model because it is dominated by a bulge instead of being pure disk.

Despite these complications and the poor fit to the central region in detail, Fig. 2.9 shows that the SFR integrated over the central region from our model agrees with the data to a similar level of accuracy as it does over the intermediate radii. The specific model we are using here employs the $Q_{\rm WS}$ recipe for $Q_{\rm 2f}$, the SR formulation of $R_{\rm mol}$, and the linear molecular SFL $\Sigma_{\rm SFR,H2}$. The relatively good agreement in the central region is because usually the model only fails badly in the very central part of the disk, typically covering an area less than 50% of the central disk. Therefore, the integrated SFR does not deviate from the observation very much. The exception to

this is NGC 2841, where the modelled SFR profiles shown in Figs. 2.6 - 2.8 deviate strongly from the observed over the entire central disk.

2.7.3 Effects of rotation curve parameterisation

Since Q is dependent on the derivative of the rotation curve (through κ), the precise shape of the smooth fit must have a quite strong effect on the result, especially in the inner region, where the rotation curve rises rapidly. In order to test this effect, we use the exponential parameterisation to fit the RC of NGC 2403 and use these new fitting results to recalculate the gas and star formation distribution. The results are shown in Fig. 2.10. The exponential form results in a shallower slope in the rising part of the RC and therefore a lowered gas and star formation surface density in the central region compared to the result of the URC fitting; whilst the URC form fitting results in a steeper slope and thus a higher gas and star formation surface density in the central region. As expected, different forms of RC fittings make little difference in the middle and outer disk for galaxies with a flat RC.

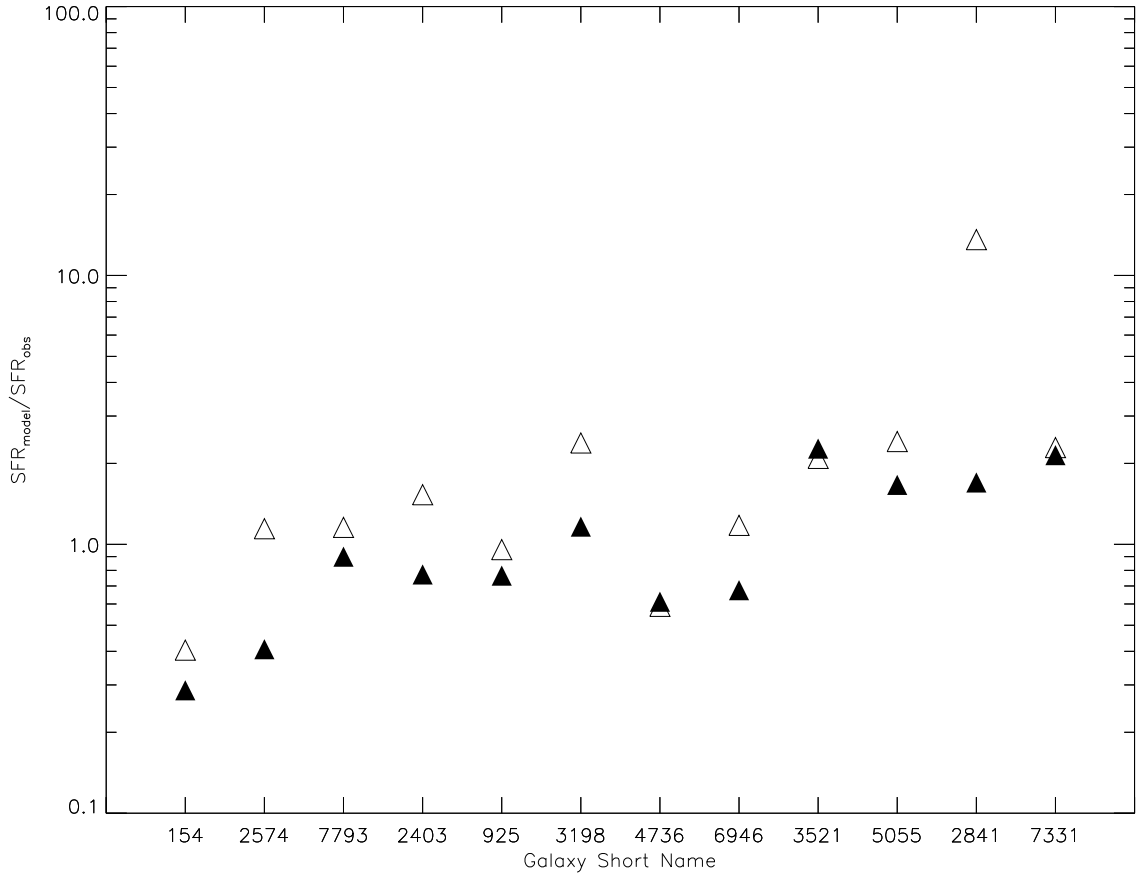

Figure 2.9: The ratio of $SFR_{\rm model}/SFR_{\rm obs}$. Solid symbols are for intermediate disk and open symbols are for central disk. The specific model we are using here is the $Q_{\rm WS}$ recipe for $Q_{\rm 2f}$, the SR formulation of $R_{\rm mol}$, and the linear molecular SFL $\Sigma_{\rm SFR,H2}$.

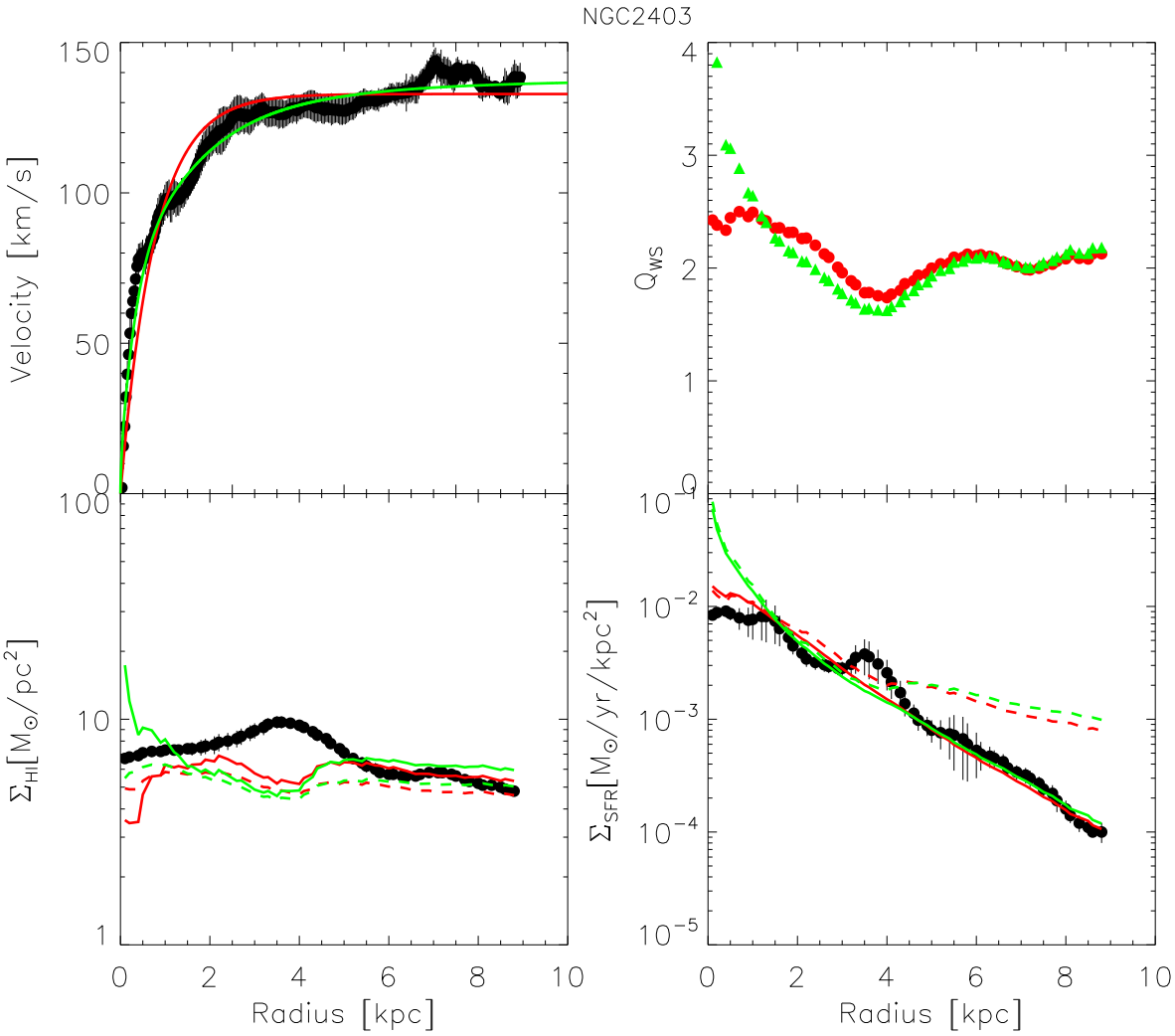

Figure 2.10: The effects on the results for NGC 2403 from using different rotation curve fitting functions. Upper-left panel: Rotation curve. Black dots with error bars are rotation curve data and uncertainties, the red solid line is the URC fit and the green solid line is the exponential rotation curve fit. Upper-right panel: Two-fluid stability parameter, $Q_{\rm WS}$. Red dots are calculated using the fitted URC form and green triangles are calculated using fitted exponential rotation curve. Lower-left panel is HI surface mass density and lower-right panel is SFR surface density. In these panels the black dots with error bars are measured data with uncertainties. The red lines are calculated using the fitted URC rotation curve and green lines are calculated using the fitted exponential rotation curve, in both cases the appropriate constant $Q_{\rm WS}$ is adopted. Solid lines are results using the SR prescription for $R_{\rm mol}$ and dash lines use the PR prescription. The SFL used here is the linear molecular SFL.

2.8 Tests and applications of the CQ-disk model

Examination of Figs. 2.4 – 2.8 and Tables 2.2 - 2.4 demonstrate that the CQ-disk model does a reasonable job (factor of ~ 2 agreement) of matching the overall shape of the HI, CO, and SFR radial profiles especially at intermediate radii. Figure 2.2 indicates that these radii are where Q_{2f} is not only fairly flat but at its minimum, i.e. the most unstable but uniformly so. This may be because at these radii star formation feedback is effective and the timescales for ISM flows are sufficient for profiles to evolve to nearly constant stability. As emphasised in sec 6.2, the model has the most difficulties fitting the detailed profiles in the central regions of galaxies, but still is fairly reasonable in predicting quantities integrated out to $r = 0.3r_{25}$.

Even at intermediate radii, the model curves do not match the profiles in close detail, with the observed profiles having small scale bumps, dips, and kinks. Often these local enhancements can also be seen in the profiles of Q_{2f}, HI, H_2, and SFR (e.g. the kinks in the profiles in IC 2574 and NGC 3521 at $R \sim 5.5$ kpc). These indicate that local enhancements in the gas density are reflected in the SFR profiles as expected by any reasonable SFL, but result in the Q profiles not being flat in detail. While disks may be evolving towards a uniform stability, local deviations may build up due to processes beyond the scope of this model (e.g. internal resonances, external perturbations, minor mergers). Hence the CQ-disk model is not as well suited to

modelling the details of individual galaxies as the overall structure of galaxies in general.

Our sample is relatively small. Further high quality observations would be useful to further test and optimise our model. New and developing generations of instrumentation including the JVLA, ASKAP, MeerKAT, Westerbork+APERTIF for HI observations, ALMA, CARMA, and SMA for CO (and thus H_2), WISE, PanSTARRS, LSST for modelling stellar content, combined with star formation surveys such as HAGS (James et al., 2004), SINGG (Meurer et al. , 2006), and 11HUGS (Kennicutt et al., 2008) as well as the wide availability of images of star formation from GALEX and WISE data mean that it will be possible to do studies similar to ours for well selected samples of hundreds or thousands of galaxies in the near future.

Examination of Figures 2.4 – 2.8 demonstrates that the various $R_{\rm mol}$ and SFL prescriptions diverge from each other the most in the outer and central regions of galaxies. For the reasons discussed in Sec. 6.2 the centre is more difficult to model. So we concentrate on how further study of LSB galaxies and outer disks may improve our model. The SR and PR recipes diverge from each other there because the former only depends on the stellar surface mass density, while the hydrostatic pressure used in the PR prescription becomes more dominated by gas. The metallicity dependence of the KR relation combined with the metallicity gradients typically seen in the bright parts of galaxies (Zaritskey et al., 1994; Kennicutt et al., 2003; Moustakas et al. , 2010) will also drive a radial gradient compared to the SR and PR prescriptions. LSB

regions are also important to test because of indications of low level star formation in extended UV disk galaxies (Thilker et al., 2005; Thilker et al. , 2007) and HI dominated regions (Bigiel et al. , 2010b). This low intensity star formation likely signifies IMF variations (Meurer et al. , 2009; Lee et al., 2009; Hunter et al., 2010; Gunawardhana et al., 2011) which should be incorporated in future versions of a more comprehensive CQ-disk model.

Comparison of the integrated HI mass and star formation rate may provide a sensitive test of our model since Figures 4, and 6-8 show that HI and star formation are largely segregated in galaxies, and the divergent behaviour of the various model profiles suggests that the HI/SFR ratio is likely to be dependent on the $R_{\rm mol}$ and SFL prescriptions. We will test this using data from the SINGG and SUNGG star formation surveys (Zheng et al. 2013, in prep).

The CQ-disk model may prove useful in galaxy simulations. For example, currently when generating the initial distribution of particles for N body simulations of interacting galaxies one often creates disks with the same scale length for stars and gas (e.g. Johansson, et al., 2009; Bekki & Couch, 2011) or giving the stellar disks exponential profiles with differing scale lengths (e.g. Lotz et al., 2008). Assuming a constant $Q_{\rm 2f}$ disk provides alternative easy to implement initial conditions for detailed simulations of galaxies. One could also use the CQ-disk model to enhance semi-analytic cosmological simulations, i.e. in a manner similar to that done by (Duffy et al., 2012a; Duffy et al. , 2012b) who modeled the detectability of galaxies in future

HI surveys. A similar application of the CQ-disk model will allow better HI line profile models, as well as models of H_2 (CO), and star formation in the same volume.

2.9 Summary

We have developed a simple 'constant Q disk' (CQ-disk) model for predicting the distribution of ISM and star formation in galaxies based on the assumption that the two-fluid instability parameter (Q_{2f}) of the galactic disk is a constant. The model predicts the gas surface mass density and star formation intensity given the rotation curve, stellar surface mass density and the gas velocity dispersion. In this paper we compared radial profiles of HI, and H_2 surface mass density and star formation intensity from a sample of 12 galaxies from L08. In order to optimise our model, we tried various prescriptions for calculating Q_{2f}, the ratio $R_{mol} = \Sigma_{H2}/\Sigma_{HI}$, and the star formation law (SFL). We find that

- The Q_{2f} profiles are fairly flat over the intermediate radii of the disk, with variations of a factor of ~ 1.6 about the mean, no matter which recipe of Q_{2f} is employed. The Rafikov (2001) formulation of Q_{2f} has the strongest physical basis of the recipes we tried, and also marginally the flattest Q_{2f} profiles. However it is the most difficult to implement since it requires the wavelength of the most unstable mode to be derived. The Wang & Silk (1994) approximation, is the most practical recipe for Q_{2f} in terms of its very simple form, and the one

we have adopted in our model.

- We tested three prescriptions of $R_{\rm mol}$ by comparing the observed surface mass densities of neutral and molecular gas with our model predictions. All three prescriptions produce $\Sigma_{\rm HI}$ and $\Sigma_{\rm H_2}$ profiles that match the observed profiles with typical variations better than a factor of 2 about the mean. Overall, the empirical scaling of $R_{\rm mol}$ with stellar surface mass density (SR) proposed by Leroy et al. (2008) produces the best fits to both the $\Sigma_{\rm HI}$ and $\Sigma_{\rm H_2}$ profiles, and therefore we favor this model. While the Krumholz et al. (2008, 2009a,b) self-shielding prescription KR produces typically better matches to the $\Sigma_{\rm HI}$ profiles than the SR relation, the matches to the $\Sigma_{\rm H_2}$ profiles are worse. Although the best $R_{\rm mol}$ relation selected here is based on the predicted $\Sigma_{\rm g}$ from our CQ-disk model, it is consistent with the L08 results based on observed neutral and molecular ISM profiles.

- We tested eight versions of the SFL, five that depend on just the total ISM content (defined as combined neutral and molecular component) and three that require the ISM be separated in to neutral and molecular phases. The latter three were tested with all three prescriptions of $R_{\rm mol}$ that we trialled. The linear molecular SFL, $\rm SFR_{H2}$ produces the best matches to the $\Sigma_{\rm SFR}$ profiles when used with the SR $R_{\rm mol}$ relation, with the models typically agreeing with the observed profiles to within a factor of 2. The two-component SFL $\rm SFR_{KMT}$,

combined with the SR relation does second best with agreement to typically a factor of 2.2, while the orbital time SFL SFR_{Ω}, at third best in terms of ϵ_{SFR} value, is the best of the single component ISM SFLs with agreement to within a factor of 2.5 over the intermediate radii disk. Again, the best SFLs here are selected based on our model predicted Σ_g as well as Σ_{H_2}, not the observed gas surface mass densities. However, the results are consistent with those from L08 and Tan (2010) who do use observed ISM profiles for their tests. This consistency also supports our CQ-disk model in an indirect way.

- The modelled star formation intensity profiles (Figs 2.6, 2.7, 2.8) match the observations best at intermediate radii, and show the largest deviations in the central region (where $R <= 0.3R_{25}$). This suggest that a more elaborate model is needed to explain the ISM and gas distribution in the centres of galaxies, especially those with bulges or a steeply rising rotation curve. However, integrating the SFR over the entire central region area we find that the models agree with the observations within a factor of 3 in all but one case. This indicates the systematic discrepancy integrated over galaxy centres generally is not severe.

Since we are testing a model for the distribution of star formation and gas in galaxies that we base on inferences from THINGS team results, there is no surprise that our model works well for large portions of galaxies selected from the THINGS sample. Our future papers will test our model on galaxies selected independently.

One advantage of our models is that they are easy to calculate given the rotation curve and the distribution of stellar mass. This may prove to be a useful advantage in terms of implementation compared to more detailed models like that of Ostriker et al. (2010). However to handle the central regions, some reasonable modifications may be required, such as requiring gas and SFR to only be at $r > 0.3r_{25}$ for galaxies with v_{flat} above some fiducial value.

Chapter 3

The Structure and Stellar Content of the Outer Disks of Galaxies: A New View from the Pan-STARRS1 Medium Deep Survey

3.1 abstract

The outer disks provide unique information about the formation history of disk galaxies. In this paper we present the results of an analysis of newly available Pan-STARRS1 Medium Deep Survey multi-band optical and near-IR ($g\,r\,i\,z\,y$) images of a sample of 700 low-redshift disk galaxies that spans broad ranges in stellar mass,

star-formation rate, and bulge/disk ratio. We combine these data with population synthesis SED fitting techniques to explore the radial distribution of the light, color, surface mass density, mass/light ratio, and age of the stellar population. We are able to characterize the structure and stellar content of the galaxy disks out to radii of about two times Petrosian r_{90}, beyond which halo light becomes significant. We measure normalized radial profiles for sub-samples of galaxies in three bins each of stellar mass and Concentration (a proxy for bulge/disk ratio). We also create and fit radial profiles for each of the 700 individual galaxies. We find that the majority of galaxies have down-bending radial surface brightness profiles in the bluer bands with a break radius of roughly r_{90}. However, they typically show single unbroken exponentials in the reddest bands and in the stellar surface mass density. We also find that the radial profiles of mass/light ratio and stellar age have a characteristic U-shape, declining with increasing radius in the inner disk (inside r_{90}) but increasing with increasing radius in the outer disk. We find a good correlation between the amplitude of the down-bend in the surface brightness profile and the rate of the increase in the M/L ratio in the outer disk. As we move from late- to early-type galaxies (e.g. increasing bulge/disk ratio), the amplitude of the down-bend and the radial gradient in M/L both decrease. We consider our results in the context of current models for the assembly of disk galaxies. We conclude that a combination of stellar radial migration that moves older stars outward, and a truncation/suppression of recent star formation in the outer disk is implied.

3.2 Introduction

The stellar disks of galaxies have been recognized as having exponential radial surface-brightness (SB) profiles since the seminal paper published by Freeman (1970). About a decade later van der Kruit (1979) studied several edge-on galaxies and found that the surface brightnesses of galactic disks do not decline exponentially forever, but can appear truncated after several radial scale-lengths. More recently, many studies using deeper modern imaging data (e.g. Pohlen et al., 2002; Erwin et al., 2005, 2008) showed that a variety of SB profiles exist. Notably, Pohlen & Trujillo (2006, PT06 hereafter) systematically studied 90 nearby late-type spiral galaxies using SDSS DR2 imaging data and found that there is no apparent truncation in the SB radial profiles of these face-on galaxies. Instead, they found the radial profiles can be divided into three categories: Type I, classical single exponential (10%); Type II, down-bending joint exponential (60%); and Type III, up-bending joint exponential (30%). [1] This disk profile classification scheme has been widely adopted by the community and a large number of models have been created to explain the formation of these different types of SB radial profiles:

Type I (single exponential, probably with an outer truncation) galaxies can be formed directly from the collapse of a uniformly rotating protogalactic cloud (Free-

[1] Truncations and Type II breaks are two fundamentally different phenomena. The former is called 'truncation' because its outer profile drops much faster than exponential but the outer part of the Type II disk can still be well described by an exponential function. The truncations are only seen in edge-on galaxies and the truncation radius is at about $4.5\,h$ while the down-bending profiles are seen in all inclinations and the break radii usually appear at $2.5\,h$, where h is the disk scale-length. (Martín-Navarro et al., 2014)

man , 1970; Fall & Efstathiou , 1980). Alternatively, they can also be formed through viscous redistribution (e.g. Ferguson & Clarke , 2001). van der Kruit (1987) argued that a uniformly rotating protogalactic cloud could collapse into an exponential disk with a sharp cut-off based on angular momentum conservation. The model naturally explains the exponential nature of galactic disks and suggests the cut-off radius, which is about $4.5\,h$, is related to the maximum angular momentum of the cloud.

This collapsing model is also one of the two traditional scenarios which attempts to explain the formation of Type II (down-bending) disk. However, as argued by Elmegreen & Hunter (2006), the collapsing model usually forms inner exponential disks with relatively sharp outer cutoffs. Also, the collapsing model would lead to a break radius at about $4.5\,h$ instead of the observed $2.5\,h$. Therefore, the other Type II disk formation scenario, which attributes the formation of breaks to a star formation threshold, was proposed (e.g. Kennicutt , 1989; Schaye , 2004; Elmegreen & Hunter , 2006). However, the star formation threshold scenario fails to produce a single exponential profile out to large radii (Schaye , 2004). Instead, secular evolution, especially the outward radial migration of stars is believed to have significant effects on the breaks (Debattista et al. , 2006; Roškar et al. , 2008). The interplay between a star formation cut-off and radial stellar migration produces stellar radial profiles in good agreement with observed Type II disks (Roškar et al. , 2008). Moreover, the predicted sharp change in the radial age profile is indirectly supported by the observational results of Bakos et al. (2008). We will show that this scenario is supported by the

observations we present here.

An explanation of the Type III (up-bending) disks is more difficult. One might consider that the Type III disk is formed by the enhanced star formation seen in galaxies with extended ultraviolet disk components (XUV disk, Thilker et al. , 2007). However, there is no obvious correlation between these two kinds of objects (Thilker et al. , 2007). Radial stellar migration might play an important role in forming Type III disks (Younger et al. , 2007), however, it is crucial to include intermittent (e.g. minor mergers, Younger et al. , 2007) or persistent (e.g. constant gas accretion, Minchev et al. , 2012) interaction with the intergalactic/circumgalactic environment. A more recent study by Bakos & Trujillo (2012) using much deeper images from the SDSS Stripe82 on 7 nearby galaxies show that the profiles of previously identified as Type III are actually contaminated by the stellar halo and they claim that there are no true Type III disks.

The three types of disks are not only different in their SB profiles but also look distinct in their radial color profiles. Bakos et al. (2008) studied radial $g-r$ color profiles of the 90 PT06 sample galaxies and found that: The $g-r$ color profiles of Type II galaxies typically show a 'U'-shape with a minimum at the break radius and a minimum color of $g-r=0.47\pm0.02$. The $g-r$ color profiles of Type I galaxies are almost flat in the outer disk and the average color profile has a relative constant value of $g-r=0.46$. The color profiles of Type III galaxies drop steeply within the break radius and then rise to form a plateau around the break radius with a color

of $g - r = 0.57 \pm 0.02$. The 'U' shape color profile of Type II galaxy implies a 'U' shape age profile, which is a signature of the stellar radial migration effect shown by Roškar et al. (2008). These different behaviors of color profiles provide us more information about the formation history of the outer disk. However, the Bakos et al. (2008) sample of Type I (9 galaxies) and Type III (21 galaxies) is too small to yield fully robust results and the radial color profiles alone are not easy to compare with theoretical models or numerical simulations.

It is important to note that the models are mostly focused on calculating the radial stellar *mass* distribution, however, the previous studies generally only present the distribution of the *light* in a single band. The light profiles trace a combination of stellar mass and age, with the relative importance of these two factors depending upon the pass-band of the observations. By observing in multiple bands these two effects can be disentangled, allowing the determination of the radial distribution of both the stellar mass and the characteristics of the stellar population. More specifically, the observed spectral energy distribution of the galaxy light can be used to estimate the mass-to-light ratio profiles to first order. This technique, based on the the mass-to-light ratio prescription of Bell et al. (2003), was used by Bakos et al. (2008) to derive stellar mass profiles for the PT06 sample. The increase in the $g - r$ color profiles galaxies in the outer disk of Type II and Type III galaxies implies that the mass-to-light ratio also rises in the outer disk. They also showed that the breaks in the Type II SB profiles almost disappear in the stellar surface mass profiles. The color profiles

of the 7 galaxies studied by Bakos & Trujillo (2012) also show a 'U'- shape with a slightly increasing value at large radii. Similar results were also obtained using deep stacked SDSS images for late-type galaxies (D'Souza et al. , 2014).

The recent studies above suggest that there might be multiple formation mechanisms for the observed outer stellar disks. Building a more comprehensive galaxy sample was therefore a primary motivation for our study. Motivated by these considerations, we have undertaken an investigation that improves upon these earlier studies in several ways. First, we use a more sophisticated and robust method to derive the stellar mass-to-light and mass profiles by employing multi-band SED fitting (thereby jointly interpreting all the multi-band imaging data rather than just a single color). Second, we will use data that enable us to investigate the faint outer disks in a much large sample of galaxies than in previous studies. Third, our sample is more representative of the full population of disk galaxies than the PT06 sample: our sample is much larger and we have broader ranges in stellar mass and surface mass density.

In this paper, we report the results from our analysis of the images of about 700 galaxies in the Medium Deep Survey (MDS) fields of the Pan-STARRS1 (PS1) project. We measure five-band (*grizy*) SB profiles and analyze them with the SED fitting program MAGPHYS to derive radial profiles of various parameters, such as stellar mass-to-light ratio, mass surface density, age, and specific star formation rate. In section 3.3 we describe the PS1MD data and our sample selection; in section 3.4 we

describe the data processing pipeline and briefly introduce the MAGPHYS software. We then present the results in three tiers. In section 3.5 we show the stacked images of the whole sample and some sub-samples to give an overview of the whole sample in 2D. We use these data to define the radial range of the disk region we are working on. In section 3.6 we present the composite radial profiles to show the 1D structures of generic disk galaxies. In section 3.7 we present a detailed analysis of radial profiles of all the individual galaxies. In particular, we analyze the breaks of SB profiles and compare our results with the PT06 SB profile classification scheme. We finally discuss our results in section 3.8 and summarize the major conclusions in section 3.9 The images and radial profiles of each individual galaxy are in the appendix and can be downloaded online. The cosmological parameters we adopt are $h = 0.7$, $\Omega_m = 0.3$, and $\Omega_\Lambda = 0.7$.

3.3 Description of Pan-STARRS1 data and sample selection

The imaging data is taken from the Medium Deep Survey (MDS) of the Pan-STARRS1 (PS1) telescope and camera. The PS1 is the prototype telescope of the Panoramic Survey Telescope & Rapid Response System (Pan-STARRS; Kaiser et al. , 2002), located on Mount Haleakala, Hawaii. There are 10 MDS fields, each with 7 square degrees field of view, observed in 5 wide bands (g,r,i,z,y; Tonry et al. , 2012).

We use the reference stack images, which have typical exposure times of ~ 10 ks in the g and r bands and ~ 20 ks in the i,z and y bands. There are also deep stack images, which have typical exposure times ~ 40 ks in the g, r, and y bands and ~ 80 ks in the i and z bands. These are only available in two of the MDS fields (MD04 and MD09). We use the reference stacks in this work to retain approximate exposure consistency between MDS fields. Further, as we demonstrate in Section 3.6, the reference stacks are already sufficiently deep to meet our goal of probing out to the disk/halo transition. Detailed descriptions of the PS1 MDS and the photometric calibration can be found in Tonry et al. (2012), Rest et al. (2013) and Schlafly et al. (2012).

The reference stack images can be used to measure SB profiles as faint as $\sim 28 - 30\, mag/arcsec^2$ in the r-band, much deeper than the SDSS images ($\sim 27\, mag/arcsec^2$, e.g. Bakos et al 2008.; PT06). For comparison, we show r-band images and SB radial profiles of an example galaxy from the PS1 MDS and SDSS DR9 mosaic images. in Fig. 3.1. The flux of the images are scaled to the average central bulge (within 4 pixel) flux. The pixel size of the PS1 image is 0.25"/pix and the typical FWHM of the PSF is about 1". The images of Fig. 3.1 are scaled to the same angular size. It is obvious that the PS1 MDS reference stack images are deeper than the SDSS images and the sky background rms of the PS1 image is lower than that of the SDSS image. Therefore the PS1 MDS images are much better for our outer disk study.

Our sample galaxies are selected from the SDSS-III database using the CASjobs

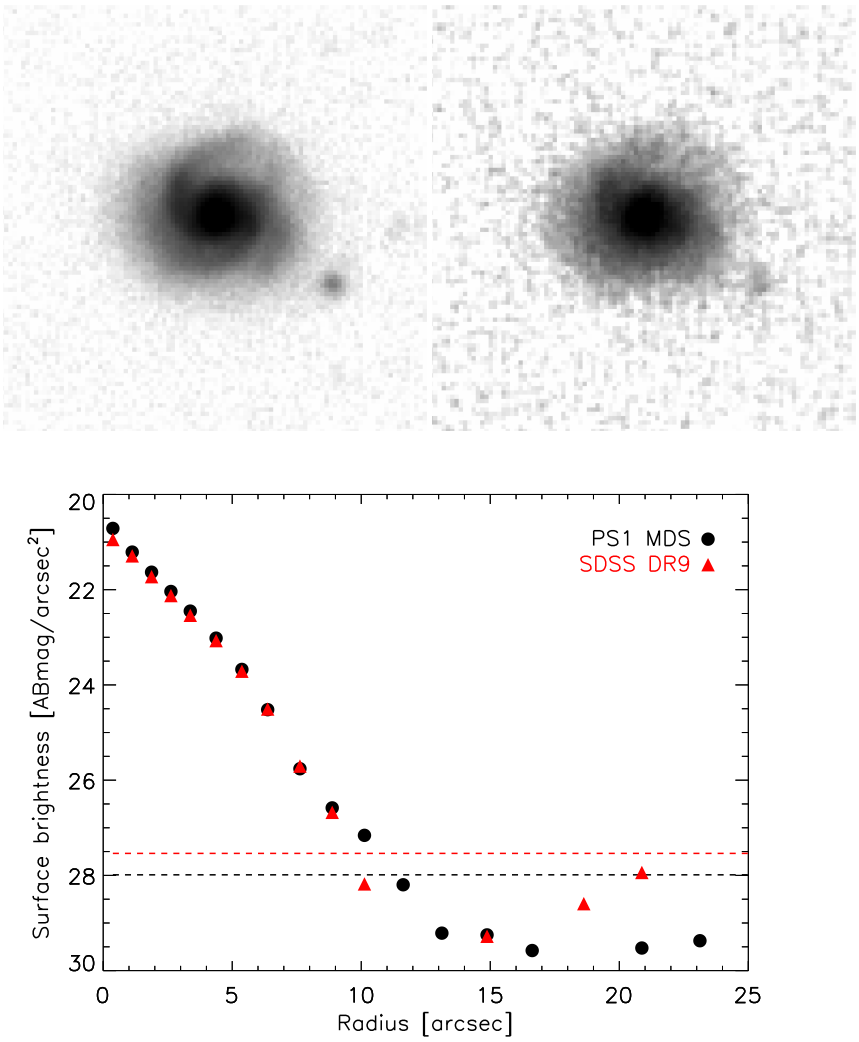

Figure 3.1: Comparison between PS1 MDS reference stack images and SDSS DR9 mosaic images. The upper panels are r-band PS1 image (left) and SDSS image (right). The images are background subtracted and the fluxes are scale to the central area (with radius of 4 pixel). The images are produced in ds9 using logarithmic scale. The lower panel is the r-band SB profiles produced using PS1 and SDSS data. The black dots and red triangles are measured SB using PS1 and SDSS data respectively. The black and red dash line show the sky rms of PS1 and SDSS images respectively. The PS1 image has a sharper PSF and lower sky rms than the SDSS image. The galaxy is centered at RA= 130.95206, DEC=43.800864 (Galaxy 6 in our sample, cf. Table 1). The field of view of the images above are 25" by 25". The equivalent exposure times are 10458s and 1294s for PS1 and SDSS images. Note the SDSS mosaic image is a stack image made through the SDSS DR9 image server using all exposures which has overlap with the target area and it has a much longer equivalent exposure time than single SDSS images.

interface[2]. The reason that we use this catalog is because SDSS has many complementary parameters such as redshifts, galaxy types, properties of neighboring galaxies, etc. There are 8 PS1 MDS fields (MD03 - MD10) observed by the SDSS. In order to choose disk galaxies, we require the fraction attributed to the r-band de Vaucouleurs component (fracDeV_r) in the SDSS composite model to be less than 0.7 [3] Similar to PT06, we also require the galaxies to be relatively face-on (expAB_r > 0.5, i.e. the ellipticity [4] is less than 0.5). In this work, we limit the galaxies by angular size instead of by apparent magnitude. The galaxies should be large enough to make it possible to measure well-resolved radial profiles (petroRad_r >= 5 arcsec). We also require that the galaxies have a measured spectroscopic redshift by selecting galaxies from the 'SpecObj' Casjobs catalog only. The resulting total number of galaxies using these selection criteria is 782. The final sample has 700 galaxies after taking out galaxies with an incomplete set of multi-band images. Since the mother sample of our galaxy sample, the SDSS spectroscopic galaxy sample, is highly complete (Strauss , 2002), we expect that our sample also has a high completeness. The only source of incompleteness is the size cut, which excludes physically small and distant galaxies.

Following Kauffmann et al. (2003b) and Schiminovich et al. (2007), Fig. 3.2 shows the distribution of our sample using two plots. The first one is the 'effective' stellar

[2]http://skyserver.sdss3.org/casjobs/

[3]The galaxy is modeled using a deVaucouleurs profile plus an exponential disk profile. A pure elliptical galaxy should have fracDev=1 and a bulge-less pure exponential disk should have fracDev=0. According to Masters et al. (2010), a galaxy with fracDeV = 0.7 corresponds to a Hubble type of Sa. or the galaxy zoo fraction of vote for disk galaxy (p_cs) to be greater than 50%.

[4]$The ellipticity is define as e = 1 - b/a$, where a and b are major and minor semi-axes of the ellipse respectively

mass surface density, μ_s, versus stellar mass, M_*. The value for μ_s is defined as

$$\mu_s = \frac{M_*}{2\pi r_{50,z}^2}, \tag{3.1}$$

where the $r_{50,z}$ is the Petrosian half-light radius in the z band. The other plot is specific star formation rate, SFR/M$_*$, versus M_*. Values for M_* and SFR are taken from the MPA-JHU SDSS DR7 release [5]. The value for $r_{50,z}$ is taken from the SDSS DR8 database. It is obvious that our sample is representative of the population of disk galaxies in SDSS over ranges of more than two orders-of-magnitude in stellar mass, mass density, and specific SFR. Our selection of disk dominated galaxies means we have only a sparse sampling of galaxies on the red sequence (sSFR $< 10^{-11} yr^{-1}$ - which are predominantly bulge-dominated galaxies).

The distributions of redshift, total stellar mass, r-band r_{90}, concentration parameter ($C = r_{90}/r_{50}$) and characteristic ellipticity of our sample galaxies are shown in Fig. 3.3. The r-band r_{90} (hereafter r_{90}) and r-band r_{50} are scale-lengths defined as the radius containing 90% and 50% of the Petrosian flux in the r-band respectively. For our sample galaxies, the r_{90} is roughly $0.7\,R_{25}$, which we define as the radius of the galaxy to the 25th ABmagnitude isophote in the r-band. The parameter C is correlated with galaxy bulge/disk ratio (Gadotti 2009; Lackner & Gunn 2012), with the range between log $C = 0.25$ and 0.45 corresponding roughly to bulge/disk ratios of ~ 0 and 1 respectively. Thus, C can serve as a proxy for Hubble types with smaller C indicating later type disks and larger C indicating earlier type disks.

[5] http://home.strw.leidenuniv.nl/~jarle/SDSS/

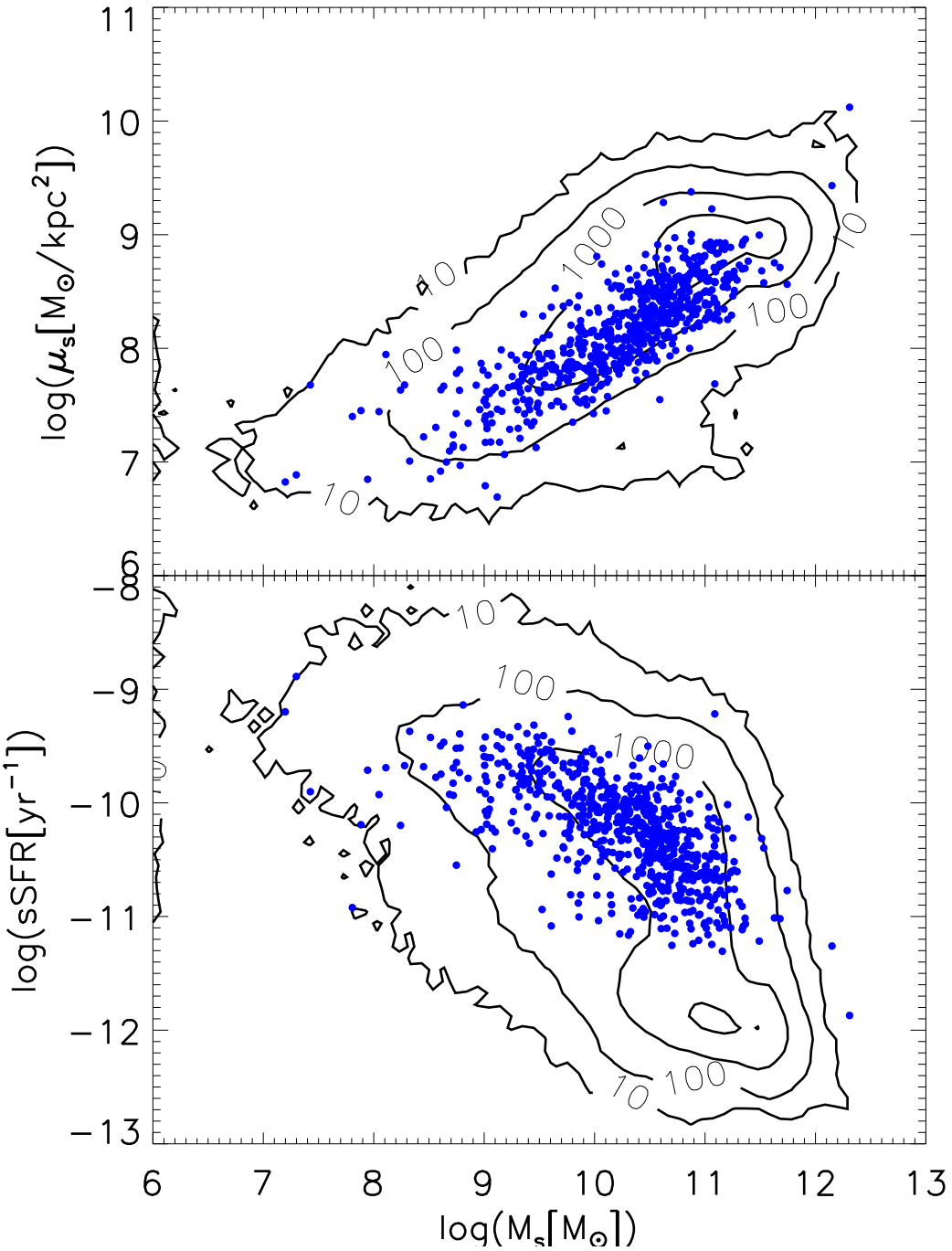

Figure 3.2: Global properties of our galaxy sample in comparison to SDSS overall. Upper: Stellar surface mass density versus stellar mass. Lower: specific star formation rate versus stellar mass. Blue dots are our sample galaxies and the background contours show the distribution of the entire MPA-JHU SDSS DR7 sample. Values of the blue points are calculated using PS1 photometry as described in this paper.

Since galaxies with different mass can have systematically different Hubble types (concentrations), assembly histories, companion galaxies, halo properties etc. (Kauffmann et al. , 2003b), we divided our sample into three subcategories by stellar mass: high mass ($M > 10^{10.5} M_{\odot}$), intermediate mass ($10^{10.5} M_{\odot} > M > 10^{10.0} M_{\odot}$), and low mass ($M < 10^{10.0} M_{\odot}$) galaxies. We have also divided our sample into three bins in concentration: $C > 2.4$, $2.4 > C > 2.1$, and $C < 2.1$. These bins roughly correspond to bulge/disk ratios of $B/D > 0.2$, $0.2 > B/D > 0.1$, and $B/D < 0.1$ (Gadotti 2009; Lackner & Gunn 2012).

We list our sample galaxies in the appendix. A part of the galaxy list is also listed below in Table 3.1.

3.4 Method

3.4.1 Data processing and radial profile extraction

We create 8' by 8' (1920pix by 1920pix) image cutouts for each galaxy. All the images are background subtracted stacked images. The background level was determined by the PS1 Image Processing Pipeline (IPP) using blocks of 400 by 400 pixels (100" by 100"). Since most of our galaxies are smaller than this block size the background subtraction performed by IPP should be appropriate and not cause over-subtraction of low spatial frequency emission. However, in order to study the outer disk more accurately, we need to do our own custom background subtraction. Here

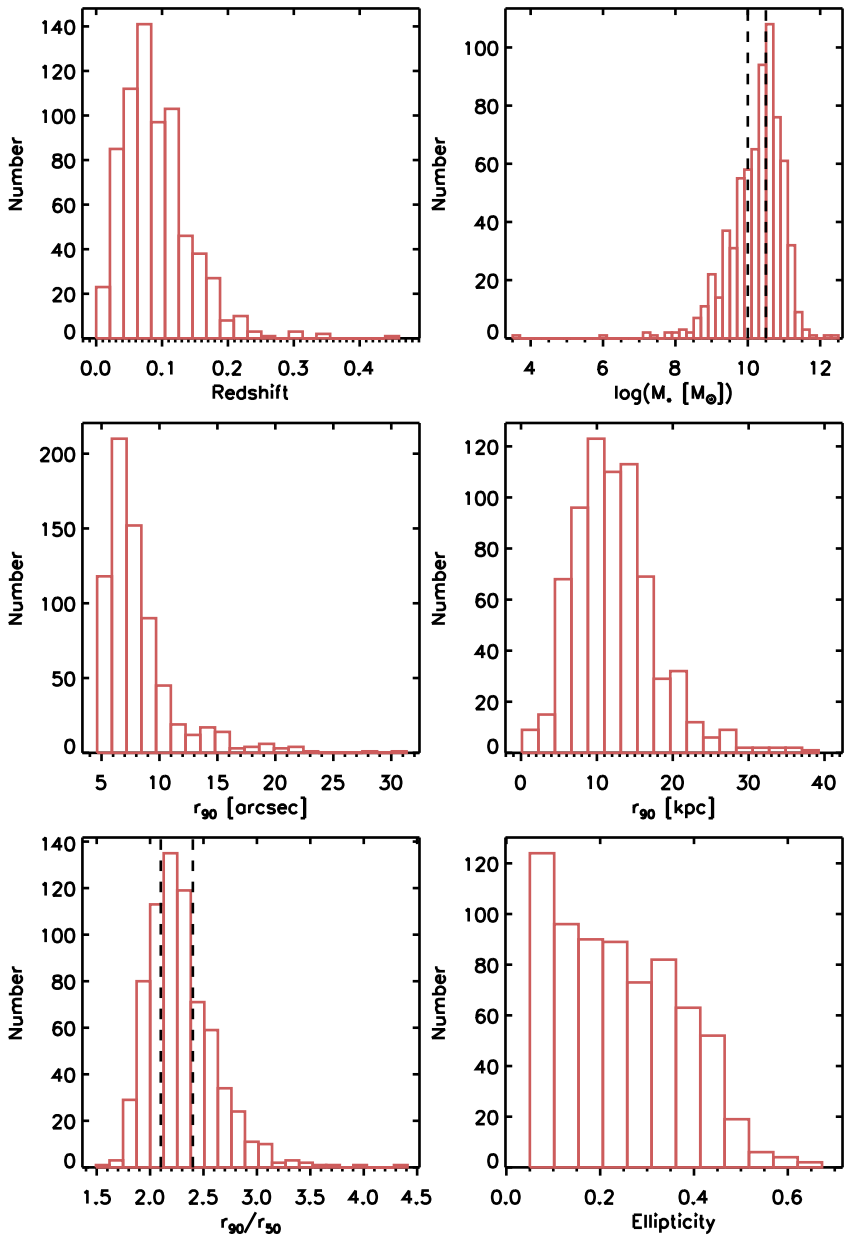

Figure 3.3: Histograms of redshift (upper left), total stellar masses (upper right), r-band r_{90} in arcsec (middle left) and in kpc (middle right), concentration parameter (lower left) and characteristic ellipticity (lower right) of our sample galaxies. The vertical black dash lines indicate the three mass bins (upper right panel) and three concentration bins (lower left panel) we used in this paper.

Table 3.1: Galaxy list example

ID	Field ID	RA	DEC	z	r_{90}	r_{50}	r_b	e	PA	lg(M_*)	lg(μ_s)	lg(sSFR)	k_{r1}	k_{r2}	k_{m1}	k_{m2}	$k_{\Upsilon_r 1}$	$k_{\Upsilon_r 2}$
					["]	["]	["]		[Deg]	[$M_\odot$]	[$\frac{M_\odot}{kpc^2}$]	[yr^{-1}]	[mag/r_{90}]		[$lg(\mu)/r_{90}$]		[$lg(\Upsilon_r)/r_{90}$]	
1	MD03	129.289	44.3036	0.13	4.86	2.33	4.75	0.05	54.67	10.62	8.46	-10.65	3.36	4.28	-1.19	-1.54	0.13	-0.14
2	MD03	130.200	44.2520	0.08	5.13	2.41	4.75	0.29	35.60	10.01	8.05	-10.24	2.53	4.38	-1.05	-1.47	0.01	0.13
3	MD03	131.078	45.0381	0.15	5.16	2.27	4.25	0.24	87.32	10.91	8.80	-10.69	2.81	4.07	-1.37	-1.17	-0.36	0.25
4	MD03	130.901	44.0561	0.11	5.11	2.69	3.81	0.09	11.90	10.35	8.12	-10.11	2.87	4.35	-1.46	-1.47	-0.26	0.25
5	MD03	131.361	44.9439	0.15	6.71	2.61	4.44	0.12	45.08	11.41	9.00	-11.13	2.40	4.67	-1.46	-1.25	-0.24	-0.34
6	MD03	130.952	43.8009	0.19	5.34	2.58	5.00	0.17	89.11	10.82	8.30	-10.15	2.94	4.59	-1.66	-1.85	-0.52	0.09
7	MD03	131.782	43.6363	0.09	5.38	2.77	3.81	0.21	-69.10	10.03	7.99	-10.01	2.33	4.30	-1.10	-1.64	-0.27	0.41
8	MD03	130.372	43.2660	0.18	5.00	2.53	3.19	0.05	44.16	10.66	8.26	-9.69	3.15	3.84	-1.78	-1.73	-0.81	0.18
9	MD03	129.000	44.2391	0.31	5.41	2.51	3.81	0.10	51.99	11.55	8.72	-10.34	2.24	4.48	-1.48	-1.21	-0.60	0.74
11	MD03	129.123	44.1469	0.13	5.81	2.61	3.81	0.09	-26.80	10.65	8.47	-10.19	2.51	4.25	-1.66	-1.08	-0.45	-0.15
12	MD03	131.171	44.3604	0.09	5.50	2.34	5.00	0.29	25.94	10.67	8.69	-10.13	3.16	3.95	-1.57	-1.16	-0.34	0.30
13	MD03	130.159	44.1456	0.08	5.73	2.50	3.81	0.05	-23.75	10.28	8.33	-10.51	4.49	3.51	-1.50	-1.84	-0.34	0.27
14	MD03	131.413	45.0530	0.14	5.73	2.68	3.81	0.32	-3.15	10.85	8.35	-10.93	2.10	3.20	-1.43	-1.70	-0.55	-0.14
15	MD03	130.280	44.0019	0.09	5.71	3.00	3.81	0.22	-45.43	10.00	7.77	-10.17	2.48	3.86	-1.54	-2.30	-0.42	-0.49
16	MD03	131.864	44.2269	0.11	5.70	2.96	5.75	0.13	48.53	10.18	7.99	-9.97	2.43	5.74	-1.26	-2.15	-0.23	0.17

Note – Galaxy list example. This table contains basic parameters of 15 galaxies selected from our 700-galaxy sample. The complete table of the whole sample can be downloaded online in electronic form. The RA, DEC and redshift (z) are from SDSS DR8 catalog. The r_{90}, r_{50}, break radius r_b, e, position angle (PA), M_*, μ_s (defined in Eq. 3.1), inner and outer r-band SB profile slope (k_{r1} and k_{r2}), stellar mass surface density profile slope (k_{m1} and k_{m2}), r-band mass-to-light ratio profile slope ($k_{\Upsilon_r 1}$ and $k_{\Upsilon_r 2}$) and sSFR are measured using PS1 data. The definition of the slopes can be found in Section 3.7.

we describe the pipeline used to mask out all the background/foreground galaxies and stars, derive galactic geometric parameters, subtract the background and extract multi-band radial profiles. All the data are processed in IRAF and IDL.

Since we have a fairly large sample of galaxies, it would be a very tedious job to mask all the contaminating sources by hand. Therefore we developed a semi-automatic graphic user interface (GUI) software to mask the contaminants such as foreground stars and background galaxies. First, we extract all the sources by using SExtractor applied to a 5-band composite chi-square detection image (Szalay et al. , 1999). All sources above 2σ local background variation are detected by SExtractor. We then examine the 3-color image and the mask segments on top of the 3-color image and select the mask segments which correspond to the target galaxy by clicking the mouse. We can also mask out SExtractor undetected stars and unwanted regions using circular apertures defined within this GUI software. The masks are then grown using the IDL function DILATE with a square shape operator. The size of the operator matrix is proportional to the size of the mask and has a minimum value of 5 pixel by 5 pixel.

The characteristic center, position angle (PA) and ellipticity of each galaxy are derived using the IRAF [6] task *ellipse* mainly following the two-step procedure provided by Li et al. (2011). In the first step, we fit all three parameters (center, PA

[6]IRAF is the Image Reduction and Analysis Facility, a general purpose software system for the reduction and analysis of astronomical data. IRAF is distributed by the National Optical Astronomy Observatory, which is operated by the Association of Universities for Research in Astronomy, Inc., under cooperative agreement with the National Science Foundation.

and ellipticity) using the i-band image. We then have radial profiles of the center coordinates ($x_c(r)$ and $y_c(r)$), position angle (PA(r)) and ellipticity (e(r)) for each galaxy. The characteristic center is determined using the origin value corresponding to the annuli at $0.5\,R_{25}$

$$\begin{aligned} X_c &= x_c(r = 0.5\,R_{25}) \\ Y_c &= y_c(r = 0.5\,R_{25}). \end{aligned} \tag{3.2}$$

In the second step, we fix the center determined in the first step and re-fit the PA and ellipticity. The final PA and ellipticity are held constant using the value of the annuli at R_{25}. We then visually examine every ellipse fit and re-fit the bad ones by hand.

After deriving the characteristic center, PA and ellipticity of the galaxy, we extract the SB profile over the radial range from 5 pixels (1.25") up to 3 R_{25}. The SB profiles are extracted with the characteristic parameters fixed in rings with the widths of the rings increasing logarithmically (in log step of 0.03). The values of the unmasked pixels within each ring are averaged to get the mean flux of each ring. The radius assigned to each ring is the average value of the inner and outer boundaries of each ring along the major axis. At this point we have a SB radial profile including the sky background (after deriving all the mean fluxes of every ring).

The outer most ring (the region between $5\,r_{90}$ and $6\,r_{90}$) is used to derive the background. The outer most ring is divided azimuthally into 36 regions (10 degrees for each region). We calculate the mode of each region and then derive the background value by averaging all the 36 mode values. The standard deviation of the 36 values

is taken as 1σ of the sky background. We then subtract the background value from each ring to get the background subtracted SB radial profile in each band. The error source for the SB is the combination of the sky background rms and the Poisson noise of the annulus. We did not include the dispersion of pixel values inside the annulus in our S/N calculation because this may be exaggerated by the internal structures such as spiral arms and star-forming regions.

The 5-band background subtracted SB radial profiles are corrected for Galactic reddening using the Cardelli et al. (1989) extinction curve assuming foreground E(B-V) values based on the Schlegel et al. (1998) dust maps. The K-corrections [7] were derived using the K-corrections calculator developed by Chilingarian et al. (2010) and Chilingarian & Zolotukhin (2012).

3.4.2 Deriving the stellar mass: SED fitting

Previous studies that convert SB into mass surface density usually use a single mass-to-light ratio (e.g. Freeman , 1970) or simple empirical mass-to-light ratios (e.g. Bakos et al. , 2008). To improve on these simple methods, in this paper, we use the Multi-wavelength Analysis of Galaxy Physical Properties (MAGPHYS) program (da Cunha et al. , 2008; Bruzual & Charlot , 2003; Charlot & Fall , 2000) to interpret the 5-band SB radial profiles. To do this, we do SED fitting using PS1 *grizy* photometry for each annulus of each galaxy and combine the fitted results to get radial profiles

[7] Note the input SB profiles for MAGPHYS are not K-corrected. The K-corrected SB profiles are only used for color analysis.

of various physical parameters, such as the stellar mass, average age, recent star formation rate (averaged over the last 0.1 Gyr). MAGPHYS supplies a comprehensive library of model SEDs (based on Bruzual & Charlot (2003)) at the same redshift and in the same photometric bands as the observed galaxy including various star formation histories (generally declining smoothly with time but allowing for bursts at late epochs). The model SEDs are made using a wide range of plausible physical parameters. MAGPHYS then compares the observed SED with the model SEDs and builds a marginalized likelihood distribution for each physical parameter. As a result, our estimation of uncertainty for each inferred parameter implicitly includes a contribution from any model parameter degeneracies in addition to the limitations from the photometry. Nevertheless we took pains to reduce the impact of degeneracy as described below, for the specific case of extinction as a function of galactocentric radius.

The effects of dust reddening and age on the optical SED of galaxies conspire to produce a very similar relationship between color and stellar mass-to-light ratio (e.g. Bell & de Jong , 2001). This means that the optical SED can yield a robust measurement of the stellar mass-to-light ratio. However, if we wish to make inferences about the age of the stellar population we need some independent way to estimate the extinction. The optimal method would be to use high-resolution ($\sim$arcsec) ultraviolet and infrared images, which we do not have. Instead we use an extinction prior in our model fitting that is based on galaxies that are similar to those in our sample, but for

which the radial dust extinction has been independently measured. We show these priors in Fig. 3.4. They were calculated as follows. The extinction radial profile is assumed to decay from a central extinction value $\tau_{\rm V0}$ exponentially until reaches a lower limit $\tau_{\rm V,min}$. We set the scale length of the exponential part of the extinction profile for all galaxies to be $1r_{90}$ (Muñoz-Mateos et al. , 2009). The central extinction value varies from galaxy to galaxy depending on total stellar mass of the galaxy (Brinchmann et al. , 2004). We fit a Gaussian functional form to the observed $\tau_{\rm V0}$ of low-redshift star forming galaxies provided by Brinchmann et al. (2004) so that we can determine the $\tau_{\rm V0}$ for every galaxy as a function of its stellar mass. The extinction lower limit is set to be $\tau_{\rm V,min} = 0.4$ and it usually meets the exponential profile in the radial range $r/r_{90} = 1 - 2.5$. The Gaussian fitting to the $\tau_{\rm V0}$ and the assumed extinction profiles are shown in the upper panel of Fig. 3.4. The actual extinction prior is then set individually for each annulus to be between the 1/2 and 2 times of the parameterized typical extinction described above. This choice of $\tau_{\rm V}$ is justified by the MAGPHYS $\rm A_V$ output, which is also plotted in Fig. 3.4. The $\rm A_V$, which is the stellar extinction, is defined as

$$\rm A_V = 1.086 \mu \tau_V, \tag{3.3}$$

where μ is the fraction of τ_V contributed by dust in the diffuse ISM. The MAGPHYS output $A_{\rm V}$ for our sample is consistent with previous spectroscopic observations of similar galaxies (CALIFA group in private communication and Muñoz-Mateos et al. , 2009)

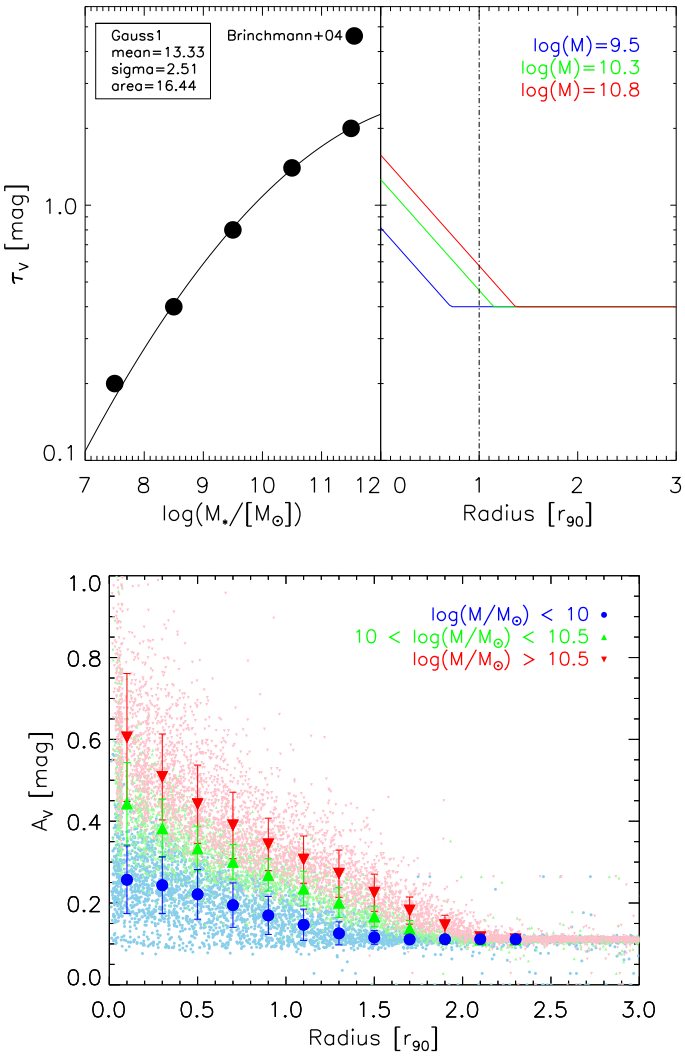

Figure 3.4: MAGPHYS extinction priors (upper panels) and output Av (lower panel). Upper-left: central total dust extinction of the *emission-line gas* in low-redshift star forming galaxies as a function of stellar mass. The black dots are scaled data from Brinchmann et al. (2004) and the solid line is the Gaussian functional fit to the data. Upper-right: parameterized typical radial variation in the emission-line extinction used for the MAGPHYS fitting; only three example galaxies are shown here: high mass (red), intermediate mass (green) and low mass (blue) galaxies; each parameterization starts with the corresponding central extinction from the left panel and decreases exponentially until hit the lower limit $\tau_V = 0.4$. To implement such an extinction prior, the fitted τ_V values are allowed to range from 0 to 2 times the radial extinction curves shown here. Lower panel: The MAGPHYS output A_V composite radial profile. This refers to the extinction affecting the *starlight*. The A_V output for the annuli of all the galaxies are plotted versus radius (normalized in r_{90}) The points are color coded in stellar mass as describe in the legend and in Section 3.3.

One example of MAGPHYS SED fitting and the distribution of different physical parameters is shown in Fig. 3.5. We take the 50% (median) value of the likelihood distribution to be the value of that physical parameter and take half of the difference between the 16th and 84th values to be the 1σ uncertainty.

The SED fitting using annular photometry may lead to biases in our results because each annulus unavoidably blends contributions from physically unassociated regions, which may have different star formation histories. For instance, arm and inter-arm locations are jointly measured within an annulus. The best way to derive the stellar mass radial profiles might be to use pixel SED fitting and then to sum up the parameter results. However, this method is much more computational intensive (cf. POGS project, Vinsen &Thilker 2013; Thilker et al. 2014 in prep) and difficult to apply to the low SB regime we are attempting to probe. Nevertheless, we may be somewhat insensitive to very low levels of star formation (such as seen in XUV-disks) if the optical luminosity is dominated by an older stellar population.

3.5 The 2D stack images

3.5.1 Motivation

The $g - r$ color profiles measured by Bakos et al. (2008) have revealed that the outer disk is different from the inner disk by having a redder color and (probably) an older age. The 'red' and 'old' descriptions also apply to stellar halo stars, which

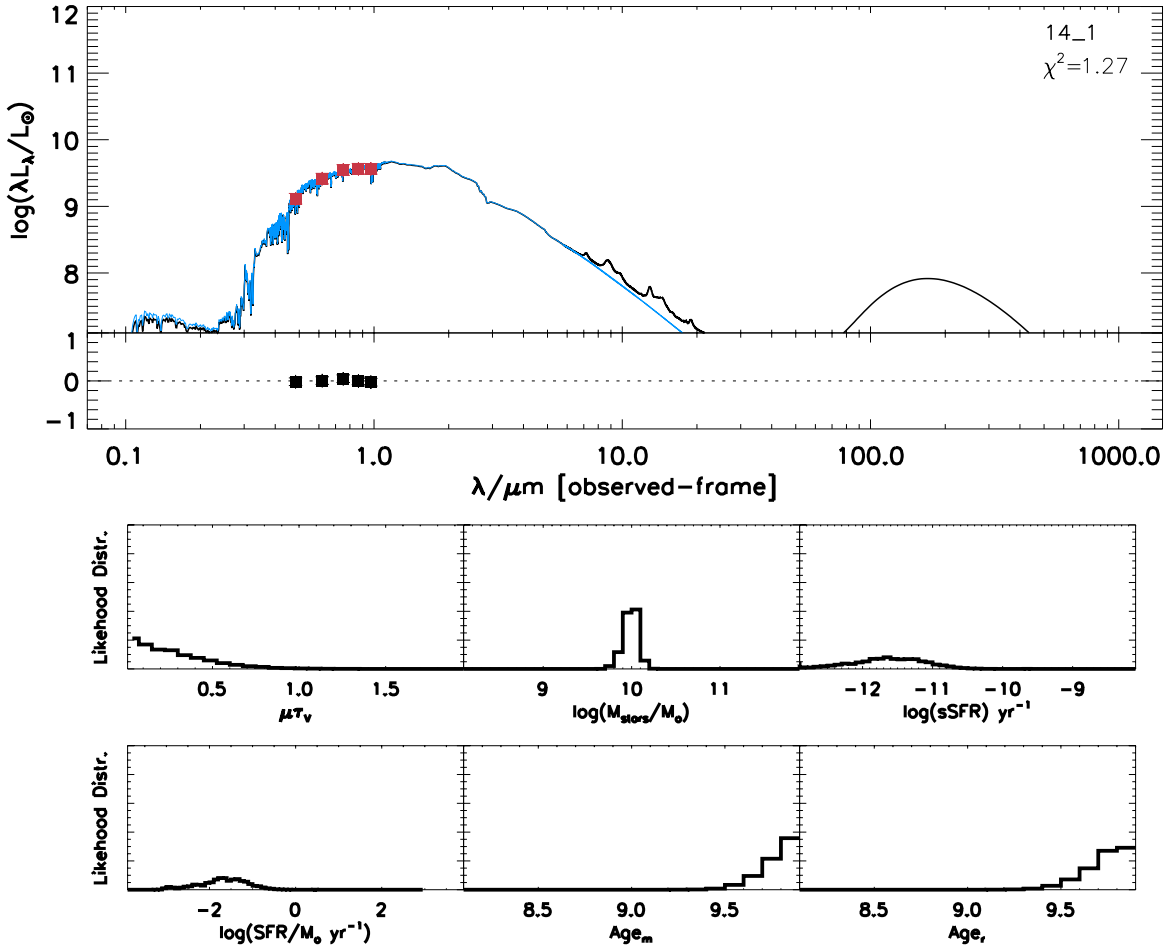

Figure 3.5: Example of MAGPHYS SED fitting and the distribution of different physical parameters. Upper panel: The red points are the observed 5-band photometry for one annulus of one of our galaxies. The black curve is the fitted attenuated SED and the blue curve is the fitted unattenuated SED. The black dots show the residuals. Lower panel: Marginalized likelihood distributions of various physical parameters: clockwise from upper left, these are the dust attenuation of the starlight, the stellar mass, the specific SFR, the log r-band-weighted mean age in years, the log of the mass-weighted mean age in years, and the SFR.

raises the possibility that we could be seeing the stellar halo instead of the outer disk. Bakos & Trujillo (2012) studied 7 of the PT06 galaxies using deep imaging data and claimed that up-bending disks were caused by the contamination of halo light in the outer disk. It is therefore interesting to investigate where the stellar halo starts to emerge in the outer region and make a clear definition of the outer border of the stellar disk region. Previous studies (Zibetti et al., 2004; D'Souza et al., 2014) show that the stellar halo usually has a much rounder shape than the stellar disk, so the best way to study the stellar halo is to look into the 2D stacked images.

Zibetti et al. (2004) stacked 1047 local ($z \sim 0.05$) edge-on disk galaxies imaged in five bands by SDSS. Zibetti et al. (2004) contract or expand each galaxy in such way that the selected scale-length of each galaxy has the same angular size. D'Souza et al. (2014) made stack images using a much larger sample, 45508 galaxies, and the sample contains both early type and late type galaxies. D'Souza et al. (2014) made a further step by rebinning each galaxy to produce an image scaled to the common value of redshift $z = 0.1$. They also divided their sample into different mass bins to study the properties of stellar halo as a function of stellar mass. However, they did not rescale the size of the galaxies as done by Zibetti et al. (2004). Assuming the exposure time for each SDSS image is about 100s, the total exposure times of the stack images made by Zibetti et al. (2004) and D'Souza et al. (2014) are about 100ks and 4.55Ms. Since typical exposure time of our PS1 MD images is about 10ks, the total exposure time of our sample is about 10Ms.

3.5.2 Stack method and the stack images

Here in this paper, we process and stack the galaxy images following a method combining the techniques provided by Zibetti et al. (2004) and D'Souza et al. (2014): Galaxy images and masks are shifted, rotated and contracted/expanded by the IRAF task GEOTRAN so that the transformed image is centered on the center of the galaxy, the major axis of the galaxy is horizontal and r_{90} is 7" (28 pixels). The GEOTRAN task was run without flux conservation so that the SB is preserved during the transformation. We then scale the linear SB I_ν to redshift $z = 0.1$ according to the equation

$$I_{\nu,z=0.1} = I_0(\frac{1+z}{1+0.1})^3, \tag{3.4}$$

where I_0 is the original intensity in unit of $\mathrm{erg\,s^{-1}cm^{-2}\,Hz^{-1}\,arcsec^{-2}}$ and z is the redshift of the galaxy. This equation corrects both the $(1+z)^4$ cosmological SB dimming and the $(1+z)^{-1}$ frequency compression effect on the monochromatic flux. The SB is then corrected for Milky Way extinction according to Schlegel et al. (1998). The K-correction is ignored. Note that D'Souza et al. (2014) did the stacking in a different way: they ran the IRAF GEOTRAN with flux-conservation so that the SB is not preserved. They also did not count for the $(1+z)^{-1}$ frequency compression effect.

We then apply the masks to each image and subtract the sky background calculated using the IDL routine MMM and combine the masked background subtracted images to make the stack image. For each pixel of the stack image, we only use

intensity values within the 16% and 84% percentiles of the pixel value distribution at that specific pixel. Following Zibetti et al. (2004) we made a mean stack image, a median stack image and a mode stack image. The mode stack image is calculated using the approximation (Zibetti et al. , 2004)

$$Mode = 3 \times Median - 2 \times Mean. \tag{3.5}$$

We also have the rising background problem in the outer regions of the mean and median stack images (Zibetti et al. , 2004). Therefore, we use the mode stack images, which are much less affected by this problem. Following D'Souza et al. (2014), we make stack images using sample galaxies divided in three different mass bins: high mass ($M_* > 10^{10.5} M_\odot$) galaxies, intermediate mass ($10^{10} M_\odot < M_* < 10^{10.5} M_\odot$) galaxies and low mass ($M_* < 10^{10} M_\odot$) galaxies respectively. We also make a super stack image using all the galaxies in our sample.

The stack images are shown in Fig. 3.6. We also plot isophote contours (green lines) and $2\,r_{90}$ (14", red circles) on top of the images. It is obvious that the emission of the stacked galaxy extends out of $2\,r_{90}$. Also, the isophotes inside the $2\,r_{90}$ all have similar ellipticity, while isophotes outside the $2\,r_{90}$ are significantly rounder than those inside $2\,r_{90}$. The extended PSF wing (up to $3\,r_{90}$) might cause some of the emission outside $2\,r_{90}$ but should have minimum effect on disk light within $2\,r_{90}$ (cf. appendix 3.8.1 for detailed discussion).

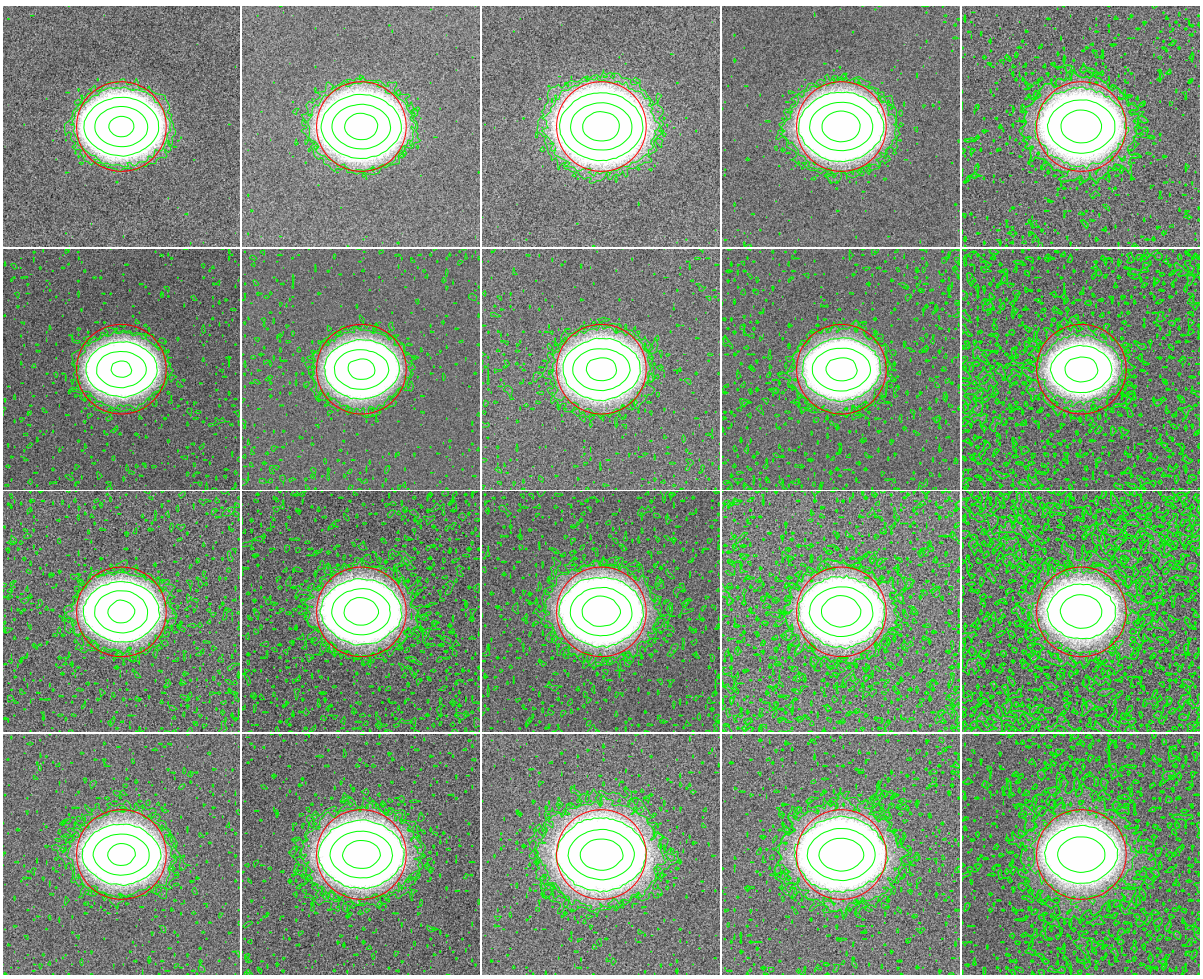

Figure 3.6: 2D stack images. From top to bottom: all galaxies, low-mass galaxies, intermediate-mass galaxies, high-mass galaxies. From left to right: g, r, i, z, y band. The contour levels represent 23, 25, 27, 29, 30 ABmag/arcsec^2. The red circles indicate $2\,r_{90}$. The 30 ABmag/arcsec^2 contour is close to $3\,r_{90}$.

3.5.3 Evidence of the stellar halo

We extracted 1D SB and color profiles of the stack images using the method described in section 3.4 and fit the SB profiles of the stack images using the MAGPHYS and the results are shown in Fig. 3.7 - Fig. 3.10. The stack images using galaxies in different mass bins have lower signal-to-noise ratio in the very outer region ($>\sim 3\,r_{90}$) and the figures from Fig. 3.8 - Fig.3.10 are plotted to show the variations of the profiles in different mass bins.

The stack image made using all the galaxies (Fig. 3.7) has the best SNR and we are confident about the profiles out to about $3\,r_{90}$. The main conclusion from this figure is that the stellar surface density profile shows an obvious change in slope (up-turn) beyond $2\,r_{90}$ and the color and mass-to-light ratio profiles show a relatively constant red color and high mass-to-light ratio. The colors in the region $2\,r_{90}$ and $3\,r_{90}$ are $g-r \approx 0.8$ and $r-i \approx 0.6$, which are very close to the values found by Zibetti et al. (2004). The stellar mass measured in the stellar halo of the all-galaxy stack image (within the region $2\,r_{90}$ and $4\,r_{90}$) is about $10^{8.4} M_{\odot}$ and is about 1% of the total stellar mass of the stack galaxy. We suggest that the upward break in the surface mass density profile at around $2, r_{90}$ represents the transition from the region dominated by the outer disk and that contaminated by the halo.

The behavior of the galaxy ellipticity as a function of radius provides additional clues, since the halo is intrinsically much rounder than the disk. In order to maximize this effect of the stellar halo on the geometry of the galaxy shape, we made a stack

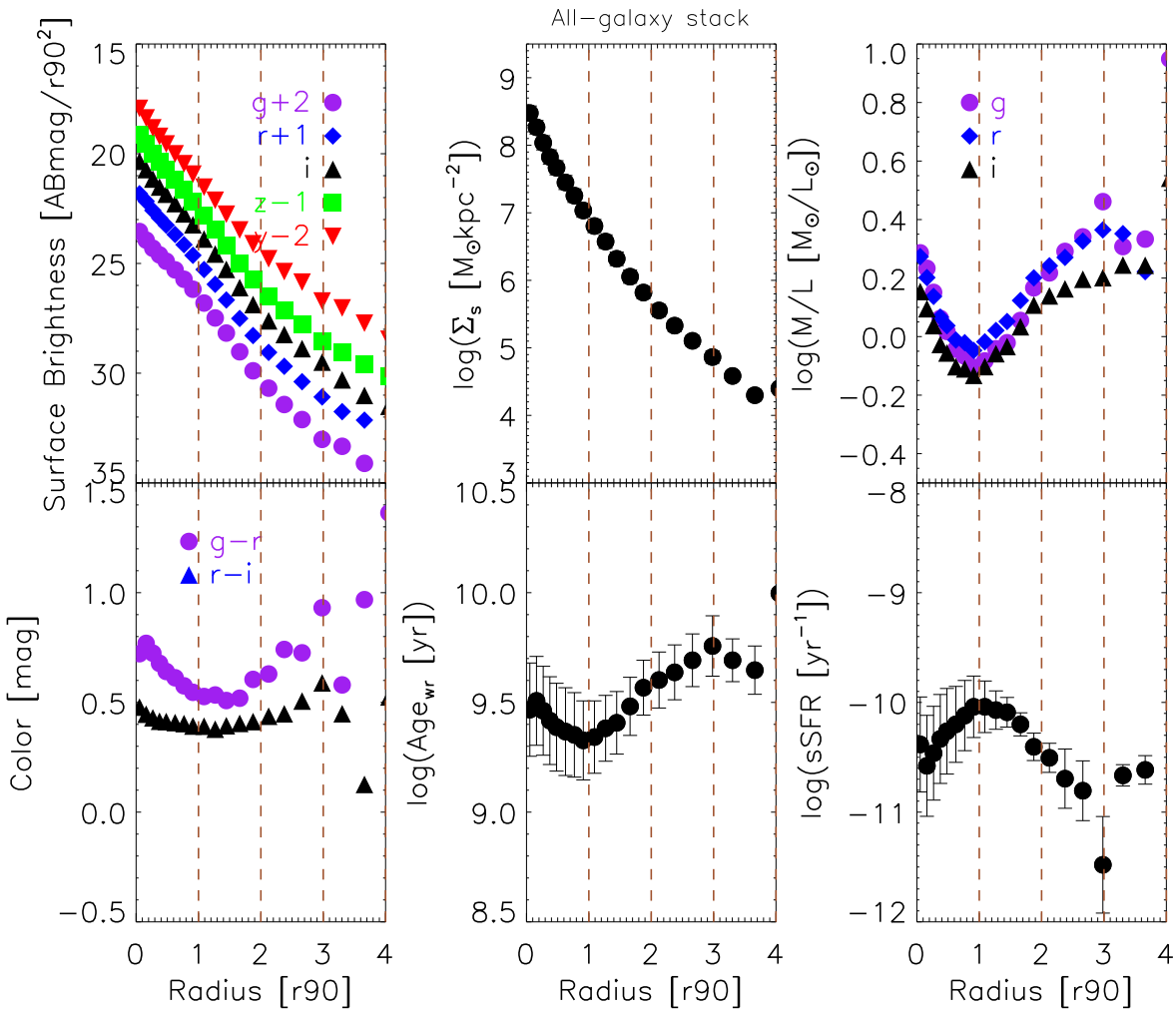

Figure 3.7: Radial profiles of stack image of all galaxies. Vertical dash lines show 1, 2, 3 times r_{90}. The profiles show (clockwise from the upper left) the multi-band surface brightness, the stellar surface mass density, the mass-to-light ratios in three bands, the specific SFR, the log of the r-band-weighted age, and the colors. The upturn/break in the stellar surface mass density profile at around $2, r_{90}$ and red colors beyond that radius suggest a transition from disk to halo at around this radius.

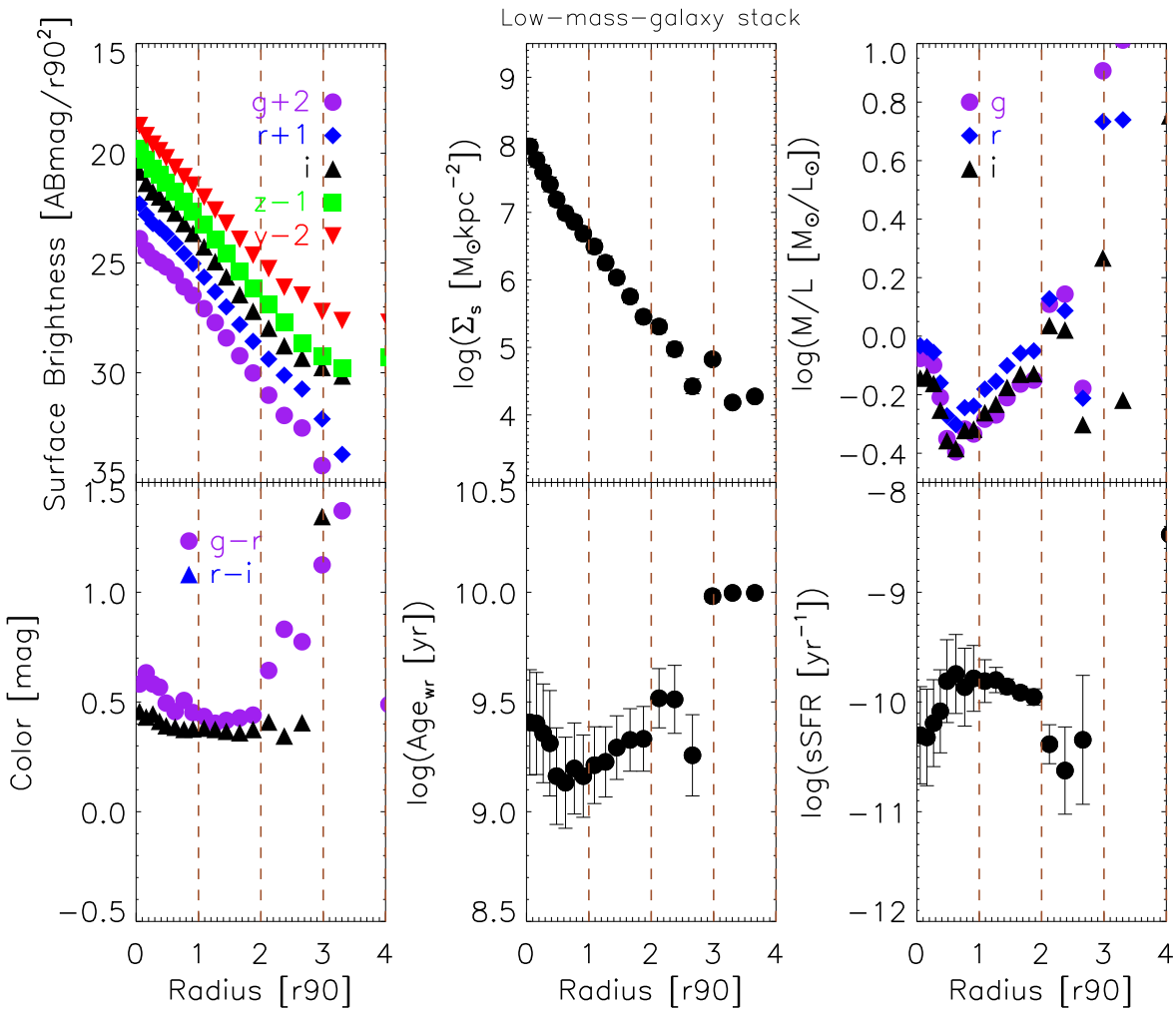

Figure 3.8: Radial profiles of stack image of low mass galaxies. The profiles inside $3\,r_{90}$ are robust, however, the results outside $3\,r_{90}$ are unreliable because the SB profiles are dominated by the sky background uncertainties in this regime.

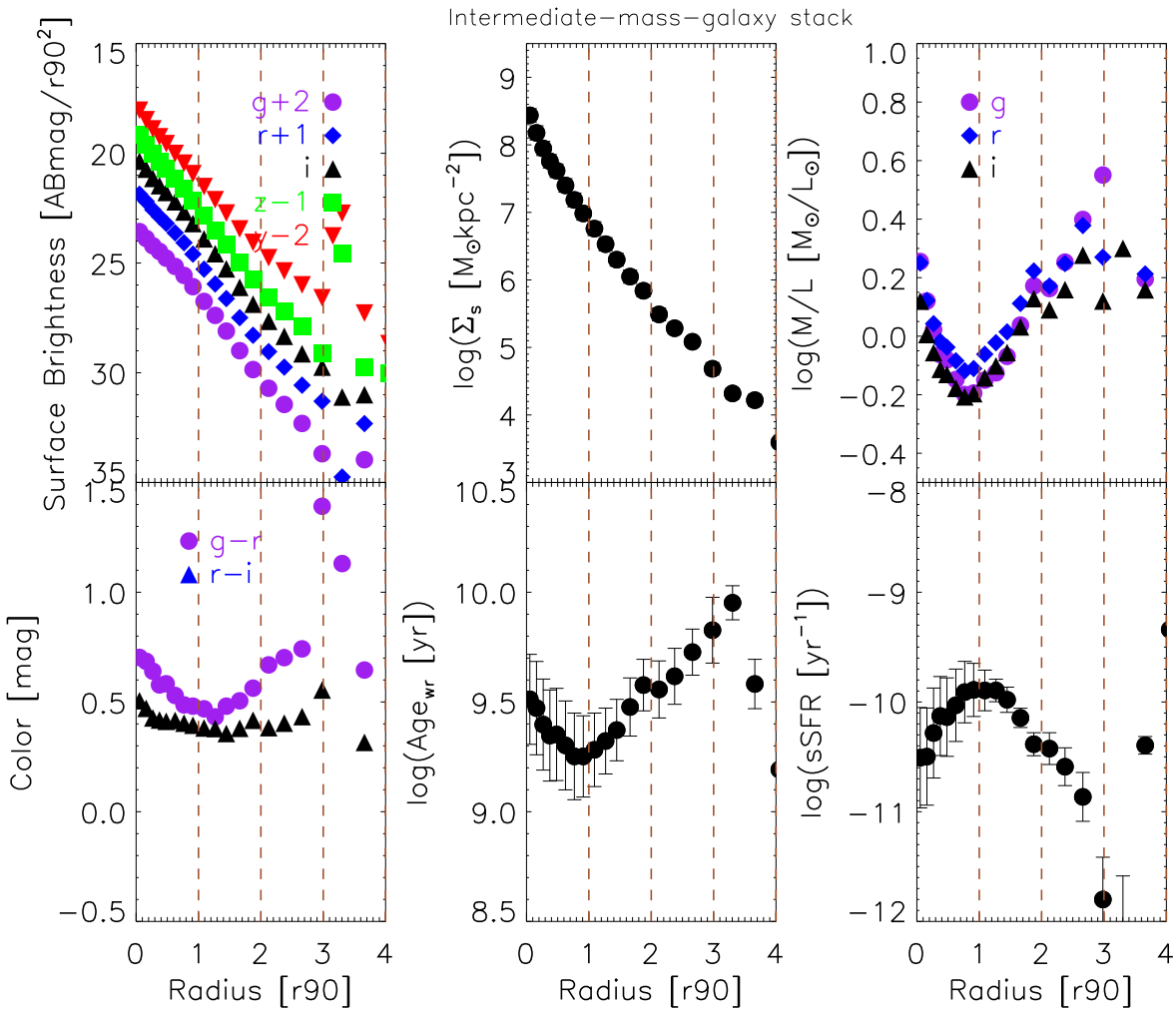

Figure 3.9: Radial profiles of stack image of intermediate mass galaxies. The profiles inside $3\,r_{90}$ are robust, however, the results outside $3\,r_{90}$ are unrelaible because the SB profiles are dominated by the sky background uncertainties in this regime.

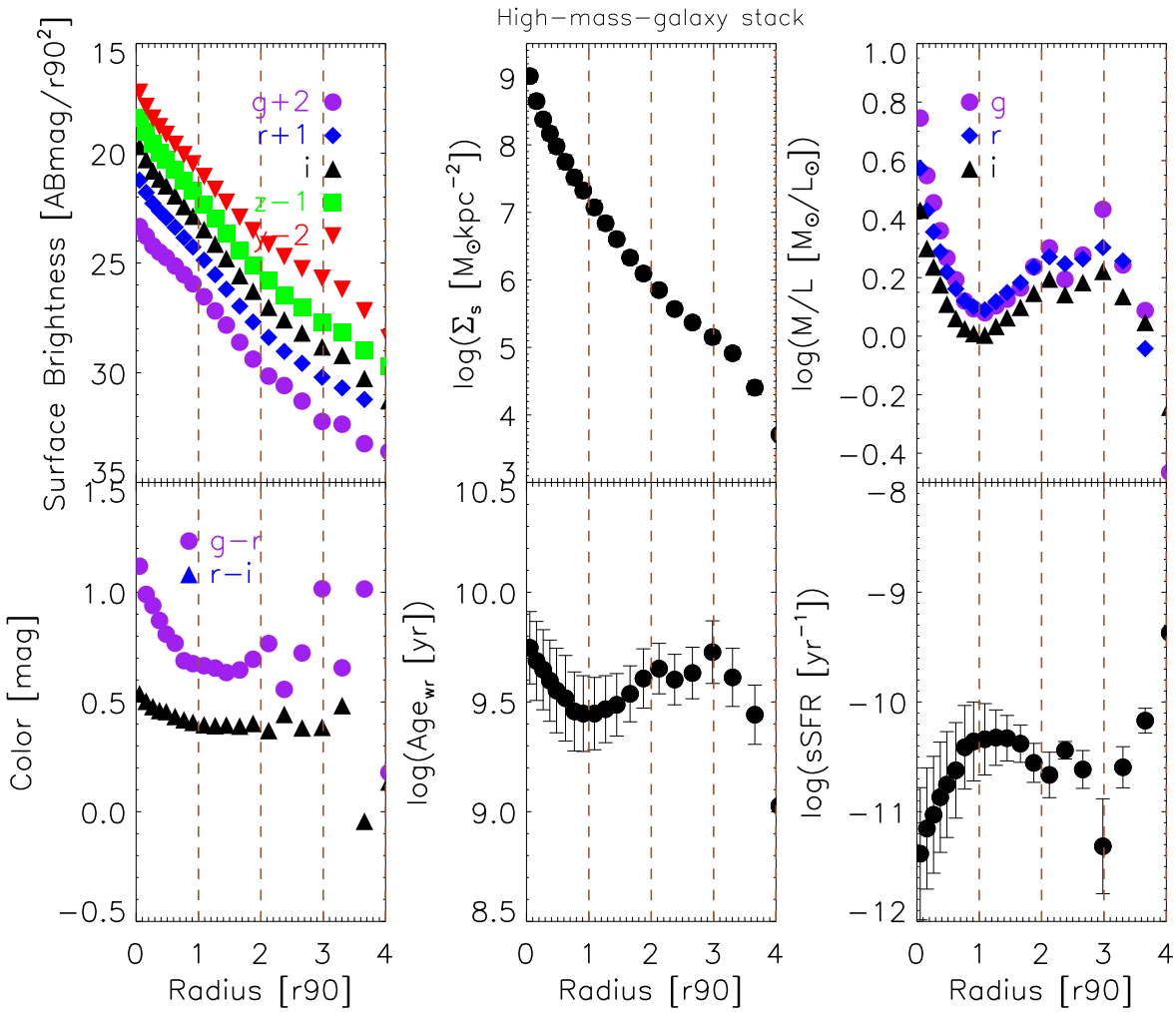

Figure 3.10: Radial profiles of stack image of high mass galaxies. The profiles inside $3\,r_{90}$ are robust, however, the results outside $3\,r_{90}$ are unreliable because the SB profiles are dominated by the sky background uncertainties in this regime.

image using galaxies with highest ellipticities, i.e. $e > 0.4$. The ellipticity profile of this high-ellipticity stack image is plotted in Fig. 3.11. The ellipticity profile rises slowly between $\sim$0.5 and $\sim$1.4 r_{90} and then slowly declines out to $\sim 3\,r90$.

Taken together, we conclude that the images of the outer disk are not significantly contaminated by light from the stellar halo at radii interior to $\sim 2\,r_{90}$.

3.6 Composite radial profiles: the generic shapes of 1D profiles

Perhaps the most compact way to visualize the general properties of the radial profiles of the 700 sample galaxies is to plot all the radial profiles onto a single figure with the radius normalized by the galaxy's intrinsic scale-length (r_{90}). We will do this by creating two sets of composite profiles: one in which the galaxies are binned in stellar mass and one in which they are binned in the concentration parameter ($C = r_{90}/r_{50}$).

We first divide our sample into three bins in stellar mass, and show the resulting composite SB radial profile plots and stellar surface mass radial profile plot in Fig. 3.12), and then present the corresponding $g-r$ and $g-i$ color radial profiles in Fig. 3.13. Lastly, we show the corresponding g-band stellar mass-to-light ratio plots in Fig. 3.14.

The resulting SB profiles have a dynamic range of about 7 magnitudes. The

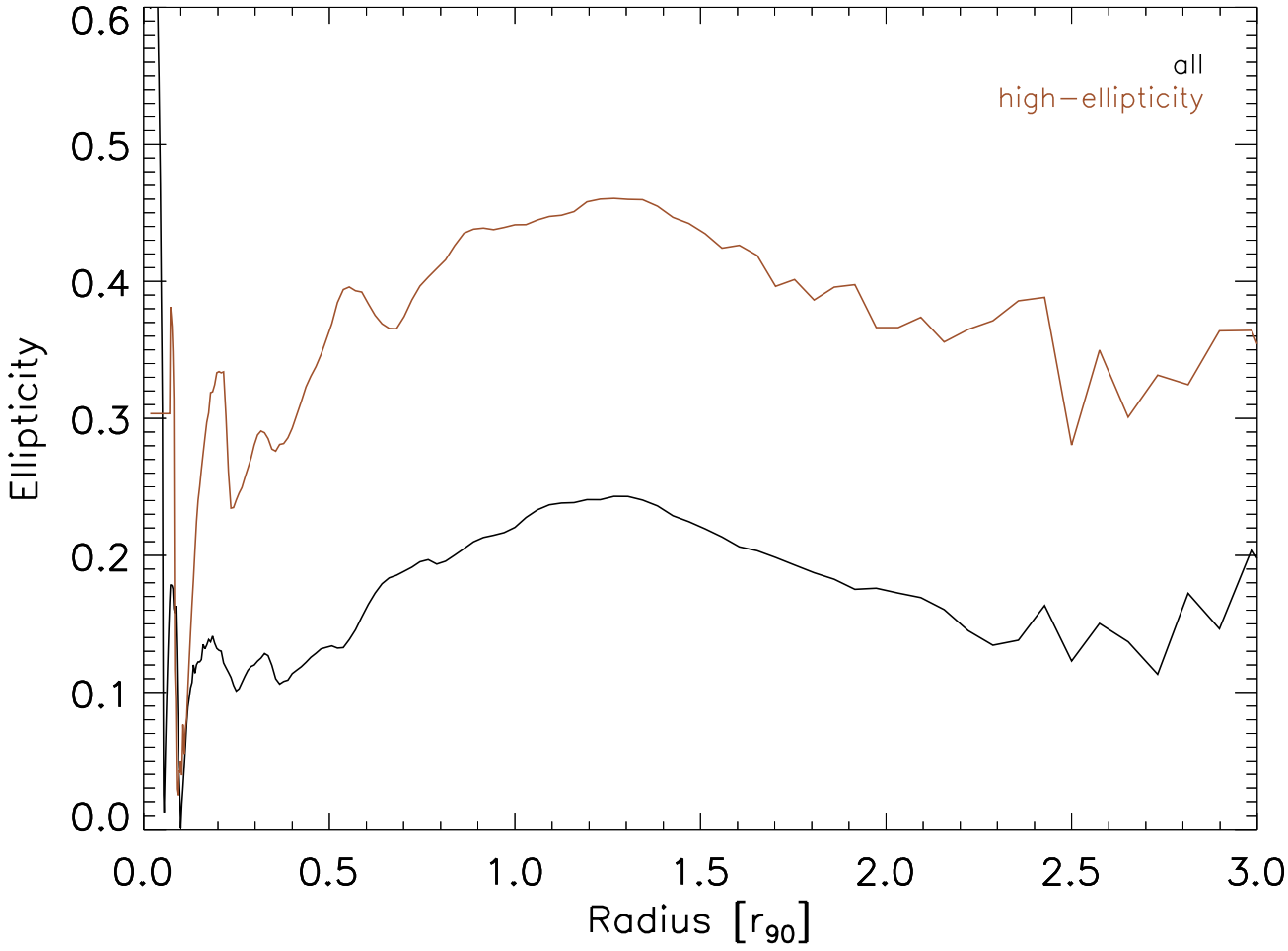

Figure 3.11: Ellipticity profiles of stacked i-band images of all galaxies and galaxies with ellipticity $e > 0.4$. The ellipticity remains high in the region between 1 and 2 r_{90} and we conclude the light in this region is dominated by the disk rather than the stellar halo.

composite i, z, y SB and the stellar mass surface density radial profiles are very close to pure exponentials with a scale-length $\sim 0.3\,r_{90}$. The plots in the bluer bands, especially the g-band SB radial profile, show a down-bending feature with a break radius at $\sim r_{90}$. This implies that most g-band profiles are down-bending and this is consistent with the PT06 results. There are no obvious breaks in the i, z, y and Σ_s radial profiles. This is consistent with the results in Bakos et al. (2008) and Bakos & Trujillo (2012).

The changes from g-band to the y-band and then to the Σ_s radial profiles imply that we have a positive color gradient and thus a increasing stellar mass-to-light ratio beyond $\sim 1r_{90}$. The color profiles (Fig. 3.13) do indeed show that the colors turn up at larger radii. The higher mass galaxies tend to be redder at all radii, but the shapes of the radial color profiles are the same in all three mass bins. Our sensitive PS1 imaging in the i, z, and y-bands provides improved contrast between the minimum in the color profiles (near r_{90}) and the comparatively red outermost disk.

Irrespective of whether the color gradients are driven purely by the age of the stellar population or whether dust reddening plays a role, the redder colors in the outer disk imply that that the stellar mass-to-light ratio is larger there. This is shown explicitly in the top panel of Fig. 3.14. The g-band stellar mass-to-light ratio at first decreases with increasing radius as we move outward from the center of the galaxies, reaches a minimum value, and then rises as we move into the outer disk. The normalized radius at which the minimum occurs in stellar mass-to-light ratio increases

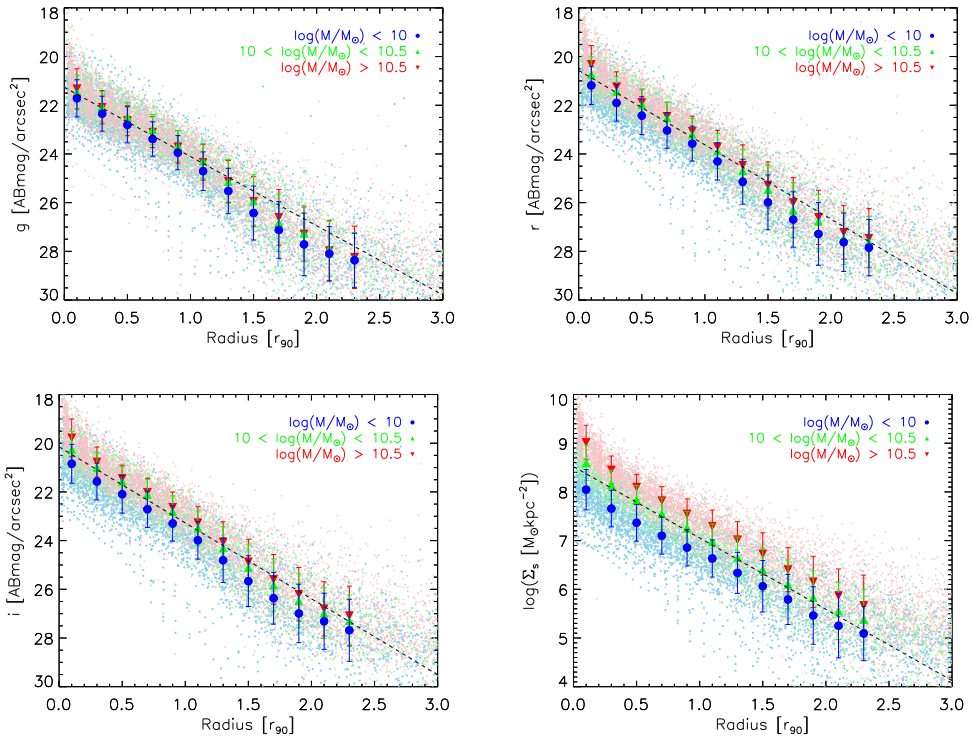

Figure 3.12: Composite radial profiles of g, r, i -band SB and stellar mass surface density. Each point corresponds to single annulus in a singe galaxy, and are color-coded according to galaxy mass, as indicated in the legend. The large symbols show the median value within bins of width 0.2 r_{90}. The vertical bars represent the dispersion in the observed/derived median values and not the typical error on each of the thousands of measurements. The photometric magnitudes are Milky Way extinction corrected and K-corrected. The dash line in each panel is a pure exponential fit to the data between 0.3 and 1 r_{90}. The bluer bands show down-bending radial profiles starting at about $1.0\,r_{90}$, while the redder bands and the surface mass density are single exponentials beyond the inner bulge-dominated region inside $\sim 0.3\,r_{90}$. This is true in all bins of stellar mass.

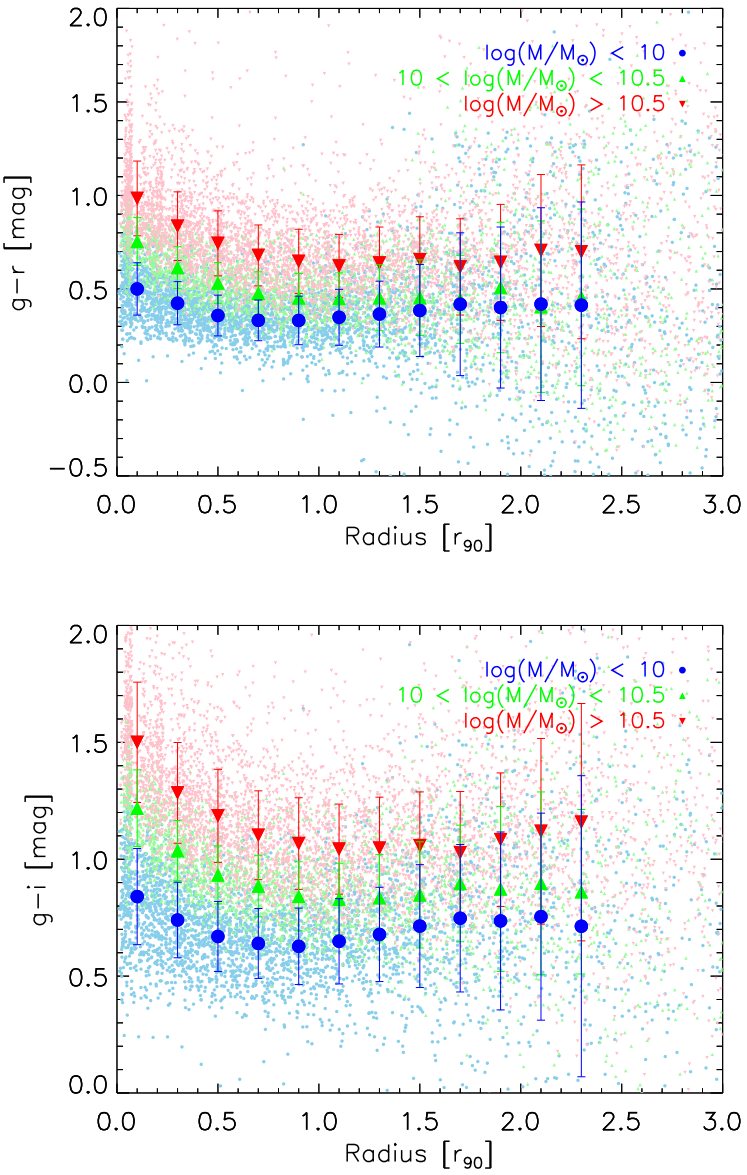

Figure 3.13: Composite radial profiles of colors. Upper panel: $g-r$; lower panel: $g-i$. The colors are Milky Way extinction corrected and K-corrected. Symbols and color-coding are as in the previous figure. Both the color profiles show a 'U'-shape with minima at around r_{90}.

slightly with increasing stellar mass (from ~ 0.8 to 1.0 r_{90}). In the botton panel we plot the g-band stellar mass-to-light ratio at a given location vs. the local stellar mass surface density. This shows the same qualitative behavior as the top panel (an obvious 'U'-shape), but the minimum in M/L occurs at the same value ($\Sigma_s \sim 10^7$ $M_\odot$ kpc^{-2}) in all three mass bins. The behavior of the stellar mass-to-light ratios for other bands are similar to that of the g-band but with diminished amplitude.

One interesting additional fact is that the location of the breaks in the g and r band composite radial profiles are exactly at the location of the bluest point in the color profiles (Fig. 3.13), $\sim r_{90}$. This is consistent with results in previous studies (e.g. Bakos et al. , 2008; Bakos & Trujillo , 2012). According to Fig. 3.12, the value of r_{90} is about 3 scale-lengths in the SB profiles. This is consistent with the locations of the PT06 breaks, but conflicts with the van der Kruit (1987) model.

To interpret the nature of the 'U'-shaped stellar mass-to-light ratio profile, we plot the composite radial profiles of the specific star formation rate (sSFR) in Fig. 3.15. This figure shows that the sSFR drops with increasing normalized radius in the outer disk in all three mass bins. The bottom panel plots sSFR vs. Σ_s and shows that sSFR reaches a (mass-dependent) maximum value at $\Sigma_s \sim 10^7$ kpc^{-2}. A complementary parameterization of the stellar population is shown in Fig. 3.16 which shows the r-band luminosity weighted mean age of the stars plotted as a function of normalized radius (top) and local surface mass-density (bottom).

Note that without UV and IR data we cannot unambiguously disentangle the

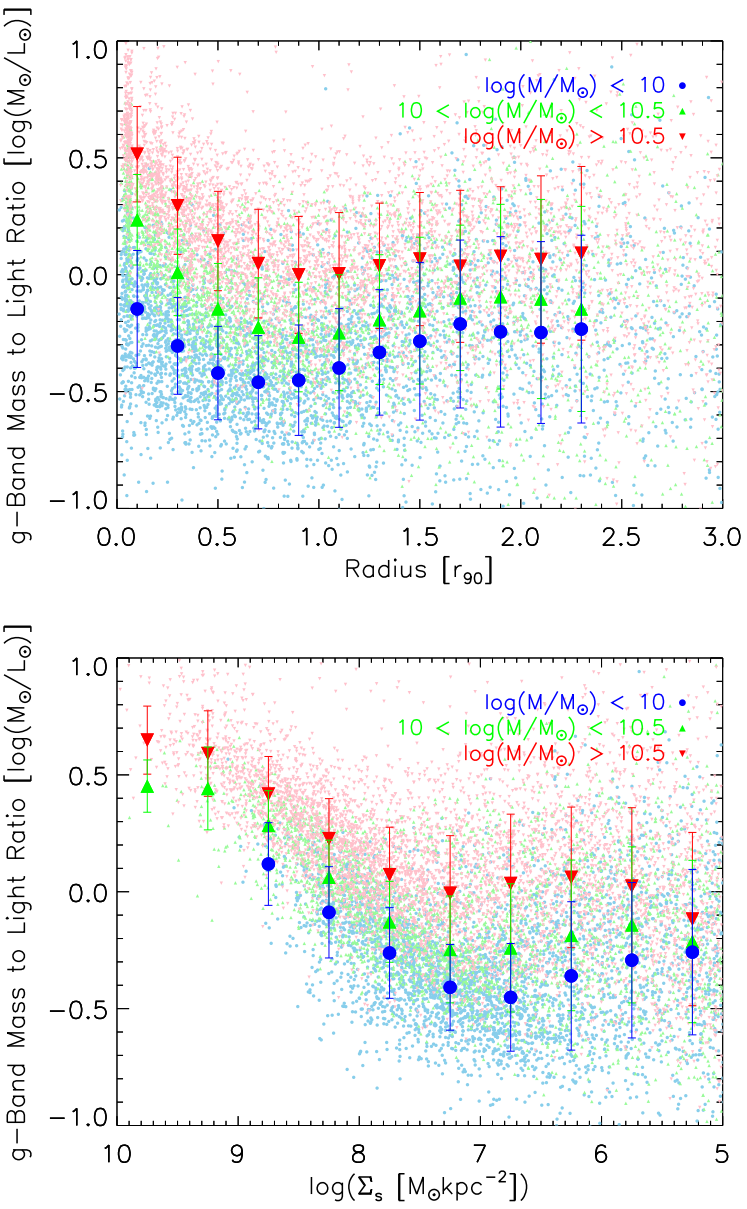

Figure 3.14: Composite g-band stellar mass-to-light ratio profile plotted as a function of radius (top) and local stellar surface mass density (bottom). Both plots show a 'U'-shape with a minimum at about r_{90} (top) and $\Sigma_S \sim 10^7$ M$_\odot$ kpc^{-2} (bottom).

effects of age and dust reddening on the observed colors (even though we have attempted to do so, as described in section 2). Nevertheless, it is difficult to imagine that the redder colors in the outer disk (or in the regions of low stellar mass surface density) are caused by an increase in the amount of dust reddening. This is completely unphysical at such low surface mass densities, where the corresponding gas and dust column densities will be small.

Finally, as expected, we note that our data show higher mass disk galaxies tend to have higher SB and be redder and lower mass galaxies tend to have lower SB and be bluer. This is also consistent with many previous studies (e.g. Bakos et al. (2008); Bakos & Trujillo (2012); Kauffmann et al. (2003b)).

In Figure 3.17 we show composite radial profiles of the g-band SB, the stellar surface mass density, and the g-band mass-to-light ratio for our sample binned in three ranges of C.

Three results are evident. First, the amplitude of the down-bending in the SB profile is largest for the lowest values of C and smallest for the largest values of C. Second, the amplitude of the 'U'-shaped mass-to-light radial profile follows the same pattern. Third, the stellar surface mass density radial profile is well described as a single exponential for all three bins in C. We conclude that there is a relationship between C (the bulge/disk ratio; Hubble type) and the radial gradients in the age of the stellar population between the inner and outer disk, even though the relative radial distribution of stellar mass is the same for both later and earlier-type disks

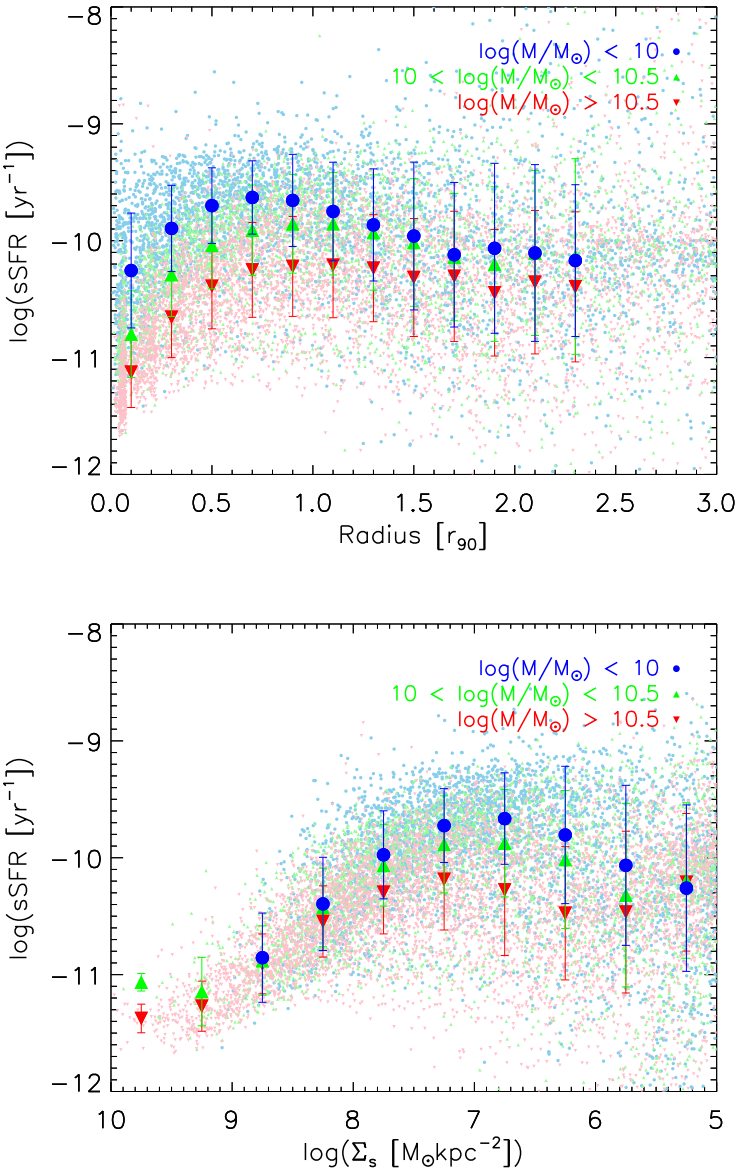

Figure 3.15: Composite radial profiles of specific star formation rate (sSFR). In all mass bins the specific star-formation rate reaches a maximum value at a radius of $\sim r_{90}$ (top) and $\Sigma_s \sim 10^7$ $M_\odot$ kpc^{-2} (bottom).

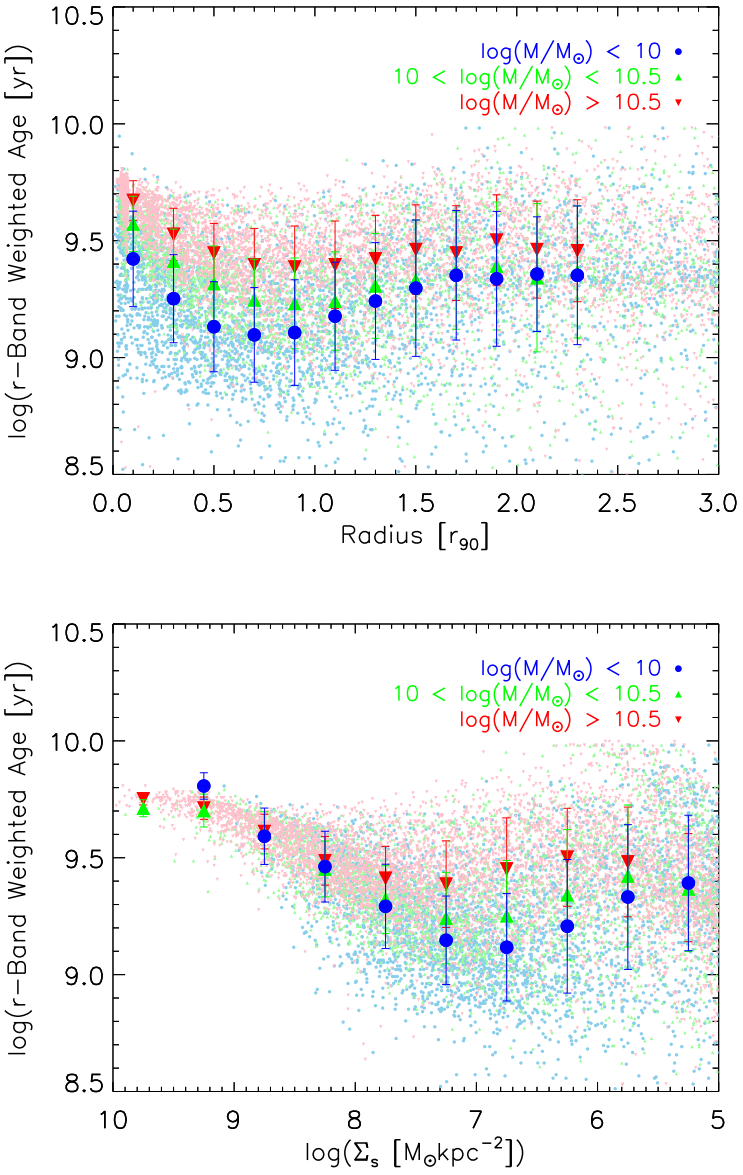

Figure 3.16: r-band weighted age radial profile stack plot. In all bins of stellar mass, the population is youngest at a radius of $\sim r_{90}$ (top) and $\Sigma_s \sim 10^7$ $M_\odot$ kpc^{-2} (bottom).

(pure exponential).

3.7 Properties of Individual Galaxies

PT06 and several following studies (e.g. Bakos et al. , 2008; Herrmann et al. , 2013) classify the SB radial profiles into three categories. However, these studies classify the profiles more or less subjectively in terms of establishing the division between Type I, II, and III. Also, the breaks are less obvious in redder bands than in bluer bands. Even in the same photometric band the inner-outer disk slope ratio (i.e. the strength of the break) is different from galaxy to galaxy. Thus, a better approach is to develop an automatic algorithm and derive a number which can describe the breaks quantitatively instead of qualitatively. In this section, we develop an objective automatic break finding algorithm and use the inner-outer disk slope ratio k_1/k_2, where k_1 and k_2 are defined as

$$\mu_1(r) = \mu_{0,1} + k_1\, r \quad (\text{if } r < r_b), \tag{3.6}$$

and

$$\mu_2(r) = \mu_{0,2} + k_2\, r \quad (\text{if } r > r_b), \tag{3.7}$$

where r is the radius of the profile, μ_1 and μ_2 are the inner and outer disk SBs in ABmag/arcsec^2, μ_{10} and μ_{20} are the central SBs interpolated using the inner and outer disk SB profiles respectively, and r_b is the break radius. The inner and outer

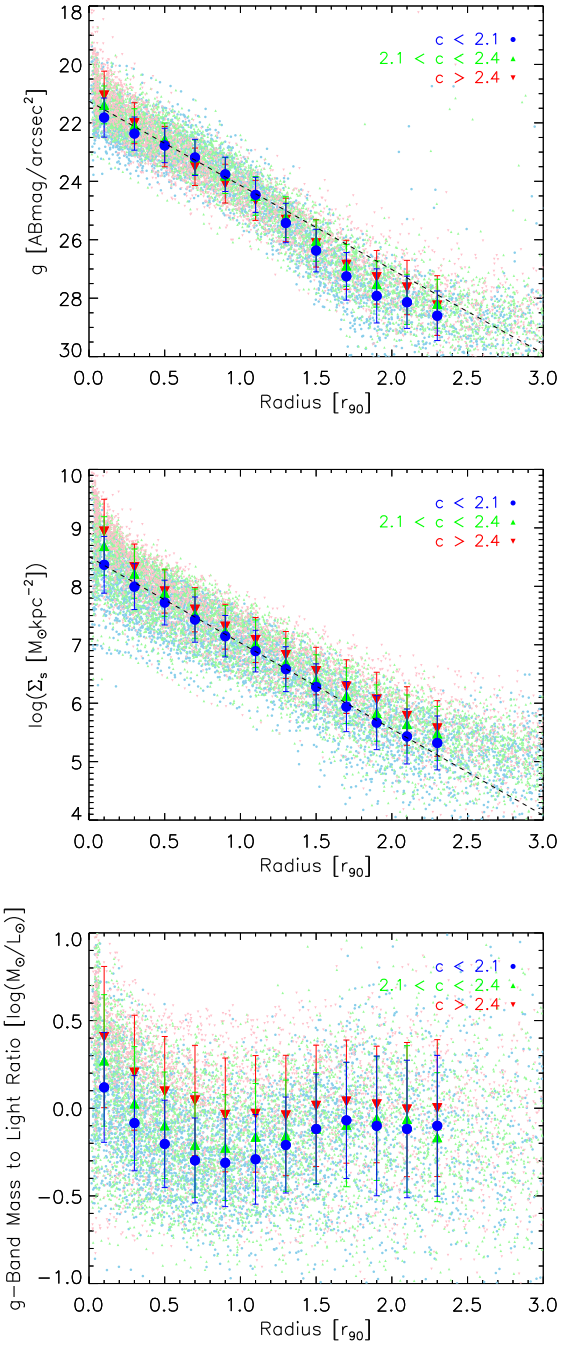

Figure 3.17: Composite radial profiles of g-band SB, stellar mass surface density and g-band mass-to-light ratio for our sample binned in three ranges of C. Symbols follow the convention of Fig. 3.12

disks are divided by the break radius r_b. Here we define the slope ratio as

$$R = k_1/k_2. \tag{3.8}$$

Therefore, a large slope ratio ($R > 1$) corresponds to the Type III (up-bending) profile; a small slope ratio ($R < 1$) corresponds to the Type II (down-bending) profile; and a unity slope ratio ($R \approx 1$) corresponds to the Type I (single exponential) profile.

3.7.1 The break-finding algorithm

It is very difficult to classify ~ 3500 SB radial profiles accurately and fully automatically for a couple of reasons: A typical SB profile contains three different parts: a Sersic profile for the bulge, an exponential profile for the inner disk and another exponential profile for the outer disk. Some galaxies even show a very extended profile for the stellar halo. The outer boundary of the bulge and the inner boundary of the stellar halo can be very different from galaxy to galaxy. Furthermore the radial profile can have wiggles (due to irregularities like spiral arms) and be very noisy in the outer low SB regime. Finally, galaxies can be classified as a combination of Type II and Type III (PT06). Previous studies (e.g. PT06 and Herrmann et al. , 2013) use human inspection in determining the type of the SB profiles.

Here we develop a fully automatic SB profile classification strategy. The strategy is based in part on the method developed by PT06 and several properties of the SB profiles described in section 3.6. According to section 3.6, breaks are generally more

obvious in bluer bands, e.g. g or r band. Furthermore, the SB radial profile break radius will not change from filter to filter, even though the inner/outer disk slopes ratio varies (cf section 3.6 and Bakos et al. , 2008). Since the r-band data have higher S/N than the g-band data, we use the r-band SB profile to derive the break radius and perform the profile classification.

One of the key points of the classification is finding the boundaries of the stellar disk and the location of the break radius. The inner boundary of the stellar disk is where the SB of the bulge is surpassed by the SB of the stellar disk and the outer boundary of the stellar disk is where the SB of the stellar disk is surpassed by the SB of the stellar halo or the rms of the sky background, which ever is higher. These boundaries are very hard to determine automatically: PT06 use human examination to determine the location of the inner boundary and set the outer boundary when the SB of the radial profile meets the rms of the sky background. The inner boundaries of PT06 are more accurate but the method is not suitable for our big sample. The outer boundaries of PT06 sometimes include part of the stellar halo Bakos & Trujillo (2012). Fortunately, for most of the galaxies in our sample, the bulge is significant (if at all) only within $0.3\,r_{90}$ and the stellar halo becomes significant outside $2\,r_{90}$ (cf. section 3.5 and 3.6). Therefore, we simply fix the inner and outer boundaries as $0.3\,r_{90}$ and $2\,r_{90}$ in this paper.

The location of the break radius is determined using two different methods: The first method is given by PT06: We first calculate the derivative of the r-band radial

profile within $0.3\,r_{90}$ and $2\,r_{90}$. The derivative profile is then smoothed to remove noisy points. The smoothed derivative profile should be a step function in an ideal situation (cf. Fig. 6 of PT06). We then search for the location of the biggest jump in the derivative profile around r_{90}. This location should be the break radius in most cases. The second method is based on the property of the mass-to-light ratio profile: The mass-to-light ratio profile usually shows a 'U' shape and the location of the 'U' shape minimum is almost always the location of the break radius. Since the 'U' shape is more obvious than the SB profile break it is much easier to fit the r-band mass-to-light ratio profile than to fit the r-band SB profile. We further simplify the algorithm by fitting the mass-to-light ratio profile using a skewed 'V' shape function (two straight lines joined around r_{90}). The minimum location of the 'V' shape function should be the break radius. After deriving the break radii using two independent methods, we fit the r-band SB profile using a broken exponential function with the break radius fixed using the values derived above. The break radius which results in a smaller χ^2 value is then our final best break radius for this specific galaxy.

The method works well for our galaxies but the reader should bear in mind that this classification is not as accurate as the method provided by PT06 because the inner bulge and outer stellar halo regions are assigned fixed values in radius. It is possible that some individual galaxies with an extended bulge and/or brighter stellar halo are misclassified in this strategy. However, our goal here is to draw statistical

conclusions based on the results for our full sample of 700 galaxies, as derived by this algorithm.

3.7.2 The slope-ratio R (in light and mass) and its correlation with other physical parameters

After determining the break radius, we calculate the slopes of the inner (k_{r1}) and outer (k_{r2}) disk r-band SB profiles. We also calculate the inner and outer disk slopes (k_{m1} and k_{m2}) of the stellar surface density profiles. The slopes of the stellar surface density profile are defined in a similar way as Eq. 3.6 and Eq. 3.7 except that the SB μ is replaced by stellar surface densities Σ in logarithmic scale. We plot the distribution of the r-band slope ratio (R_r) and the stellar surface mass density profile slope ratio (R_m) in Fig. 3.18. The distribution of $\log(R_r)$ looks like a Gaussian centered around -0.12 ($k_{r1}/k_{r2} = 0.75$), which means most galaxies have down-bending SB profiles. In comparison, the distribution of $\log(R_m)$ looks like a log-normal centered around 0 ($k_{m1}/k_{m2} = 1$), implying a single smooth exponential form. The statistical parameters of the distributions of $\log(R_r)$ and $\log(R_m)$ are listed in Table 3.2. The $\log(R_r)$ distribution has a slightly a larger rms and a some skewness, while the $\log(R_m)$ has a somewhat smaller rms and no skewness.

We also plot the slope ratios versus the concentration parameter ($C = r_{90}/r_{50}$, total stellar mass M_*, total star formation rate SFR, specific star formation rate

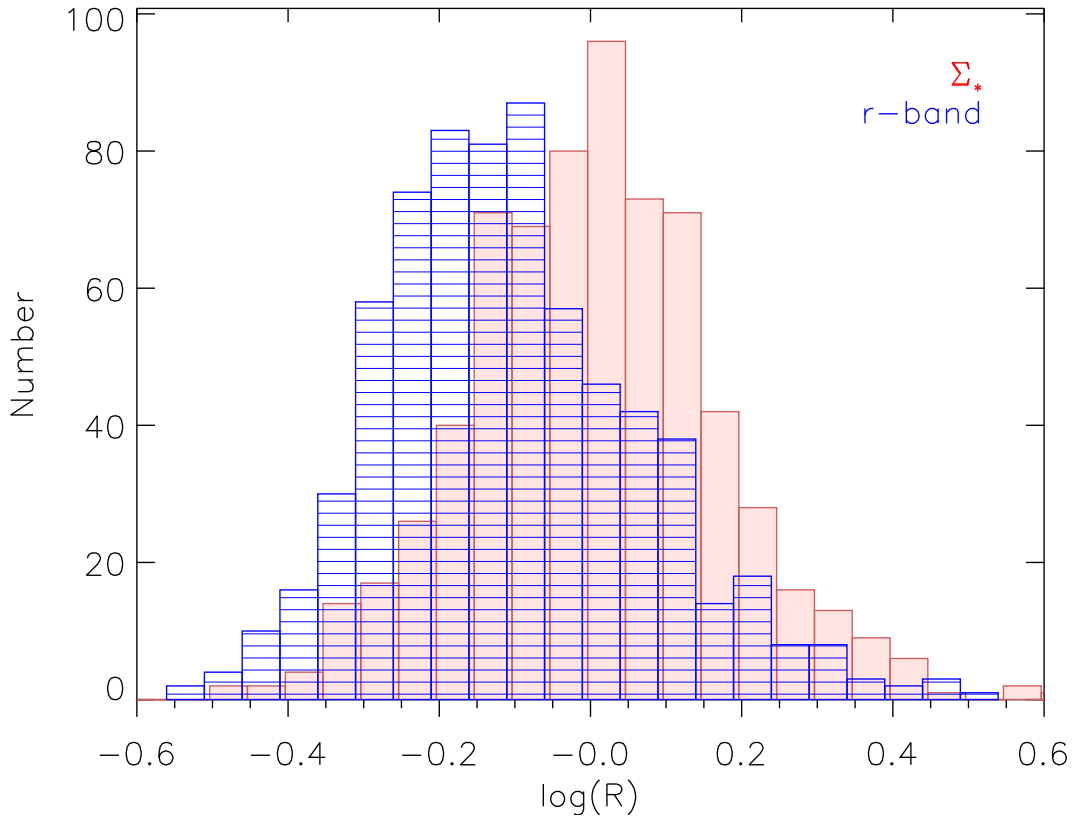

Figure 3.18: Ratio of inner and outer disk slopes (R). The distribution for the r-band implies most disk galaxies have down-bending outer surface brightness profiles ($R < 1$). The distribution for Σ_s peaks at $R = 1$, corresponding to a pure exponential profile. The typical errors in both forms of R are about 0.08 (about half the rms dispersion in the distributions).

Table 3.2: Statistics of $\log(R_r)$ and $\log(R_m)$ distribution.

	Mean	Median	Mode	rms	skew
$\log(R_r)$	-0.104	-0.121	-0.149	0.173	0.041
$\log(R_m)$	0.004	0.006	0.002	0.164	0.000

(sSFR=SFR/M_*), average stellar surface mass density ($\Sigma_* = M_*/\pi r_{90}^2$) and average SFR surface density ($\Sigma_{\rm SFR} = {\rm SFR}/\pi r_{90}^2$) in Fig. 3.19. Here r_{50} is the radius containing 50% of the r-band Petrosian flux, the values for M_* and SFR are derived in section 3.6.

There is a strong correlation between the R_r and C but no obvious correlation between the R_r and other parameters. The correlation of SB profile shape and C (Hubble type) is consistent with PT06 who found the disk SB profile types strongly correlate with Hubble types, with down-bending disks typically found to be later type galaxies.

We also plot k_{r1} and k_{r2} versus these physical parameters in Fig. 3.20. It also shows obvious correlation with the C but no obvious correlation with other parameters.

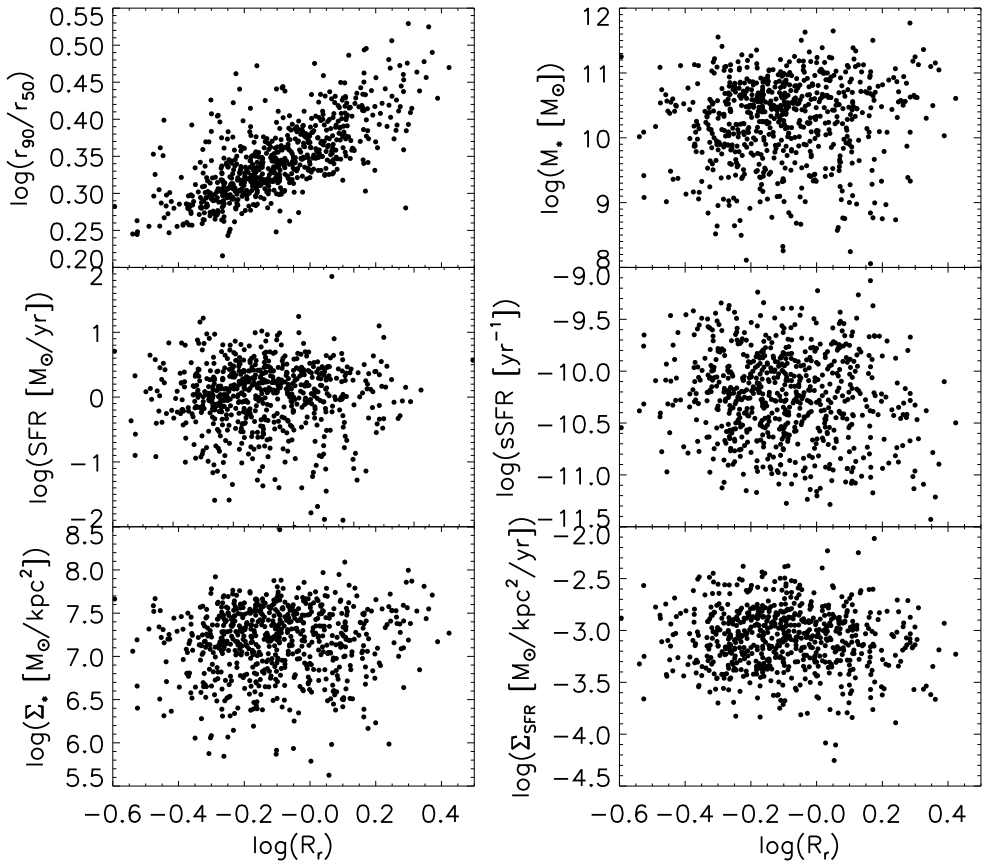

Figure 3.19: r-band slope ratio v.s. concentration parameter, stellar mass, total SFR, sSFR, Σ_* and Σ_{SFR}. The only strong correlation is with concentration, with later type disk galaxies having more strongly down-bending radial SB profiles.

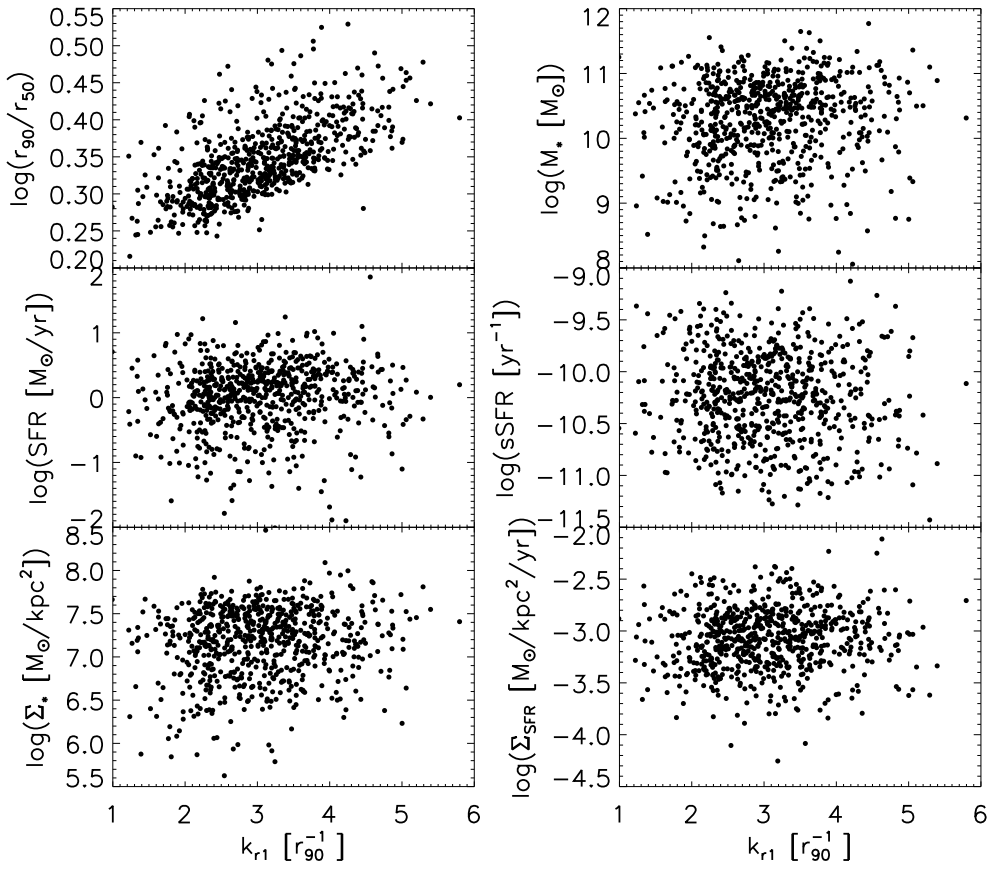

Figure 3.20: r-band k_{r1} v.s. concentration parameter, stellar mass, total SFR, sSFR, Σ_* and Σ_{SFR}. The only strong correlation is with concentration.

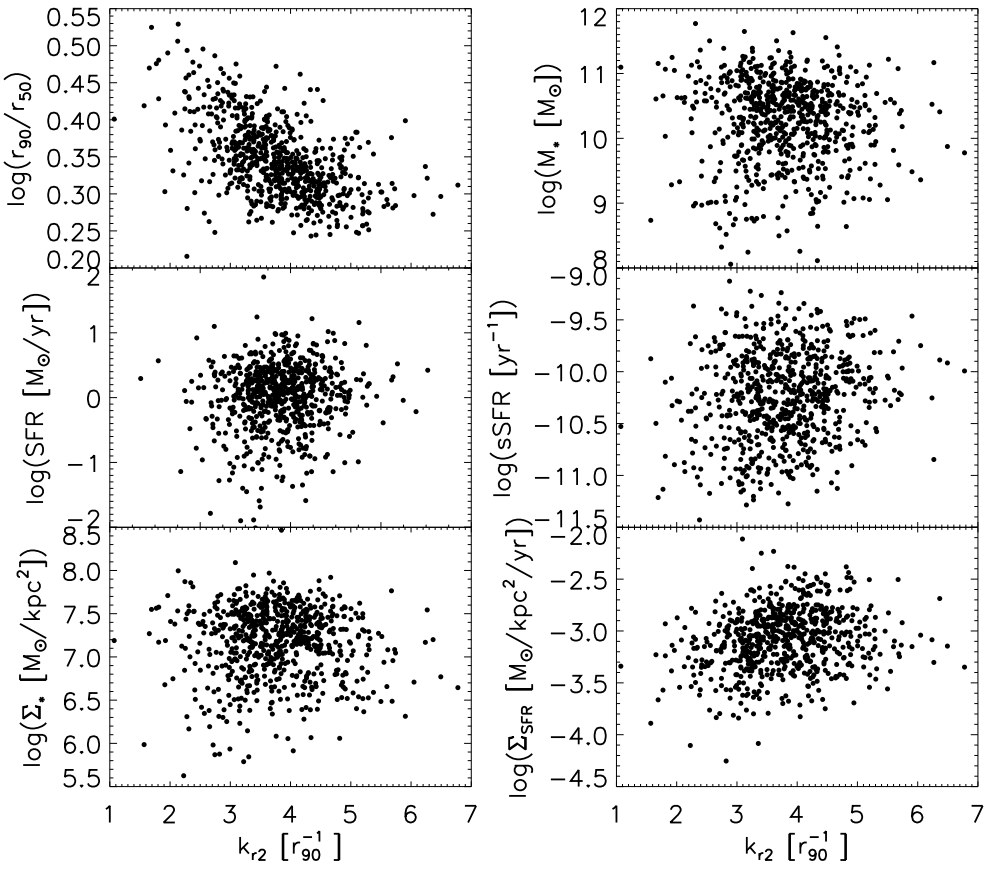

Figure 3.21: r-band k_{r2} v.s. concentration parameter, stellar mass, total SFR, sSFR, Σ_* and Σ_{SFR}. The only strong correlation is with concentration.

3.7.3 M/L radial profiles

One of the key results in section 3.6 is that the stellar mass-to-light ratio radial profiles of most galaxies have a 'U' shape with the minimum value located around r_{90}. However, Bakos et al. (2008) found that the $g-r$ color profile (which should correlate with the M/L profile), varies with different SB profile types: Type II disks have a 'U' shape color profile, Type I disks show a constant color in the outer disk, and Type III disk show a slight bluing after the break radius. It is therefore interesting to study the variation of the M/L radial profiles as a function of R_r.

For simplicity, we approximate the M/L profile using a skewed 'V' shape (instead of the more complicated 'U' shape) function similar to Eq. 3.6 and 3.7:

$$\log(\Upsilon_1(r)) = \log(\Upsilon_{0,1}) + k_{\Upsilon 1}\, r \quad (\text{if } r < r_b), \tag{3.9}$$

$$\log(\Upsilon_2(r)) = \log(\Upsilon_{0,2}) + k_{\Upsilon 2}\, r \quad (\text{if } r > r_b), \tag{3.10}$$

where Υ_1 and Υ_2 are the inner and outer disk stellar mass-to-light ratio in $M_\odot/L_\odot$.

We first plot the histogram of the slopes of the inner ($k_{\Upsilon_r 1}$) and outer ($k_{\Upsilon_r 2}$) disk r-band M/L profile in Fig. 3.22. The distribution of $k_{\Upsilon_r 1}$ is a Gaussian centered around -0.35 $\log(L_\odot/M_\odot)/r_{90}$, which means most galaxies show a decrease in M/L with increasing radius in the inner disk. The distribution of $k_{\Upsilon_r 2}$ is also a Gaussian, but centered around 0.2 $\log(L_\odot/M_\odot)/r_{90}$. This means most galaxies show an increase in M/L with increasing radius in the outer disk (consistent with the results we summarized in section 5 earlier based on the composite profiles). However, Fig. 3.22

shows that there is a range of properties, and exceptions to the rules.

In order to see how the radial gradients in the M/L ratio relate to the surface brightness profiles, we plot the R_r versus k_Υ in Fig. 3.23. This shows that the radial dependence of the M/L in the outer disk ($k_{\Upsilon_r 2}$) correlates strongly with R_r. Several specific results are noteworthy. If we confine the analysis to galaxies with $R_r \leq 1$ (down-bending surface brightness profiles), then galaxies with larger down-bending break amplitudes (smaller R_r) have stronger radial gradients in the M/L ratio in the outer disk. This is consistent with the result that even strongly down-bending r-band profiles can be produced by disks with single exponential surface mass density radial profiles. Moreover, for the down-bending galaxies, the inner disk slope $k_{\Upsilon_r 1}$ is nearly a constant as a function of R_r, with nearly all such disks showing a decrease in M/L with increasing radius in the inner disk. Interestingly, the up-bending disks ($R_r > 1$) behave differently: any radial gradient in M/L is weak in both the inner and outer disk. This implies that the up-bending disks also have up-bending stellar surface mass-density profiles.

We also plot both $k_{\Upsilon_r 1}$ and $k_{\Upsilon_r 2}$ versus different galaxy parameters in Fig. 3.24 and 3.25. The strongest correlation is between C (bulge/disk ratio, Hubble type proxy) and the radial gradient of M/L in the outer disk ($k_{\Upsilon_r 2}$. The early type disks are more likely to show M/L profiles in the outer disk that are flat.

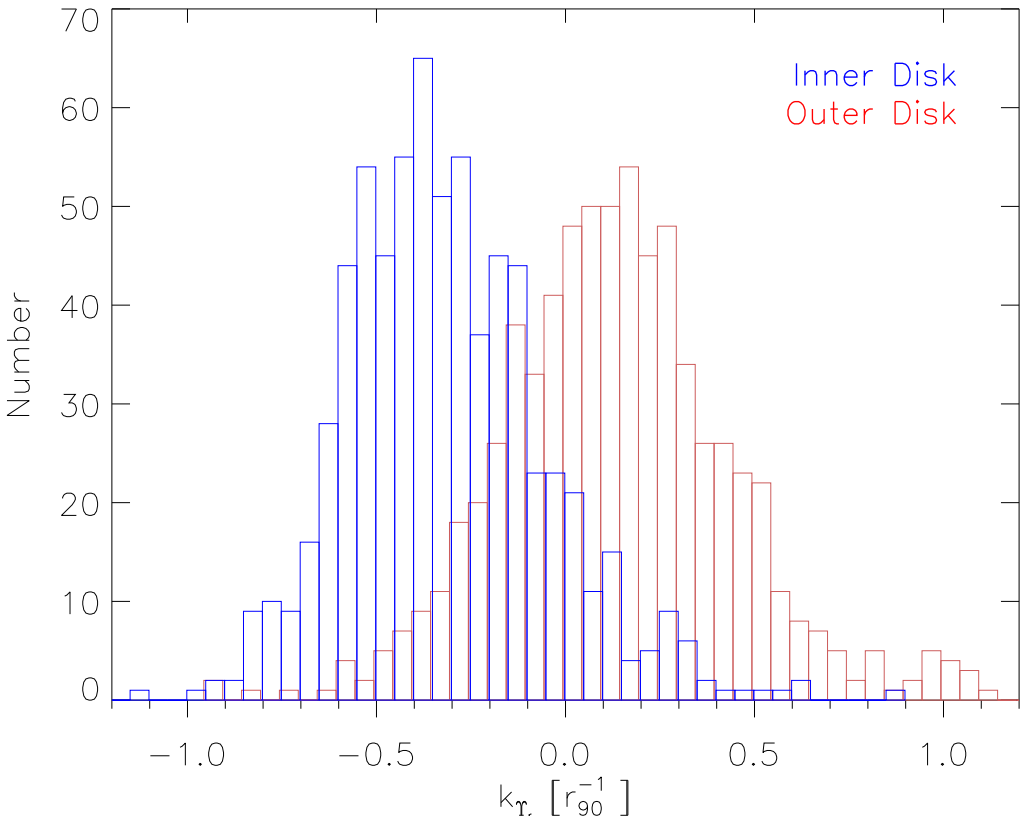

Figure 3.22: Histogram of the slopes of the inner and outer disk r-band M/L profile. Most galaxies show radial increases in M/L in the inner disk (blue histogram) and radial decreases in M/L in the outer disk (red histogram). The typical uncertainty in k_{Υ} is about 0.01.

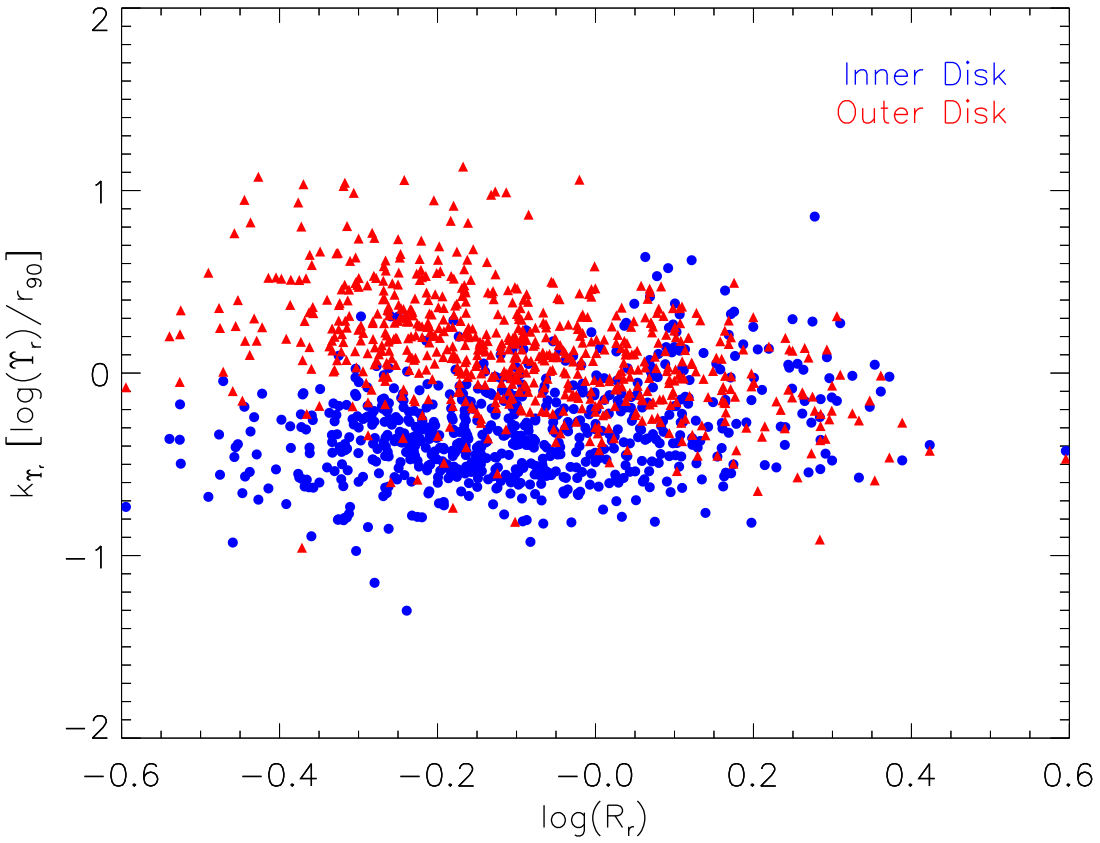

Figure 3.23: Correlation between R_r and the slopes of the inner and outer disk M/L profile. Most down-bending disks ($\log(R_r < 0)$ show M/L values that decline with radius in the inner disk and increase with radius in the outer disk. The up-bending disks ($\log(R_r) > 0$) typically show only weak radial gradients in M/L in either the inner or outer disk.

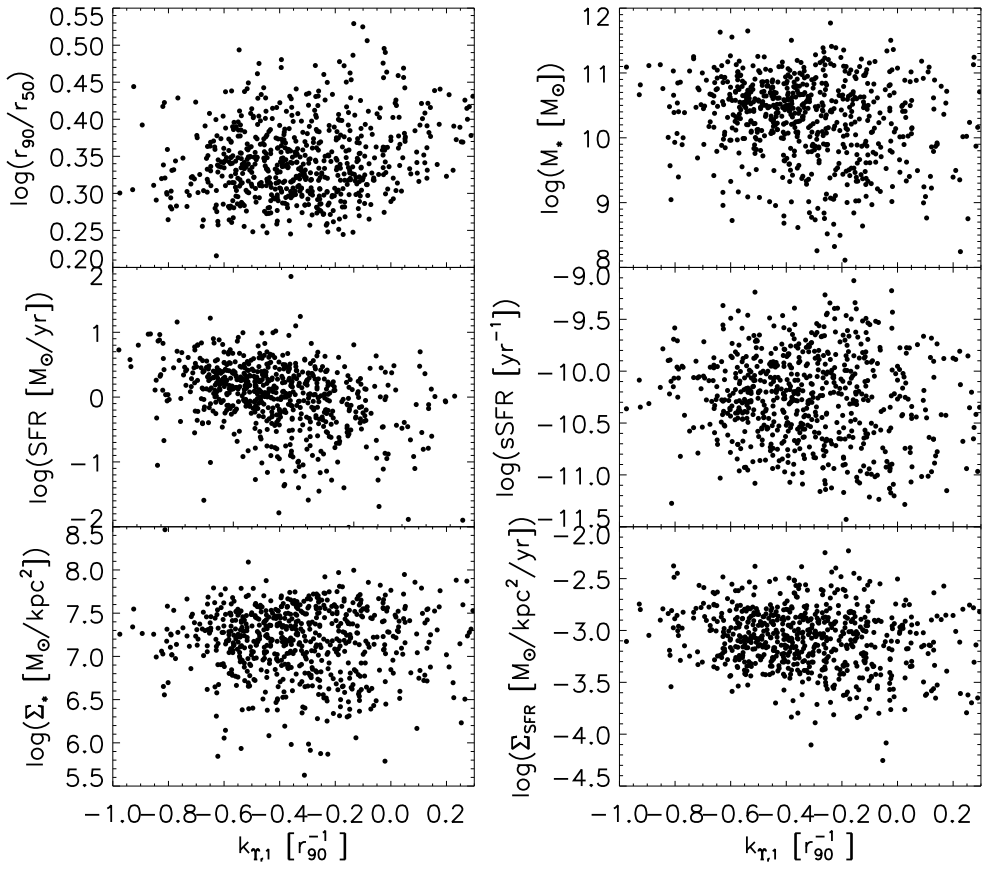

Figure 3.24: Slope of the inner disk r-band M/L profile, $k_{\Upsilon_r 1}$ v.s. concentration parameter, stellar mass, total SFR, sSFR, Σ_* and Σ_{SFR}. There are no strong correlations.

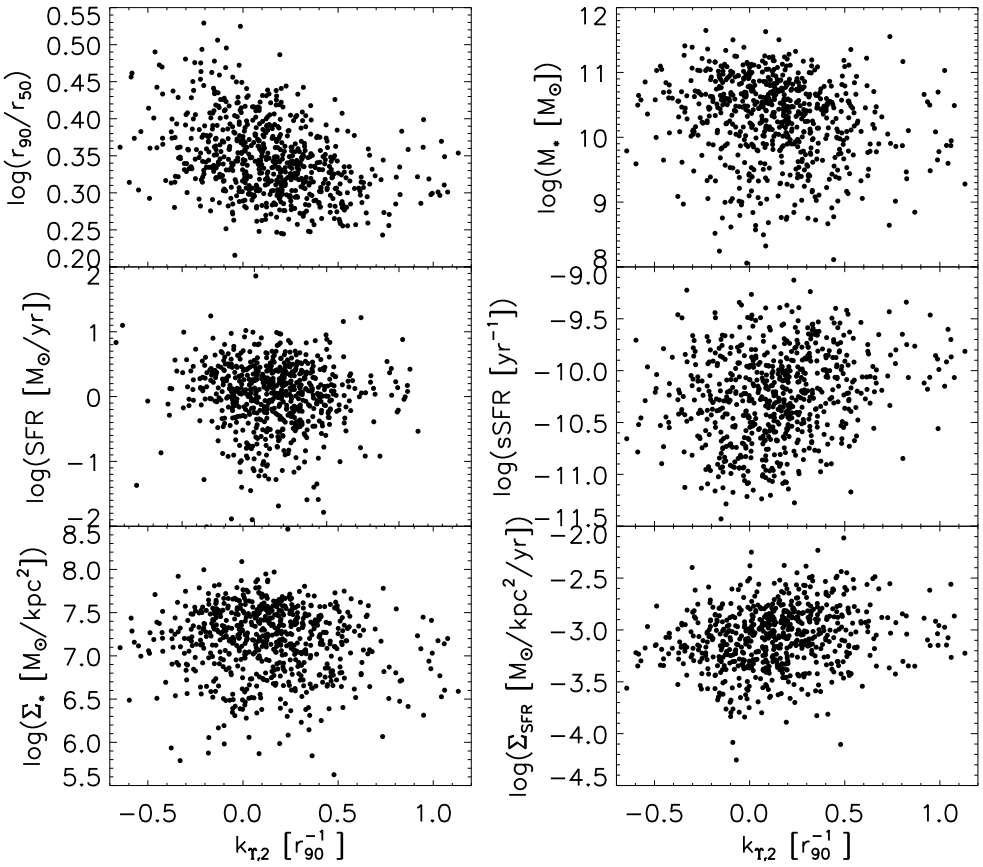

Figure 3.25: Slope of the outer disk r-band M/L profile, $k_{\Upsilon,r2}$ v.s. concentration parameter, stellar mass, total SFR, sSFR, Σ_* and Σ_{SFR}. The only strong correlation is with concentration: later type disk galaxies have stronger radial increases in M/L in the outer disk.

3.8 Discussion

3.8.1 PSF

Deep stacked images can reveal the effects of the extended and faint wings of the image point spread function (PSF) (de Jong , 2008). Thus, it is important to examine the contribution of the extended wings of the PSF to the outer disks and stellar halos. Zibetti et al. (2004) calculated an effective PSF for the SDSS using a stacked image of stars selected from their galaxy images following a similar galaxy stack procedure described in section 3.5. Although their effective PSF has an extended wing, the decline in the core is very sharp, 6-7 mag/arcsec^2 within 2" and the extended wings contribute less than $1/10^4$ of the central SB at radii larger than 8". They claim that the extended PSF wing has only a minor effect on the stellar halo detection, based on an examination of a PSF-convolved model galaxy. However, de Jong (2008) claimed that the mean or median stacked image in better than the mode image used by Zibetti et al. (2004). He further claimed that the PSF has a major effect on the halo detection (20-80% of the halo light) along the minor axis of edge-on galaxies. However, he also concluded that an extended halo component is still needed to fully fit the observations.

Here we follow the procedure described by de Jong (2008) for calculating the effective PSF through stellar stacking method: We first select a star, which is within 2 mag difference from the central brightness of the target galaxy but far away from

other objects. We take these stars from each image and rotate and rescale the image centered on the star following the procedure described in section 3.5. All other objects other than the selected star in the image are then masked. We then combine all the stars and calculate a mean image of the stars. The surface brightnesses of the stars are scaled to the central SB of the star and outerlier pixels are clipped in the calculation. The final effective PSFs are calculated and shown in Fig. 3.26. The resultant effective PSFs in different bands do have extended wings out to radii of 15". The g, r, i, z-band PSFs are very close to each other but the y-band PSF has a slight up turn beyond a radius of 3". However, the PSFs of all 5 bands decline sharply by 7-9 mag within 7", the r_{90} of the stacked galaxy image. This is far below the SB around the break radius. We thus claim that although the extended PSF wing might have some effects on the detection of the stellar halo, it should have very minimal effects on the composite stellar disk profiles.

In order to quantify the effect of the PSF on the SB profiles, we made a 1-D galaxy model and convolved the model with the PSF. The model galaxy has an exponential disk and a point source in the center. The exponential disk has $g - i = 0.8$ and the point source has $g - i = 1.4$. The flux ratio of the point source and the exponential disk is 0.5. This is meant to be a simplified model of the galaxies in our sample with the larger bulge/disk ratio where the effects of the PSF wings on the measured colors of the outer disk will be most severe. The model galaxy and the PSF convolved SB and color profiles are plotted in Fig. 3.27. The halo region ($\sim 2 - 3r_{90}$) does

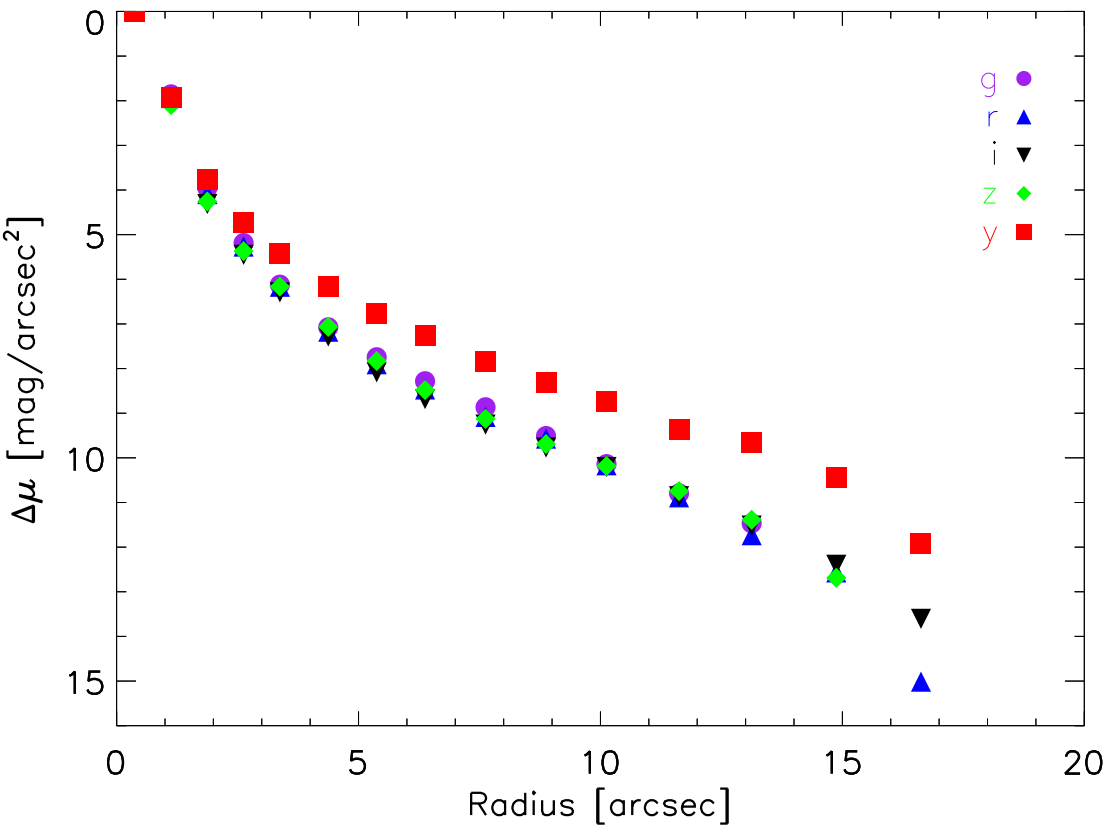

Figure 3.26: The PSF profiles.

have an spurious up-turn with the $g-i$ color by 0.1, but the color of the disk region ($\sim 0.5-2r_{90}$) has almost no change from the input model.

3.8.2 Comparison to Previous Studies

Previous studies of radial profiles of the stellar component of disk galaxy profiles have usually been limited to the region interior to R_{25} radius (or r_{90}). These typically have shown color profiles that become bluer with increasing radius (e.g. MacArthur et al. , 2004). It is only recently that systematic studies of the outer disks have shown the trend toward redder colors that is seen in our deep images.

While are results are based on integrated SEDs of the stellar population, similar results have been found using photometry of resolved stars to produce color magnitude diagrams (CMDs). For example, Radburn-Smith et al. (2012) found a similar trend in NGC 7793 and Thilker et al. (in prep.) also found the outer disk of M83 to be dominated by an old stellar population (although with the degree of dominance dependent on galactocentric radius). However, Gogarten et al. (2010) also used CMDs of resolved stars, but found no up-turn in the radial age profile of NGC 300. Some spectroscopic studies, such as Delgado et al. (2014); Yoachim et al. (2010, 2012) using IFU spectra, do show some example of an up-turn in the radial age profile at larger radii.

The general trend for galaxies to have redder (older) outer disks was first reported by Bakos et al. (2008) using the PT06 sample. They classified the radial color profiles

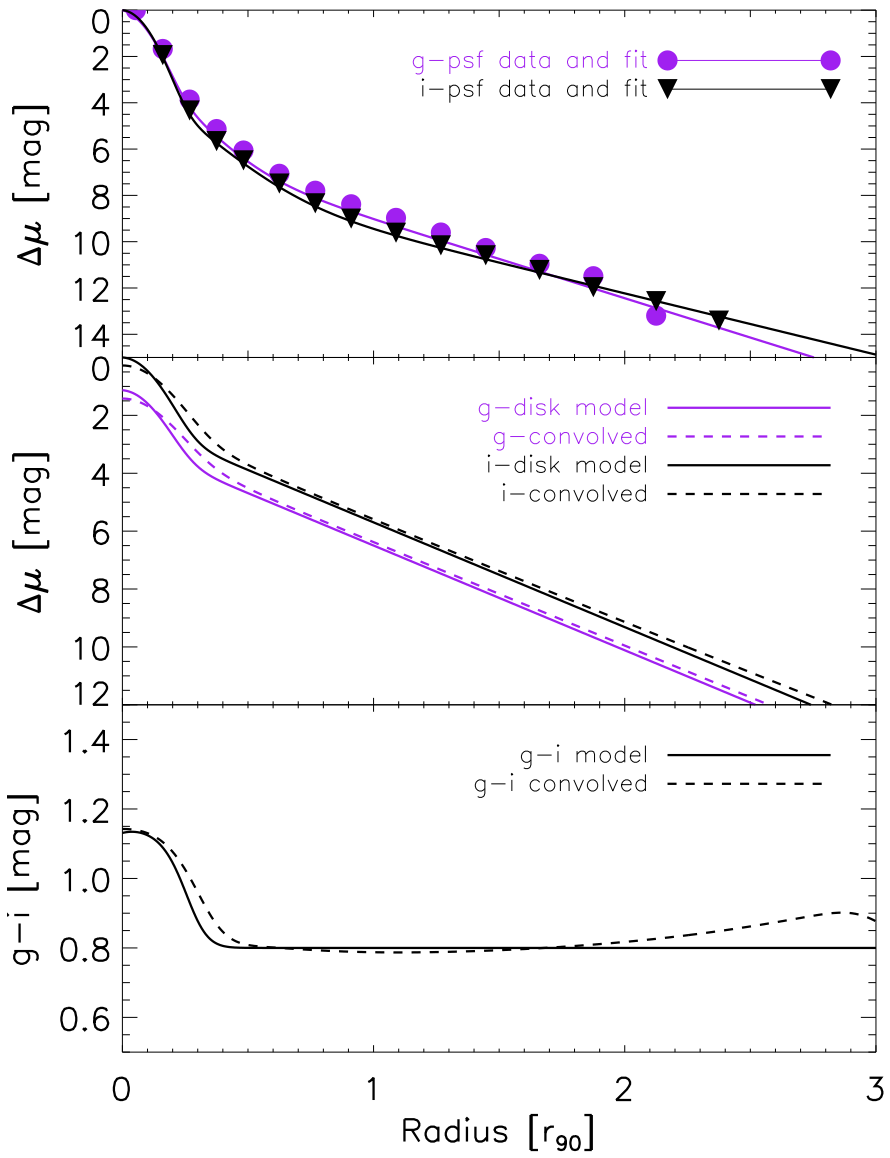

Figure 3.27: The 1-D galaxy model and the PSF convolved profiles. Upper-panel: g-band (purple) and i-band (black) PSF. The symbols are measured data and the lines are functional fit. The PSFs are fitted using a Gaussian plus a broken exponential profile. Middle-panel: g-band (purple) and i-band (black) SB profiles. Lower-panel: $g-i$ color profiles. Solid lines are the original model and dash lines are the model after convolution with the PSF.

into three different types corresponding to the SB profile types. They found that the Type II (down-bending) SB (g and r-band) galaxies usually have a 'U'-shaped color profile with the location of the minimum (bluest colors) corresponding to the SB profile break radius. The Type III (up-bending) SB galaxies also have a minimum in the radial color profile but its location does not correspond to the break radius. The Type I (single exponential) SB galaxies have a gradual decrease in the color profile until about 1.3 disk scale-lengths and the colors then stays constant in the outer disk. D'Souza et al. (2014) also find 'U'-shaped color profiles in stacked images of late-type galaxies

To explicitly compare our results to those in Bakos et al. (2008), we selected the 100 most down-bending galaxies ($R_r < 0.3$), the 100 galaxies with profiles closest to single exponentials ($0.89 < R_r < 1.106$) and the 100 most up-bending galaxies ($R_r > 1.26$). We then used these galaxies to reproduce Fig. 1 of Bakos et al. (2008). The plot is shown in Fig. 3.28. It roughly matches some of the properties described by Bakos et al. (2008), however we do not see a clear minimum in the color profile in the Type III galaxies. In fact, the near constant color we see in the Type III galaxies beyond a radius of $\sim 0.5\, r_b$, combined with the up-bending SB profile, results in a corresponding up-bending in the surface mass density radial profile. This is unlike the more common Type I and II disks, which have single exponential distributions of stellar mass density.

Bakos & Trujillo (2012) used the deep SDSS Stripe82 imaging data to analyze SB

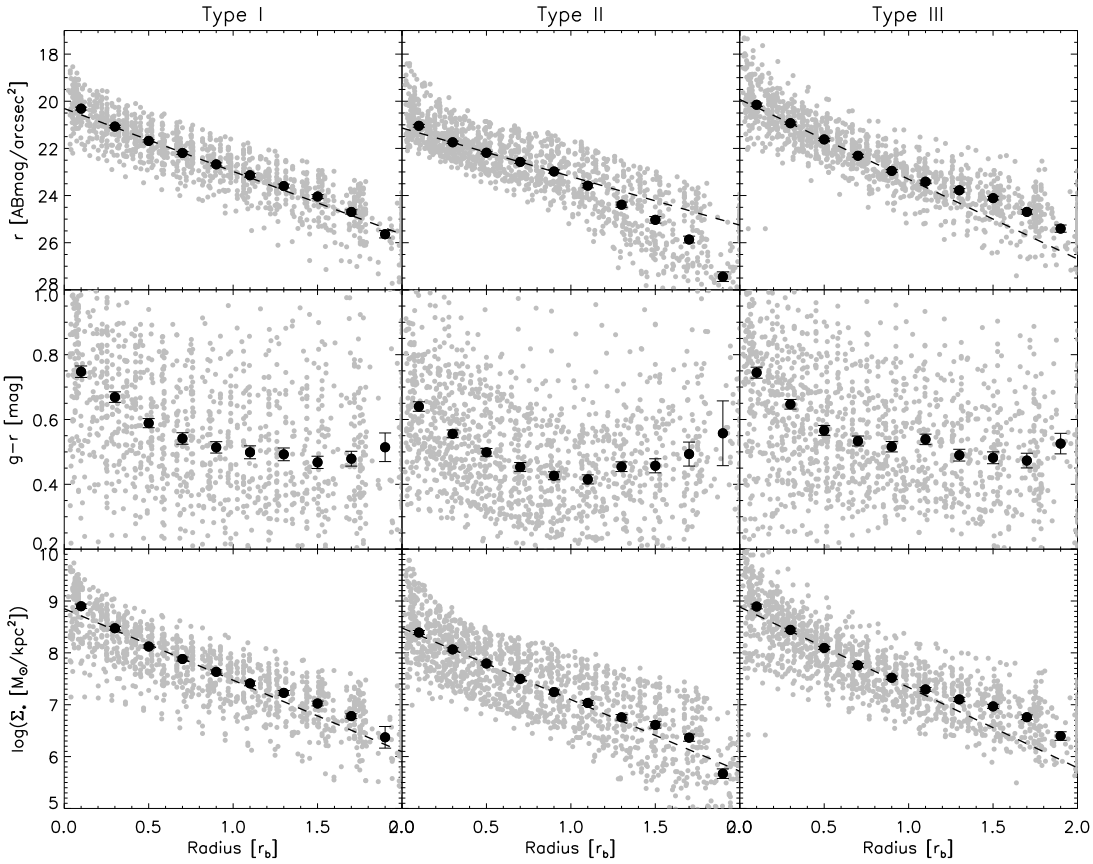

Figure 3.28: r-band SB (top row), $g-r$ color (middle row) and stellar surface mass density (bottom row) profiles of 'Type I' (left column), 'Type II' (middle column) and 'Type III' (right column) disks. All three types have sample size of 100 galaxies. The plot is intended to have the same format as the Fig. 1 of Bakos et al. (2008): The gray dots are individual galaxy profiles and the black dots show the median values. The vertical bar shows $\sigma/\sqrt{N}$ for each radial bin, where N is the number of points in that radial bin. The dash lines are the linear fit to the black dots between $0.3-1\,r_{90}$. The radius is scaled in break radius r_b.

and color radial profiles of 7 galaxies down to $30 mag/arcsec^2$ depth. The depth is similar to our data and it reaches the stellar halo region at around $27.5-30 mag/arcsec^2$. The only Type I galaxy in this sample also shows an up-turning feature in the radial color profile in the outer disk. They found that the stellar halo starts to affect the SB profile at the level of about 28 mag/arcsec^2 and they claimed that the stellar halo could be responsible for the previous classification of Type III galaxies. Two of the examples, NGC 7716 and NGC 1087, are claimed to be affected by the tidal streams in the stellar halo.

In this paper, we obtained SB profiles down to $28-30$mag/arcsec^2, similar to that of Bakos & Trujillo (2012) and thus we should be able to detect the effect of the stellar halo and investigate whether galaxies with $R_r > 0$ (Type III galaxies) are caused by the stellar halo. The results in Section 3.5 indicate that the ellipticity profile of the isophotes of the stacked images starts to decrease only slowly beyond $\sim 1.5\, r_{90}$, and the stellar surface mass density profile starts to turn up after $\sim 2\, r_{90}$ in generic disk galaxies. However, the SB profile of 100 most up-bending galaxies (Fig. 3.28) shows an upturn in the surface mass density around $r_b\, (\sim r_{90})$ where the halo light should be negligible. This implies that although some of the Type III galaxies might be caused by the stellar halo, the up-turn in most such galaxies is produced by the disk.

3.8.3 Implications for outer disk formation

Let us conclude by discussing our results within the context of the mechanisms that determine the structure and stellar content of the outer disk. In the standard formation scenario (e.g. Fall & Efstathiou , 1980; Mo et al. , 1998), galaxies form in cold dark matter halos. Galaxies continue to accrete gas from the circum-galactic medium during their evolutionary history. Gas accreted in later times typically has higher angular momentum and will therefore remain in the outer disk because of the conservation of specific angular momentum during the infall process (e.g. Guo el al. , 2011; Fu et al. , 2013). Since gas is the fuel of star formation, the outer disk should be more gas rich and composed of a younger population of stars compared to the inner disk. This is called the inside-out formation process. The inside-out picture is supported by numerous observations (e.g. Wang et al., 2011) and is widely accepted by the community. However, at first sight some of the results in this paper appear to be at odds with this simple picture, because the outer disks are frequently found to be older than the inner disk.

There are two plausible ways that in principle - could reconcile these results with the simple inside-out model. The first involves truncation of star formation in the outer disk. One interesting feature of our results is that the minimum values of mass-to-light ratio and stellar age are generally located in the region in the galaxy disk where the stellar mass surface density has a value of $\sim 10^7 M_\odot/kpc^2$ (lower panel of Fig. 3.14). This is the same value as the mean stellar mass surface density at the break

radius of the PT06 type II galaxies, $10 M_{\odot}/pc^2$, (Bakos et al. , 2008; Bakos & Trujillo , 2012). Assuming the scale height of the disk to be $100pc$, we can convert this surface mass density into a volume number density of about 0.1 proton cm^{-3}. This is the general star formation threshold used in many simulations (e.g. Roškar et al. , 2008), although the threshold is formulated as gas density.

Roškar et al. (2008) argue that the 'U'-shaped color/age radial profile is not caused by the star formation threshold but rather by a rapid drop of gas surface density. However, Sánchez-Blázquez et al. (2009) argue that the gas surface density cannot drop so rapidly, based upon their fully cosmological simulation of disk galaxy formation. Instead, they suggest that the drop in star-formation in the outer disk is due to the warp/flare in gas disk which reduces the gas volume density more strongly than the gas surface density (see also Ferguson , 1998). Our galaxies are so distant that we cannot easily detect gas and star formation occurring at the SFR surface densities typical for XUV disks, at least in radial profile form. A similar study of local galaxies employing GALEX and HI data would be helpful to reveal the relation between the star formation threshold and the break. Bigiel & Blitz (2012) studied neutral gas profiles of 33 nearby spiral galaxies and found that the combined total gas radial profile is pure exponential that decreases slowly, with a scale-length $\sim 0.6\, R_{25}$, out to about $2\, R_{25}$. The molecular-to-atomic Hydrogen transition radius in their study is about $0.7\, R_{25}$, which is comparable to r_{90} in our paper and this supports the idea that the break radius might be caused by star formation threshold instead of rapid drop of

total gas surface density.

A star formation threshold by itself cannot explain the pure exponential surface mass density profile that extends to the outer disk. A plausible explanation is to violate the implicit assumption that most of the stars currently in the outer disk were formed in-situ. There is in fact growing evidence that the radial migration of stars plays an important role in establishing the structure and stellar content of galaxy disks. Sellwood & Binney (2002) proposed a dynamical churning mechanism that will cause radial stellar migration. Roškar et al. (2008) studied the effect of stellar radial migration in disk formation for an isolated model galaxy. They found that the stellar radial migration does have a large effect in redistributing stars. The migration distance can be very large (up to $\sim 10kpc$). They conclude that Type II disks can be formed as a consequence of the interplay between this outward transport of disk stars and a cutoff in the star formation in the outer disk. Their predicted age profile shows a 'U'-shape, with a minimum at a stellar surface mass density of $10M_{\odot}/pc^2$. This fits our results very well. However, their models predict that the location of this region of minimum age corresponds to a downward break in the radial profile of the stellar mass surface density. This contrasts with our results that the stellar surface mass radial profile is a pure exponential with no obvious break.

Sánchez-Blázquez et al. (2009) extended this investigation by simulating a disk galaxy in a full cosmological environment (in which the galaxy experiences cosmological gas infall and/or interactions with other galaxies). Gas infall and minor mergers

not only expand the galactic disk but also induce density perturbations which enhance stellar radial migration. Their simulations yield age and sSFR radial profiles that appear similar to our observational results. Furthermore, they find that the breaks in the SB profiles only exist in bluer bands, and that the stellar mass surface density profile is close to exponential (again, in agreement with our results). They argue that break in the radial blue SB profile is due to a decrease in the star formation rate per unit area in the outer disk which is caused by a decrease in the volume density of gas at the break radius. They attribute this drop in density to the onset of a warp and flaring of the outer gas disk. Thus, while radial migration is important is producing an exponential stellar mass surface density profile, radial migration alone cannot explain the age gradient (the truncation of recent star formation in the outer disk is needed). Matínez-Serrano et al. (2009) reach qualitatively similar conclusions. More recently, Bird et al. (2013) have used numerical simulations to dissect in detail the build up of the stellar disk of a Milky way-like galaxy over cosmological time. This work again highlights the importance of the interplay between radial migration and the truncation of star formation in the outer disk.

Despite this emerging consensus, there is still some uncertainty about the detailed mechanism that drives radial migration. Previous theoretical studies (Sellwood , 2013, and references therein) show that the churning effect (which was the mechanism originally proposed to derive stellar radial migration) does not heat up the disk. However, Minchev et al. (2012) simulated the evolution of an initially truncated galaxy in a full

cosmological environment. They claim that the stellar migration is mainly due to the effects of the bar plus the spiral arms, instead of the churning mechanism (which mostly effects stars around the co-rotation radius). They found that the outer disk stars that migrated from inner disk should exhibit high velocity dispersions, especially in the radial direction. Thus observations of stellar velocity dispersions in the outer disk of the Milky Way might provide important constraints on the physics behind radial migration.

One conclusion then would be that stellar migration has a significant influence on the outer disk formation and is mostly due to resonant effects induced by spiral arms and/or bars. However, this the leads to a question as to why the dwarf irregular galaxies, which do not have significant spiral arms or bars, also show 'U'-shaped color/age profiles (Herrmann et al., 2013). A possible explanation is that radial migration in dwarf irregular galaxies is caused by resonant effects associated with bar-like density maxima.

Another question is about how much stellar mass can be transferred to the outer disk from the inner disk via radial migration. This is a difficult question to answer precisely from our data but we can roughly estimate the percentage of migrated stellar mass needed in the outer disk. Given a pure exponential disk with a scale length of $0.3r_{90}$, we would expect (by simply integrating the exponential function over the disk) the inner disk ($r < r_{90}$) contains about 85% of the total stellar mass and the outer disk ($r > r_{90}$) contain less than 15% of the total stellar mass. Here, using the derived

stellar mass radial profiles for our sample galaxies, we calculate the percentage of stellar mass for different parts of each galaxy. The histograms of the percentage are shown in Fig. 3.29. The bulge here is defined as the part of the galaxy within $0.3\,_r90$; the inner disk is defined as the part of the galaxy between $0.3\,r_{90}$ and r_{90}; and the outer disk is defined as the part of the galaxy between r_{90} and $2\,r_{90}$. Suppose 57% (Sánchez-Blázquez et al. , 2009) of the outer disk stars were formed in the inner disk. Then the stellar mass that migrated from the inner to the outer disk is only $< 9\%$ of the total stellar mass of the galaxy. This is a small fraction, but nevertheless has a significant impact on the properties of the outer disk.

3.9 Summary

Making use of deep stacked Pan-STARRS1 multi-band imaging observations, we have conducted an investigation of the structure and stellar content of 700 disk galaxies selected from SDSS. These galaxies were selected to span a range of bulge/disk ratios and to be relatively face-on. The mass range we sample well extends from $\sim 10^9$ to 10^{11} $M_\odot$. In particular, we modeled the five-band ($grizy$) images to determine the gradients in surface brightness (SB), color, stellar mass surface density, stellar mass-to-light ratio, specific star formation rate, and luminosity-weighted mean age over a range of radii typically reaching twice the characteristic size (r_{90}) of the galaxy. Compared to previous related studies our sample is much larger, is more rep-

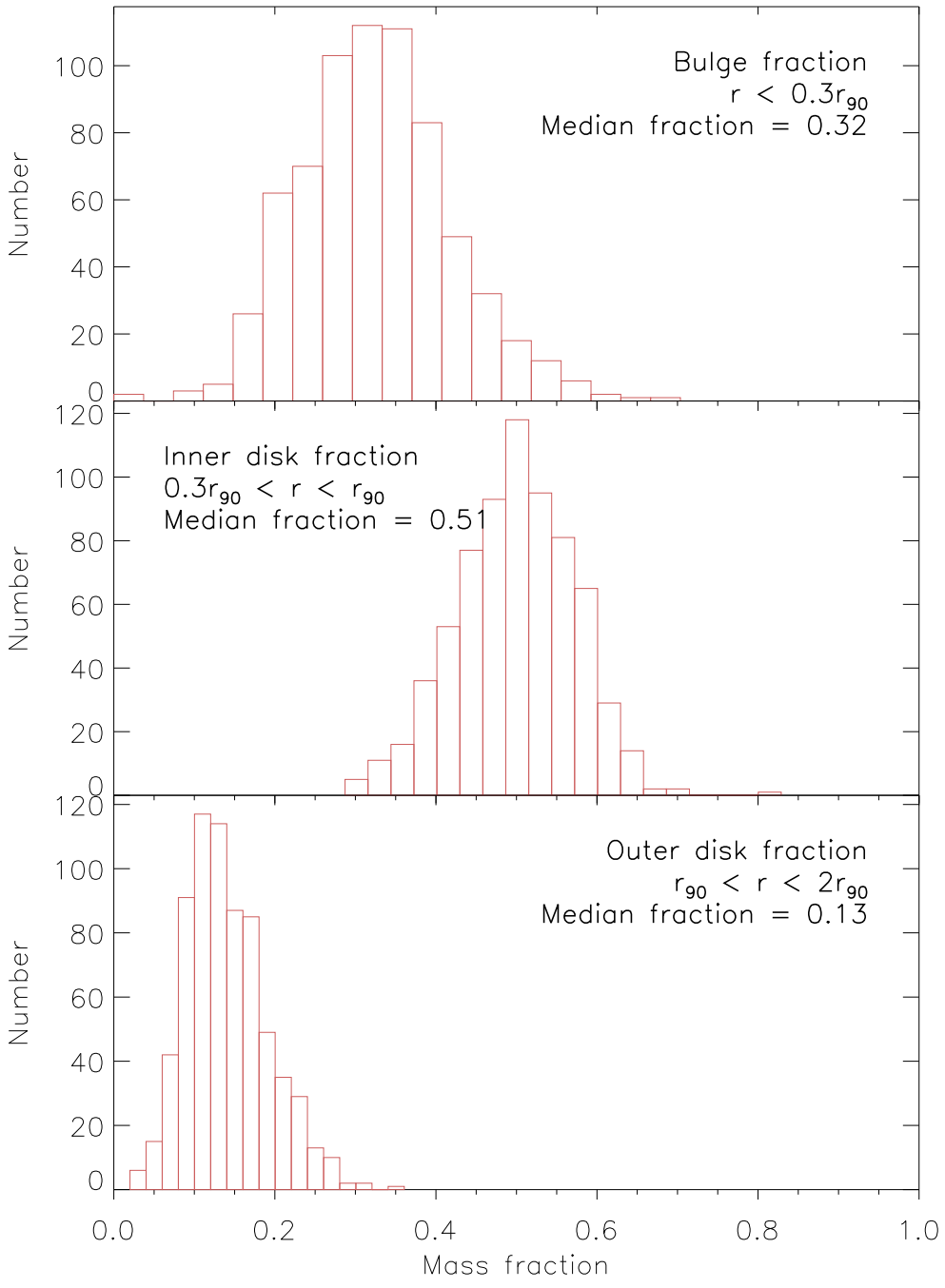

Figure 3.29: Observed stellar mass fraction of different parts of the disk.

resentative of the full population of disk galaxis, and was analyzed using more robust and sophisticated comparison to stellar population synthesis models.

In summary:

- We made ultra-deep stack images in 5 PS1 bands using all 700 galaxies to explore the properties of the faint stellar halo. We also made stack images using galaxies in three mass bins: low mass ($M_* < 10^{10}\,M_\odot$), medium mass ($10^{10}\,M_\odot < M_* < 10^{10.5}\,M_\odot$) and high mass ($M_* > 10^{10.5}\,M_\odot$). The isophotes outside $2\,r_{90}$ are significantly rounder than those inside, indicating that the stellar halo may contaminate the light from the outer disk in the region outside $2\,r_{90}$. We found that the radial profile of the stellar surface mass density shows a distinct up-turn from a single exponential at around $2\,r_{90}$, further supporting the contribution of the halo light beyond this radius.

- We used the combined data on the 700 individual galaxies to create normalized radial profiles in three bins of galaxy mass. The resulting characteristic radial SB profiles show downward bending breaks in the bluer bands (especially g-band), but become progressively smoother and more nearly single-exponentials as the bands move red-ward. The radial profiles of the stellar mass density are very close to single exponentials out to radii of twice r_{90}. This is true over the entire range in stellar mass sampled by our data. In all mass bins, the characteristic radial profiles of color, stellar mass-to-light ratio, and stellar age show a 'U'-shape (they first decline with increasing radius, but then rise in the

outer disk). The minima are located at radii of around 0.8 to 1.0 r_{90} or at locations where the local stellar mass surface density is $\sim 10 M_{\odot}/pc^2$.

- We also created normalized radial profiles in three bins in the concentration parameter ($C = r_{90}/r_{50}$), which is a good proxy for bulge/disk ratio (Hubble Type). We find that the amplitude of the break in the SB profile decreases as C increases (i.e. for earlier Hubble types). Moreover, the amplitude of the 'U'-shaped M/L radial profile also declines as C increases. In all cases, the radial stellar surface mass density remains a single exponential.

- We developed an automatic algorithm to find the break radii in the r-band SB radial profiles of each of the 700 individual galaxies. We then quantified the magnitude of the SB profile breaks using a slope ratio R_r, which is defined as the ratio of the slopes of the SB profiles in the inner (k_1) and outer (k_2) disk. We also measured an analogous ratio R_m based on the slopes of the inner and outer surface mass density radial profiles. We found that R_r has a log-normal distribution centered around log(R_r=-0.12) with a dispersion of 0.17, indicating that most r-band SB profiles are down-bending. On the other hand, R_m has a log-normal distribution, but is centered around log(R_r=0) with a dispersion of 0.16. This means most of the stellar surface mass density profiles are close to pure (single) exponentials. Both results are consistent with our findings based on the binned, normalized profile shapes.

- We explored the correlation between the r-band SB profile slope ratio R_r with the concentration parameter (C), total stellar mass (M_*), total SFR, specific SFR (sSFR), and average surface densities of stellar mass (Σ_{M_*}) and SFR ($\Sigma_{\rm SFR}$). There is a strong correlation between C and R_r, consistent with the results described above based on the composite profiles. No obvious correlations were found between the R_r and other parameters.

- We approximated the radial M/L profile in individual galaxies using a skewed 'V' shape function and characterized the results using the slopes of inner ($k_{\Upsilon_r 1}$) and outer ($k_{\Upsilon_r 2}$) disk r-band M/L profile. We found that $k_{\Upsilon_r 1}$ has a log-normal distribution centered on $\sim$-0.3, implying that most galaxies have M/L ratios that decrease with radius in the inner disk. In contrast, $k_{\Upsilon_r 2}$ has a log-normal distribution centered on $\sim$+0.2, implying that most galaxies have M/L ratios that increase with radius in the outer disk. We also examined $k_{\Upsilon_r 1}$ and $k_{\Upsilon_r 2}$ as functions of R_r as well as other physical parameters. We found that $k_{\Upsilon_r 2}$ strongly correlates with R_r while the $k_{\Upsilon_r 1}$ is almost a constant. The strongest other correlation is between $k_{\Upsilon_r 2}$ and C. This is consistent with PT06 and Bakos et al. (2008), as well as with our inferences based on the composite profiles.

- We conclude that down-bending SB profiles, pure exponential surface mass density profiles, and older outer disks (beyond r_{90}) are typical for the majority

of disk galaxies over a wide range in galaxy mass. However, these features weaken as the bulge/disk ratio increases. These results are consistent with recent numerical simulations of the evolution of disk galaxies. It appears that a combination of a radial migration of stars from the inner to the outer disk is required, but that a truncation of recent star-formation in the outer disk is also important. Together these two mechanisms may be able to create a smooth exponential radial mass profile while also creating an outer disk that is older than the inner disk.

Chapter 4

Summary and Future Prospects

4.1 Summary

As stated in Chapter 1, the focus of the thesis is on the structure and evolution of disk galaxies. The thesis contains two major projects: one is to construct a simple model for predicting the distribution of the ISM and star formation in galaxies based on the assumption that the two-fluid instability parameter ($Q_{2\mathrm{f}}$) of the galactic disk is a constant; the other is to investigate the distribution of stellar mass, star formation rate and mean stellar age in the outer disk and stellar halo using a multi-band SED fitting method.

4.1.1 'Constant Q' disk model

The 'Constant Q' (CQ) model was inspired by the pioneering work by Quirk (1972) and some SFL related work by (Leroy et al., 2008, hereafter L08) and Bigiel et al. (2008). The model predicts the gas surface mass density and star formation intensity given the rotation curve, stellar surface mass density and the gas velocity dispersion or vice versa. The model was tested on 12 galaxies from L08 and is successful in most parts of the galactic disk.

We explored four versions of two-fluid stability parameter Q_{2f} models and found that all four forms of $Q_{2\mathrm{f}}$ profiles are fairly flat over the intermediate radii of the disk, consistent with our basic assumption that the galactic disk is in a marginally stable state. We therefore adopted the Wang & Silk (1994) approximation of the two-fluid stability parameter, Q_{WS}, because of its simplicity.

Based on the assumption that the Q_{WS} is constant for the whole galactic disk, we can calculate the ISM distribution in a similar way to Quirk (1972). In order to compare more directly with the observations, we further tested different empirical relations of the molecular-to-neutral gas ratio R_{mol} so that we can calculate the distribution of both H_2 and HI. We tested three prescriptions of R_{mol} relations: the Stellar surface mass density - R_{mol} relation (SR relation, L08), the hydrostatic Pressure - R_{mol} relation (PR relation Elmegreen, 1989) and the more physically intuitive relation derived by Krumholz et al. (2008, 2009a,b) (KR relation) from self-shielding model of molecular clouds. All three prescriptions produce Σ_{HI} and $\Sigma_{\mathrm{H_2}}$ profiles that

match the observed profiles reasonably well. The SR relation produces the best fits to both the $\Sigma_{\rm HI}$ and $\Sigma_{\rm H_2}$ profiles and therefore is our favored model.

In order to calculate the distribution of the SFR using the derived $\Sigma_{\rm HI}$ and $\Sigma_{\rm H_2}$, we also tested eight versions of the SFLs. Five of the SFLs depend on just the total ISM (both neutral and molecular gas) content and the other three require the ISM to be separated into neutral and molecular phases. The linear molecular SFL ($\rm SFR_{H2}$) produces the best matches to the $\Sigma_{\rm SFR}$ profiles out of 8 versions of SFLs we have tested when used with the SR relation, with the models typically agreeing with the observed profiles to within a factor of 2.

The modeled star formation intensity profiles (Figs 2.6, 2.7, 2.8) match the observations best at intermediate radii, and show the largest deviations in the central region (where $R <= 0.3R_{25}$). It is not unexpected that the model fails in the very central part because of the significance of the central bulge might have very different kinematics. The large deviations in the outer disk requires further investigation.

The success of the CQ-Disk model implies that feedback acts to equilibrate the stability of the disk. This also means that the current angular momentum distribution in disks is not just due to the angular momentum distribution of the material that fell in but also depends on internal processes.

4.1.2 Structures of outer disk and stellar halo

In the second part of the thesis (Chapter 3), we conducted an investigation of the structure and stellar content of a sample of disk galaxies using the deep stacked Pan-STARRS1 (PS1) multi-band imaging observations. We selected 700 disk dominated and relatively face-on galaxies from the SDSS galaxy catalog. The stellar mass range of the sample extends from $\sim 10^9$ to 10^{11} $M_\odot$. Compared to previous related studies our sample is much larger, is more representative, and was analyzed using a more robust and sophisticated approach.

We derived 5-band surface brightness (SB) profiles for all 700 galaxies reaching SB levels of $28 - 30\,\mathrm{ABmag/arcsec^2}$ at the outer edge of the stellar disk at about $2\,r_{90}$ (the radius containing 90% of the r-band Petrosian flux). The characteristic radial surface brightness profiles show downward bending breaks in the bluer bands (especially g-band) with break radii around r_{90}, but become progressively smoother and more nearly single-exponentials as the bands move red-ward.

We then performed SED fitting to the 5-band photometry using the Multi-wavelength Analysis of Galaxy Physical Properties (MAGPHYS da Cunha et al. , 2008; Bruzual & Charlot , 2003; Charlot & Fall , 2000) software. The output has various physical parameters of which the most important are stellar mass, stellar mass-to-light ratio, specific star formation rate and luminosity-weighted mean stellar age. We compile and present the physical parameters in the form of radial profiles.

In all the bins of galaxy stellar mass, the radial profiles of the stellar surface mass

density are very close to single exponentials out to radii of twice r_{90}. The characteristic radial profiles of color, stellar mass-to-light ratio, and r-band luminosity-weighted mean stellar age show a 'U'-shape (they first decline with increasing radius, but then rise in the outer disk. The stellar surface mass density profiles are also smoother than the SB profiles.

The radial SB profiles in all 5 bands have the same break radius for a single galaxy. The break radii have a good correlation with r_{90} and the location of the minima of the 'U' shape M/L and color profiles. The minima of the M/L and color profiles shift slightly from 0.8 r_{90} for low-mass galaxies to r_{90} for high-mass galaxies. However, the location of the minima almost always correspond to a stellar mass surface density of $\sim 10 M_{\odot}/pc^2$.

We calculated the slopes of both inner and outer disk (divided by the break radius) r-band SB profiles and the inner-outer disk slope ratio R_r has a log-normal distribution centered around the value $\log(R_r)$=-0.12 (implying most galaxies have down-bending profiles). We also calculated the inner-outer disk slope ratio of stellar mass surface density profiles, R_m. It also has a log-normal distribution centered around $\log(R_m) = 0$ (consistent with a single exponential). The R_r also strongly correlates with the concentration parameter and the slope of the outer disk M/L profile. We propose that these distributions of R_r and R_m are more useful in characterizing the properties of the outer disk than the three discrete types of radial profiles proposed by PT06.

These results are consistent with recent numerical simulations of the evolution of disk galaxies. It appears that a combination of a radial migration of stars from the inner to the outer disk is required, but that a truncation of recent star-formation in the outer disk is also important. Together these two mechanisms may be able to create a smooth exponential radial mass profile while also creating an outer disk that is older than the inner disk. The effect of stellar radial migration is equally important for disk galaxies with stellar mass between $10^8 - 10^{12}\,\mathrm{M}\odot$ in the context of this thesis.

In order to study where the the stellar halo starts to dominate the outer disk in the SB profile, we stacked the images of all 700 galaxies to make 5-band images of a generic disk galaxy. The isophotes of the stacked images reach down to 30-32 ABmag/arcsec^2 depending on the wavelength. The isophotes in the region outside $2\,r_{90}$ become significantly rounder than those inside $2\,r_{90}$. The stellar surface mass density profile is pure exponential inside $2\,r_{90}$ but starts to bend upward after that. These two lines of evidence imply that the stellar halo starts to dominate the light beyond $2\,r_{90}$. The profiles of the stacked galaxy images show that the stellar halo has a comparable or even redder color (higher M/L; older age) than the inner bulge. The total mass of the stellar halo is about 1% that of the whole galaxy.

4.2 Future prospects

From the results of the thesis we learnt that the inside-out galaxy formation scenario is generally still valid but that internal secular evolution and the redistribution of stars and gas within the galactic disk is crucial to explain the current structure of the galactic disk. There are still many questions about the galaxy formation and evolution, and we conclude the thesis by describing how to improve our knowledge with some future projects:

We used a constant gas velocity dispersion and an indirect measurement of stellar velocity dispersion in Chapter 2. These imposed extra uncertainties on the CQ-disk model. A better choice is to use the CALIFA or the SDSS MaNGA IFU data to measure the stellar and gas dynamics more precisely for a large sample of galaxies. The CALIFA and MaNGA data will also be helpful for us to measure the radial distribution of the star formation rate, which can be used to calibrate our CQ-disk model.

We used photometry of the 5 optical bands to do SED fitting in Chapter 3. Although the stellar contents can be well constrained using these optical bands, the derived star formation and mean stellar age are not as reliable as the stellar mass. This is because of the degeneracy in the model fits between age and dust reddening. A better approach would be to use the GALEX FUV and NUV data as well as UKIDSS or WISE infrared data plus suitably smoothed version of the PS1 image to perform the SED fitting. The multi-band data from UV to infrared will provide a

much better constraint on the star formation and mean stellar age by breaking the age/dust degeneracy.

Our results about the outer stellar disk favor an interplay between stellar radial migration and a star formation threshold. The importance of stellar radial migration has been more and more recognized, but is still lacking direct evidence. A more direct approach would be to measure the chemical abundances of the stars in the Milky Way disk, which can be done with the SDSS APOGEE data.

We focused on the stellar contents in the second half of the thesis but almost ignored the gas content. The gas disk is usually more extended than the optical disk and this gas is the fuel for the star formation. Extended star formation has already been observed in some XUV disk galaxies (Thilker et al. , 2007). It is therefore also interesting to study the HI distribution of a subsample of the 700 galaxies. The relationship between the HI, star formation as traced in the UV and the stellar disk should shed more light on the formation and evolution of disk galaxies.

Chapter 5

Appendix

5.1 Galaxy list

5.2 Figures of each galaxy

Bibliography

Asplund, M., et al. 2009, ARA&A, 47, 481

Atkinson, A. M., Abraham, R. G., & Ferguson, A. M. N. 2013, ApJ, 765, 28

Bakos, J., Trujillo, I., & Pohlen, M. 2008, ApJ, L103

Bakos, J., & Trujillo, I. 2012, arXiv:1204.3082

Battaner, E., & Florido, E. 2000, FCPh, 21, 1

Bekki, K., & Couch, W.J. 2011, MNRAS, 415, 1783

Bell, E., & de Jong, R. 2001, ApJ, 550, 212

Bell, E. F. 2002, ApJ, 581, 1013

Bell, E. F., et al. 2003, ApJS, 149, 289

Binney, J., & Tremaine, S., Galactic Dynamics, Princeton Univ. Press, 2008

Bigiel, F., et al. 2008, AJ, 136, 2846

BIBLIOGRAPHY

Bigiel, F., et al. 2010a, ApJ, 720, L31

Bigiel, F., et al. 2010b, AJ, 140, 1194

Bigiel, F., & Blitz, L. 2012, ApJ, 756, 183

Blitz, L., & Rosolowsky, E. 2006, ApJ, 612, L29

Blitz, L., & Rosolowsky, E. 2006, ApJ, 650, 933

Boissier, S., Prantzos, N., Boselli, A., & Gavazzi, G. 2003, MNRAS, 346, 1215

Bosma, A. 1981, AJ, 86, 1825

Bird, J. C. et al. 2013, ApJ, 773, 43

Brinchmann, J., et al. 2004, MNRAS, 351, 1151

Bruzual, G. & Charlot, S. 2003, MNRAS, 344, 1000

Burton, W. B., Elmegreen, B. G., & Genzel, R., The Galactic Interstellar Medium, Springer-Verlag Berlin Heidelberg, 1992

Calzetti, D., et al. 2007, ApJ, 666, 870

Cardelli, J., Clayton, G., & Mathis, J. 1989, ApJ. 345, 245

Charlot, S. & Fall, S. M. 2000, ApJ, 539, 718

Chilingarian, I., Melchior, A.-L., Zolotukhin, I. 2010, MNRAS, 405, 1409

BIBLIOGRAPHY

Chilingarian, I., Zolotukhin, I. 2012, MNRAS, 419, 1727

Courteau, S. 1997, AJ, 114, 2402

da Cunha, E., et al. 2008, MNRAS, 388, 1595

Davé, R., Finlator, K., & Oppenheimer, B. D. 2011, MNRAS, 416, 1354

de Blok, W. J. G., et al. 2008, AJ, 136, 2648

de Jong, R. S., et al. 2007, ApJ, 667, L49

de Jong, R. S. 2008, MNRAS, 388, 1521

Debattista, V. P., et al. 2006, ApJ, 645, 209

Delgado, R. M. G., et al. 2014, A&A, 562, A47

Dopita, M. A. & Ryder, S. D. 1994, ApJ, 430, 163

D'Souza, R., Kauffmann, G., Wang, J., & Vegetti, S. 2014, arXiv:1404.2123

Duffy, A.R., Moss, A., Staveley-Smith, L. 2012a, PASA, 29, 202

Duffy, A. R. 2012b, MNRAS, 420, 2799

Dutton, A., 2009, MNRAS, 396, 121

Dutton, A. & van den Bosch, F. C., 2009, MNRAS, 396, 141

Dutton, A. & van den Bosch, F. C., 2011, arXiv:1108.0663

BIBLIOGRAPHY

Elmegreen, B. G. 1989, ApJ, 338, 178

Elmegreen, B. G. 1993, ApJ, 411, 170

Elmegreen, B. G. 1997, RMxAC, 6, 165

Elmegreen, B.G., & Parravano, A. 1994, ApJ, 435, L121

Elmegreen, B. G. & Hunter, D. A. 2006, ApJ, 636, 712

Elmegreen, B. G. 2011, ApJ, 737, 10

Erwin, P., Beckman, J., Pohlen, M. 2005, ApJ, 626, L81

Erwin, P., Pohlen, M., Beckman, J. 2008, AJ, 135, 20

Fall, S. M., & Efstathiou, G. 1980, MNRAS, 193, 189

Ferguson, A. M. N., & Clarke, C. J. 2001, MNRAS, 325, 781

Ferguson, A. M. N. 1998, PHD Thesis

Freeman, K. C. 1970, ApJ, 160, 811

Fu, J., et al. 2013, MNRAS 434, 1531

Genel, S., et al. 2012, ApJ, 745, 11

Glover, S. C. O. & Clark, P. C. 2012, MNRAS, 421, 9

Gogarten, S. M., et al. 2010, ApJ, 712, 858

BIBLIOGRAPHY

Goldreich, P., & Lynden-Bell, D. 1965, MNRAS, 130, 125

Gunawardhana, M.L.P., Hopkins, A.M., Sharp, R.G., et al. 2011, MNRAS, 415, 1647

Guo, Q., et al. 2011, MNRAS, 413, 101

Heckman, T. M., Armus, L., & Miley, G. K. 1990, ApJS, 74, 833

Herrmann, K., Hunter, D. & Elmegreen, B. 2013, AJ, 146, 104

Hessman, F. V., & Ziebart, M. 2011 A&A, 532, A121

Hoekstra, H., van Albada, T. S., & Sancisi, R. 2001, MNRAS, 323, 453

Hunter, D., Elmegreen, G. G., & Baker, A. L. 1998, ApJ, 493, 595

Hunter, D.A., Elmegreen, B.G., & Ludka, B.C. 2010, AJ, 139, 447

James, P.A., Shane, N.C., Beckman, J.E., et al. 2004, A&A, 414, 23

Johansson, P.H., Naab, T., Burkert, A. 2009, ApJ, 690, 802

Jog, C. J., & Solomon, P. M. 1984, ApJ, 276, 114

Jog, C. J. 1996, MNRAS, 278, 209

Kaiser, N., et al. 2002, SPIE, 4836, 154

Kauffmann, G., et al. 2003, MNRAS, 341, 33

Kauffmann, G., et al. 2003, MNRAS, 341, 54

BIBLIOGRAPHY

Kennicutt, R.C. 1989, ApJ, 344, 685

Kennicutt, R.C. 1998, ApJ, 498, 541

Kennicutt, R.C., Jr., Bresolin, F., & Garnett, D.R. 2003, ApJ, 591, 801

Kennicutt, R.C., et al. 2007, ApJ, 671, 333

Kennicutt, R.C., Jr., Lee, J.C, Funes, S.J., et al. 2008, ApJS, 178, 247

Kepner, J. V. 1999, ApJ, 520, 59

Kobulnicky, H. A., & Kewley, L. J. 2004, ApJ, 617, 240

Krumholz, M. R., & McKee, C. F. 2005, ApJ, 630, 250

Krumholz, M. R., & Thompson, T. A. 2007, ApJ, 669, 289

Krumholz, M. R., McKee C. F., & Tumlinson, J. 2008, ApJ, 689, 865

Krumholz, M. R., McKee C. F., & Tumlinson, J. 2009, ApJ, 693, 216

Krumholz, M. R., McKee, C. F., & Tumlinson, J. 2009, ApJ, 699, 850

Krumholz, M. R., & Gnedin, N. Y. 2011, ApJ, 729, 36

Kregel, M., van der Kruit, P. C., & de Grijs, R. 2002, MNRAS, 334, 646

Lee, J.C., Gil de Paz, A., Tremonti, C., et al. 2009, ApJ, 706, 599

Leroy, A. K. et al. 2008, AJ, 136, 2782

BIBLIOGRAPHY

Li, Z., et al. 2011, ApJS, 197, 22

Lin, D. N. C., & Pringle, J. E. 1987, ApJ, 320, L87

Lin, D. N. C., & Pringle, J. E. 1987, MNRAS, 225, 607

Lotz, J.M., Jonsson, P., Cox, T.J., & Primack, J. 2008, MNRAS, 391, 1137

MacArthur, L., et al. 2004, ApJ, 152, 175

Majewski, S. R. 1993, ARA&A, 31, 575

Markwardt, C. B. 2009, Astronomical Data Analysis Software and Systems XVIII ASP Conference Series, 411, 251

Martín-Navarro, I. et al. 2012, MNRAS, 427, 1102

Martín-Navarro, I. et al. 2014, arXiv:1401.3749

Masters, K. L., et al. 2010, MNRAS, 404, 792

Matínez-Serrano, F. J., et al. 2009, ApJ, 705, L133

Meurer, G. R., et al. 2006, ApJS, 165, 307

Meurer, G. R., et al. 2009, ApJ, 695, 765

Meurer, G. R., Zheng, Z., & de Blok, E. 2013, MNRAS, 429, 2537

Martin, C. L., & Kennicutt, R. C. 2001, ApJ, 555, 301

BIBLIOGRAPHY

McKee, C.F., & Ostriker, E.C., 2007, ARA&A, 45, 565

Nelson, E. J., et al. 2012, ApJ, 747, L28

Minchev, I., et al. 2012, A&A, 548, A126

Mo, H., Mao, S., & White, S. 1998, MNRAS, 295, 319

Moustakas, J., et al. 2010, ApJS, 190, 233

Muñoz-Mateos, J. C., et al. 2009, ApJ, 701, 1965

O'Brien, J. C., Freeman, K. C., & van der Kruit, P. C. 2010, A&A, 515, A62

Ostriker, E. C., McKee, C. F., & Leroy, A. K. 2010, ApJ, 721, 975

Persic, M., Salucci, P. & Stel, F. 1996, MNRAS, 281, 27

Pohlen, M., et al. 2002, A&A, 392, 807

Pohlen, M. & Trujillo, I. 2006, A&A, 759, 772

Pěrez, E. et al., 2013, ApJ, 764, L1

Quirk, W. J. 1972, ApJ, 176, L9

Radburn-Smith, D. J., et al. 2012, AJ, 753, 138

Rafikov, R. R. 2001, MNRAS, 323, 445

Rest, A., et al. 2013, arXiv:1310.3828

Romeo, A. B. & Wiegert, J. 2011, MNRAS, 416, 1191

Roškar, R., et al. 2008, ApJ, 675, L65

Saintonge, A., et al. 2011, arxiv:1104.0019

Sánchez-Blázquez, P., et al. 2009, MNRAS, 398, 591

Schaye, J. 2004, ApJ, 609, 667

Schiminovich, D., et al. 2007, ApJS, 173, 315

Schlafly, E. F., et al. 2012, ApJ 756, 158

Schlegel, D., Finkbeiner, D., & Davis, M. 1998, ApJ, 500, 525

Schmidt, M. 1959, ApJ, 129, 243

Sellwood, J. A. & Binney, J. J. 2002, MNRAS, 336, 785

Sellwood, J. A. 2013, arXiv: 1310.0403

Silk, J. 1997, ApJ, 481, 703

Sofue, Y., & Rubin, V. 2001, ARA&A, 39, 137

Strauss, M. A., et al. 2002, AJ, 124, 1810

Szalay, A. S., et al. 1999, AJ, 117, 68

Tamburro, D. et al. 2009, AJ, 137, 4424

Tan, J. C. 2000, ApJ, 536, 173

Tan, J. 2010, ApJ, 710, L88

Thilker D. A., Bianchi L., Boissier S., et al., 2005, ApJ, 619, L79

Thilker, D. A., et al. 2007, ApJS, 173, 538

Thilker, D. A., et al. 2014, in preparation

Tonry, J. L., et al. 2012, ApJ, 750, 99

Toomre, A. 1964, ApJ, 139, 1217

Tremonti, C. A., et al. 2004, ApJ, 613, 898

van den Bosch, F. C. 2001, MNRAS, 327, 1334

van der Hulst, J. M. et al. 1993, AJ, 106, 548

van der Kruit, P.C. 1979, A&AS, 38, 15

van der Kruit, P. C. & Searle, L. 1981, ApJ, 95, 105

van der Kruit, P.C. 1987, A&AS, 173, 59

van der Kruit, P. C. 1988, A&A, 192, 117

Walter, F., et al. 2008, AJ, 136, 2563

Wang, B. & Silk, J. 1994, ApJ, 427, 759

BIBLIOGRAPHY

White, S. D. M., & Rees, M. J. 1978, MNRAS, 183, 341

Wang, J., et al. 2011, MNRAS, 412, 1081

Wong, I., et al. 2013, in preparation

Wong, T., & Blitz, L. 2002, ApJ, 569, 157

Wong, T. 2009, ApJ, 705, 650

Yoachim, P., Roškar, & Debattista, V. 2010, ApJ 716, L4

Yoachim, P., Roškar, & Debattista, V. 2012, ApJ 752, 97

Younger, J. D., et al. 2007, ApJ, 670, 269

Zaritsky, D., Kennicutt, R.C., Jr., & Huchra, J P. 1994, ApJ, 420, 87

Zheng, Z., et al. 1999, AJ, 117, 2757

Zheng, Z., et al. 2014, submitted to ApJ

Zibetti, S., White, S., and Brinkmann, J. 2004, MNRAS 347, 556

Zibetti, S., & Ferguson, A. 2004, MNRAS 352, L6

Vita

Zheng Zheng received the Sc. B. degree in Physics from Shandong University in 2004 and Sc. M. degree in Astrophysics from the National Astronomical Observatories, Chinese Academy of Sciences in 2007. He then enrolled in the Astronomy Ph.D. program at Johns Hopkins University in 2007. His research focuses on disk galaxies.